Fully Quantum Measurement of the Electron Magnetic Moment

A thesis presented
by

Brian Carl Odom

to
The Department of Physics
in partial fulfillment of the requirements
for the degree of
Doctor of Philosophy
in the subject of

Physics

Harvard University
Cambridge, Massachusetts
October 2004

Thesis advisor Author

Gerald Gabrielse **Brian Carl Odom**

Fully Quantum Measurement of the Electron Magnetic Moment

Abstract

This thesis reports a preliminary result for the first fully quantum measurement of the electron magnetic moment. This 0.6 parts per trillion result is the most accurate to date and is combined with existing Quantum Electrodynamics theory to yield a new value for the fine structure constant. The measurement uses quantum spectroscopy of transitions between the ground and first-excited cyclotron and spin states of a single electron, eliminating errors associated with relativistic mass corrections of excited states. A dilution refrigerator provides the 0.1 K temperature needed to cool the cyclotron motion, ensuring that only the ground state is occupied, and to cool the axial motion, reducing thermal broadening of the cyclotron and spin-flip resonances. The measurement is performed in a cylindrical trap cavity with well characterized electromagnetic standing-wave modes, making possible the first cavity-shift correction to the measured magnetic moment.

Contents

List of Figures

List of Tables

Acknowledgments

It has been my pleasure to work with Jerry Gabrielse for more than a few years on this rewarding project. Under his guidance and vision, a measurement which has been many graduate students' theses in the making is coming together in a wonderful way. And under his tutelage, reliable availability, and constant support, I learned to do science.

I am privileged to present results of a measurement which has been under development for almost two decades, benefitting from the dedication of many students. However, most obvious to me are the contributions of the students with whom I have worked. Steve Peil laid an excellent foundation by developing a sub-Kelvin trap for single electrons, and his demonstration of single quantum jumps with Geronimo form the basis of the current experiment. Brian D'Urso made a plethora of clever improvements to the detection system, such as the self-excited oscillator and 200 MHz amplifier, which have developed into crucial parts of the experiment and contribute significantly to the quality of data we are now collecting. I particularly appreciate Brian's friendship and collaboration during the few years when it seemed that the experiment could do nothing but fail in new and creative ways. Ramon van Handel's adjustable-height spacer provided an important improvement B-field stability. Finally, Dave Hanneke has played a central role in the final stages of this first-generation result. Dave's temperature regulation system is essential, and he has taken much of the data presented in this thesis. His willingness to run the experiment while I hypothetically wrote my thesis often translated into his filling cryogens and fixing equipment while I analyzed results and contemplated physics. For his generosity under that division of labor I am very grateful.

If I listed all the graduate students and postdocs whose companionship I have thoroughly enjoyed, it would be akin to someone who generally lies about their age sharing his taste in music. But, for any of you who might read this thesis, it has been a delight.

I have enjoyed many helpful conversations with my committee members Ike Silvera and Bob Wesetervelt, whose genuine concern for my wellbeing was very encouraging and who helped me through problems ranging from superleaks to overly hot electrons. The excellent work and rush jobs of Louis DeFeo, Rich Anderson, and Al Chandler in the machine shop deserve substantial recognition. Without their often having slipped my projects forward in the queue, the data which have come together literally over the last two weeks would have been delayed, and this thesis would have been significantly less exciting to present. Also, kindnesses of Jan Ragusa, Vickie Greene, Stan Coutreau and others in the Harvard Physics Department have been significant.

My father's contributions to my personal and scientific development are substantial – science fair projects and his off-hand statement that I might particularly enjoy learning physics when I got to 11th grade – come to mind. My mother's dedication to provide only the best in nurture and education have had an impact which I will probably continue to discover for the rest of my life. And my wife Teri was a living reminder that I too could live – and even live well – if the magnet did indeed quench again.

Finally, I thank God, through whose active participation in my life I have been rescued from what I might have become, with failures and successes becoming both bigger and smaller, and much more meaningful.

Chapter 1

Introduction

This thesis reports a preliminary result for the first fully quantum measurement of the electron magnetic moment. We measure cyclotron and spin-flip transition frequencies exclusively between the ground and first-excited cyclotron and spin states of a single electron–a quantum cyclotron [1]. The preliminary error assignment of 0.6 part per trillion (ppt) achieved in this work represents a factor of 7 improvement over the best previous measurements [2, 3]. When combined with existing theory [4, 5, 6], this measurement of the electron magnetic moment provides the most accurate determination of the fine structure constant, α. Quantum Electrodynamics (QED), generally considered to already be the most stringently tested physical theory [7], can be further tested by comparing this determination of α with values obtained by different types of experiments, if ever a measurement by another method approaches the accuracy we attain. The work reported here also opens the way for improved tests of CPT (Charge, Parity, Time Reversal) symmetry and Lorentz Invariance for leptons.

Improvements of this measurement over previous experiments are discussed in Sec. 1.2. The quantum cyclotron is realized with a single electron in a sub-Kelvin cylindrical Penning trap. The details of the apparatus and dynamics of the trapped electron are discussed in Chapter 2. Precise measurement of the magnetic moment of the electron requires a highly stable magnetic field, discussed in Chapter 3. This stability allows accurate measurement of the cyclotron and anomaly resonance frequencies, as discussed in Chapter 4. Effects of the microwave cavity, formed by the conducting walls of the Penning trap, are discussed in Chapter 5. Finally, analysis of the results and of systematic uncertainties is presented in Ch. 6.

1.1 The g Value and Fundamental Physics

The g value of a particle is proportional to the ratio of its magnetic moment $\vec{\mu}$ to its angular momentum $\vec{S}$:

$$\vec{\mu} = g\,\frac{q\hbar}{2m}\,\frac{\vec{S}}{\hbar}\,, \tag{1.1}$$

where $\hbar$ is Planck's constant, q is the charge, m is the mass, and the quantity $|\,q|\,\hbar/2m$ is recognized as the Bohr magneton for the case of the electron.

For a non-relativistic rotating charged body with equal charge and mass distributions, classical electricity and magnetism predicts $g = 1$. The Dirac equation, if used as a single-particle wave equation, predicts $g = 2$. And, Quantum Electrodynamics predicts that g differs from 2 by about 1 parts in 10^3. Because modern experiments take advantage of the smallness of this offset and actually measure the quantity g - 2, as discussed in Sec. 1.2.1, they are often called "g - 2" experiments. Often, results of

g value experiments are presented in terms of the "electron anomaly" a_e, defined by

$$\frac{g}{2} = 1 + a_e. \tag{1.2}$$

1.1.1 Theoretical Prediction for the g Value

Quantum electrodynamics predicts that the magnetic moment of the electron is given by a series expansion in the fine structure constant α. The full standard model prediction for g also includes small, but now observable, non-QED contributions. The expansion for the g value is given by

$$\frac{g}{2} = 1 + C_1\left(\frac{\alpha}{\pi}\right) + C_2\left(\frac{\alpha}{\pi}\right)^2 + C_3\left(\frac{\alpha}{\pi}\right)^3 + C_4\left(\frac{\alpha}{\pi}\right)^4 + \ldots + a_{\mu,\tau} + a_{had} + a_{weak}\,, \tag{1.3}$$

where the coefficients C_1, C_2, C_3, ... and the muon and tau contribution $a_{\mu,\tau}$ are predicted by QED theory, and a_{had} and a_{weak} are the non-QED hadronic vacuum polarization and weak contributions. C_1 was first shown by Schwinger [9] to be exactly 0.5. C_2 requires the evaluation of 7 Feynman diagrams and is known analytically to be $-0.328\ldots$ [10, 11]. The 72 Feynman diagrams for C_3 are now known analytically to yield $1.181\ldots$ [6]. The C_4 calculation, involving 891 four-loop Feynman diagrams, has been calculated numerically [4, 12] to be ~ -1.71, which includes a recent correction [5] that resulted in a shift of the predicted g value by - 6 ppt. Work on the 10th-order Feynman diagrams for C_5 has begun, but currently only 784 of the 12,672 diagrams have been evaluated [12]. A rough estimate [13] of the contributions of the C_5 term yields an uncertainty (shown in Fig. 1.1) which is currently larger than the uncertainty

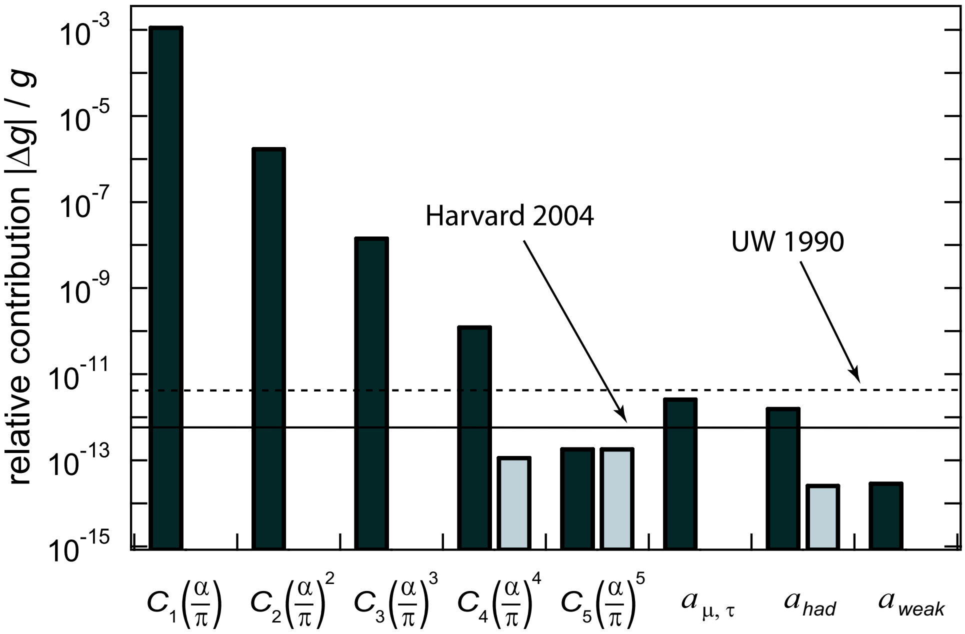

Figure 1.1: Relative contribution of the terms from Eq. (1.1) to the electron g value (dark bars) and magnitude of their uncertainties (light bars). The solid line represents the accuracy of the 2004 Harvard g value measurement presented in this thesis. The dashed line represents the accuracy of the 1990 University of Washington measurement [8].

in the C_4 contribution. The non-electron terms are [14]

$$a_{\mu,\tau} = 2.721 \times 10^{-12} \tag{1.4}$$

$$a_{had} = 1.642(27) \times 10^{-12} \tag{1.5}$$

$$a_{weak} = 0.030 \times 10^{-12}. \tag{1.6}$$

Relative contributions of all terms to the g value along with their uncertainties are displayed in Fig. 1.1. As can be seen from the figure, the g value measurement presented in this thesis for the first time probes the contributions of muonic and hadronic vacuum polarization.

1.1.2 The Fine Structure Constant

The fine structure constant α is the coupling constant which quantifies the interaction of the radiation field with electric charge. In SI units,

$$\alpha = \frac{e^2/\hbar c}{4\pi\epsilon_0}, \tag{1.7}$$

where $\hbar = h/2\pi$ is Planck's constant, c is the speed of light, and ϵ_0 is the permittivity of free space.

The quantitative prediction of Quantum Electrodynamics for the electron magnetic moment is the most stringently tested prediction of any physical theory [7]. The tremendous success of QED is also of practical importance for its role in the determination of fundamental constants common to many measurements [15]. For example, the most accurate resistance calibration standards, based on the integer quantum Hall effect, produce the standard resistance $R_K = h/e^2 = \mu_0 c/2\alpha$. Since μ_0 and c are defined quantities, the only uncertainty in the value of R_K is in the accuracy of α, which is best known from electron magnetic moment experiments. Thus the thoroughly non-quantum, non-relativistic concept of resistance is calibrated based on calculation of high-order Feynman diagrams and the electron g value measurement. Similarly, if a proposed redefinition of the kilogram is adopted, $\hbar$ would become an exact constant, and current knowledge of α would be the limiting factor in calibration of ac Josephson effect voltage standards [16].

The electron magnetic moment measurement presented in this work can be combined with the most recent QED calculations [6, 12, 13] to calculate a new value for the fine structure constant. We obtain the preliminary result

$$\alpha^{-1} = 137.035\,999\,777\ (27)\ (67), \tag{1.8}$$

where the first uncertainty is from theory and the second is from experiment. (See Sec. 5.4.2 for comments on the experimental uncertainty.)

1.1.3 Testing Quantum Electrodynamics

Although the interaction between light and electric charge is described by a running coupling constant, α is defined as the low-energy limit of this constant. Regardless of any possible breakdown of QED at high energies, all experiments which measure the fine structure constant must yield the same result [17]. Thus, comparisons between values of α obtained from various experiments, shown in Fig. 1.2, constitutes a test of QED.

The quantum Hall result [18] is the only experiment shown in Fig. 1.2, besides the electron g value, which yields α directly. Many of the results given in Fig. 1.2 rely on measurements of the Rydberg constant $R_\infty = \alpha^2 m_e c/2h$, which is often useful because it has been measured very accurately [13] and because it connects a fundamental mass to the fine structure constant. The h/m_{Cs} measurement based on cesium recoil experiments [19, 20], along with a measured cesium-to-proton mass ratio [21] and a measured proton-to-electron mass ratio [13], gives the second most accurate value for α. Ongoing analysis of systematic uncertainties in the completed h/m_{Cs} experiment, as well as improvements to the atom interferometer for a new measurement, have the goal of improving this result [22].

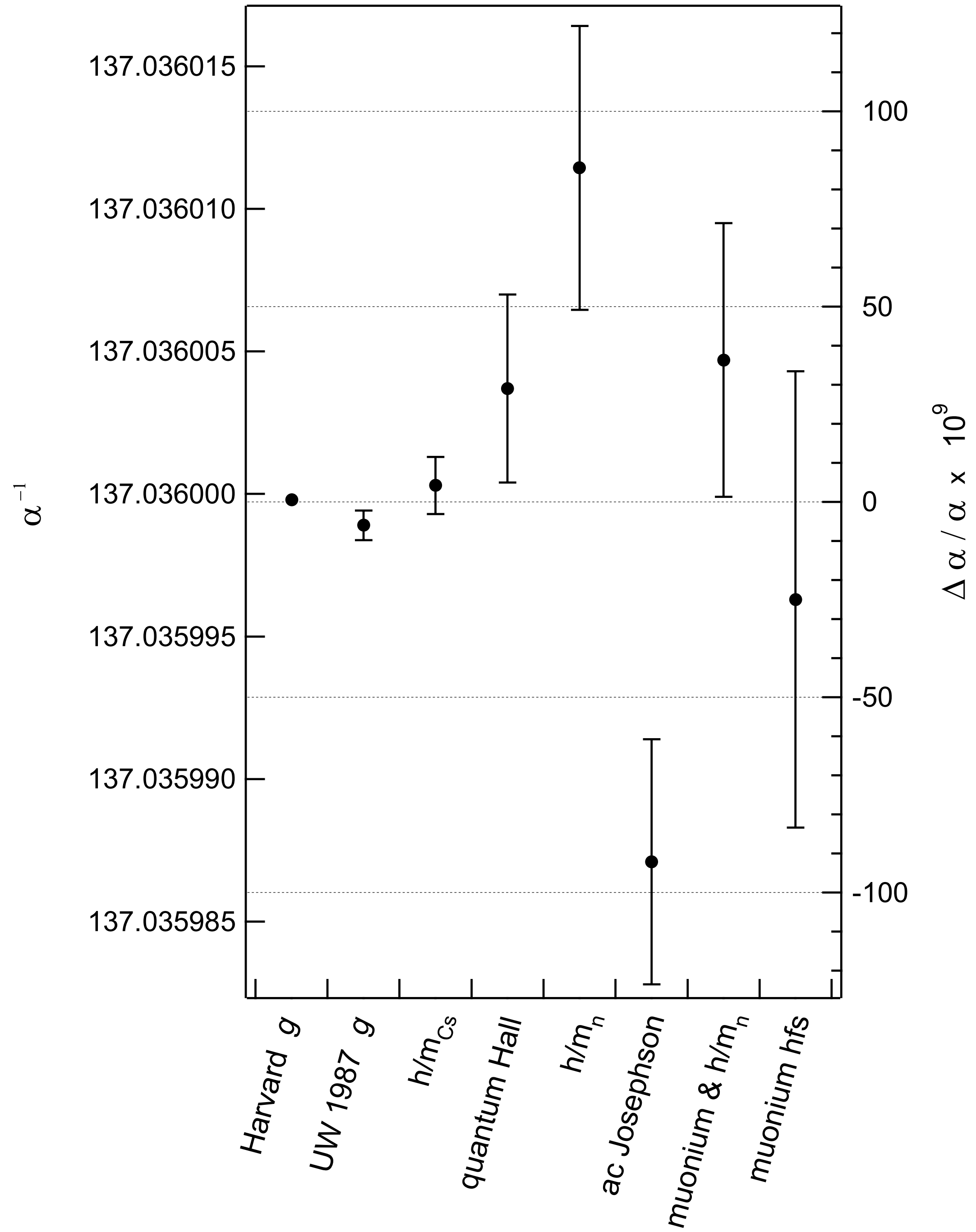

Figure 1.2: Comparison of the fine structure constant α as determined by several experiments. The 1998 CODATA value [13], corresponding to zero on the right-hand axis, is based primarily upon the 1987 University of Washington g value measurement [2] and a flawed QED calculation which was since discovered [5] to produce a +6 ppb error in the inferred value for α^{-1}. The uncertainty for the Harvard g value measurement is less than the width of the point.

Similarly to the cesium recoil result, the neutron h/m_n measurement [23] combined with measurements of the electron [24] and neutron [25] masses determines α. Measurement of the muonium hyperfine splitting and of the magnetic moment of the muon also yield a value for α [26]. If the h/m ratio from the neutron or cesium is used along with the muonium hyperfine splitting, the precision of the muonium results can be improved [27] at the cost of independence of the two results. The ac Josephson experiment measures e/h [13] and then is combined with measurements of the shielded helion gyromagnetic ratio [28, 29] and the shielded proton gyromagnetic ratio [30] to obtain α. Not shown in Fig. 1.2, because of the larger theoretical uncertainties [31, 32], are results from helium fine structure spectroscopy [33, 34]. The disagreement claimed by some of these measurements shown in Fig. 1.2, not generally regarded as pointing to a failure of QED, is larger than one might hope.

1.1.4 Testing CPT Symmetry and Lorentz Invariance

The CPT theorem states that any physical theory must be invariant under the combined operations of charge conjugation, parity inversion, and time reversal. The CPT theorem can be proven for local relativistic field theories of point particles in flat spacetime [35]. It is interesting to note that string theories, which describe extended objects, do not meet these criteria.

One testable consequence of the CPT theorem is that a particle and its antiparticle must have opposite charge, the same mass, the same lifetime, and opposite magnetic moment. Thus, comparison of the electron and positron magnetic moments and charge-to-mass ratios constitute a test of CPT. Also, searches for diurnal variations of resonance frequencies of an electron (without comparison to a positron) probe terms in a Standard Model extension [36, 37, 38] which violate Lorentz invariance, some of which also violate CPT.

Previous work with electrons and positrons in Penning traps [39, 40] sets stringent limits on CPT and Lorentz violation in the lepton sector. The figure of merit [41] for Lorentz and CPT violation achieved by these experiments is comparable to that achieved in experiments on neutral kaons [42], which is generally considered to set the most stringent bounds on CPT violation in any system. The techniques reported in this thesis for better measurements of the electron g value, in particular the narrowing of anomaly and cyclotron resonance widths discussed in Sec. 1.2.3, also opens the way for improved tests of CPT and Lorentz invariance.

1.1.5 Time Dependence of α

The possibility that physical constants might vary in time or space, originally proposed by Dirac [43], is now a common feature of models which attempt to use string theories to unify gravity and quantum mechanics [44]. Recent astrophysical observations [45, 46] report that the fine structure constant has changed for a redshift range $0.2 < z < 3.7$, on the level of $\Delta\alpha/\alpha = (-0.54 \pm 0.12)$. It is interesting, then, to consider what sensitivity to $\dot{\alpha}/\alpha$ might be achieved in laboratory experiments. Recent comparison of atomic clocks have established $\dot{\alpha}/\alpha < \pm\, 2.9 \times 10^{-15}/\ \mathrm{yr}^{-1}$ [47]. Thus, g value measurements such as the one presented in this thesis, while far better for measuring the value of α, are unlikely to be made competitive with clock experiments in searches for non-vanishing $\dot{\alpha}$.

1.1.6 The Muon g Value

Muon and electron g value measurements are complementary experiments which fill very different roles [14]. Assuming electron-muon universality, the same Feynman diagrams can be used to predict the muon and the electron anomalous magnetic moments. However, because of the mass difference, even the purely QED calculations yield different predictions for the electron and muon anomalies at the 0.5% level. More importantly, coupling of the lepton to some other massive particle scales like $(m_\mu/m_e)^2 \approx 4 \times 10^4$. Thus, the higher sensitivity to massive particles with accompanying challenges in QED calculations, along with three orders of magnitude poorer measurement accuracy, prevents the muon g value experiments from competing with the electron measurements as a test of QED.

On the other hand, the muon g value, with the current precision $\Delta g/g = 6 \times 10^{-10}$ [48], is already well into the regime of sensitivity to the weak interactions and serves as a sensitive probe for new massive particles. Toward this end, electron g value measurements can be seen as providing important verification of the dominant QED contributions to the muon g value. At present, muon g value measurements [48] disagree with the Standard Model theory by $2.7\,\sigma$ [49].

1.2 The Harvard g Value Measurement

Tremendous precision is available in frequency measurements of periodic phenomena. As a result, the highest precision experiments tend to be performed in systems where the measured quantity is a frequency. Electron g value experiments, representing the most precise tests of QED, also follow this pattern.

The experiment presented here combines the accuracy of a frequency measurement with the discrete nature of quantum mechanics for the first fully quantum g value measurement. In this work, cyclotron and spin-flip frequency measurements are made exclusively on transitions between the ground and first-excited cyclotron and spin states, shown in Fig. 1.4. This exquisite quantum control prevents subtle effects of special relativity (see Sec. 6.2.1) from contributing any uncertainty to the g value measurement.

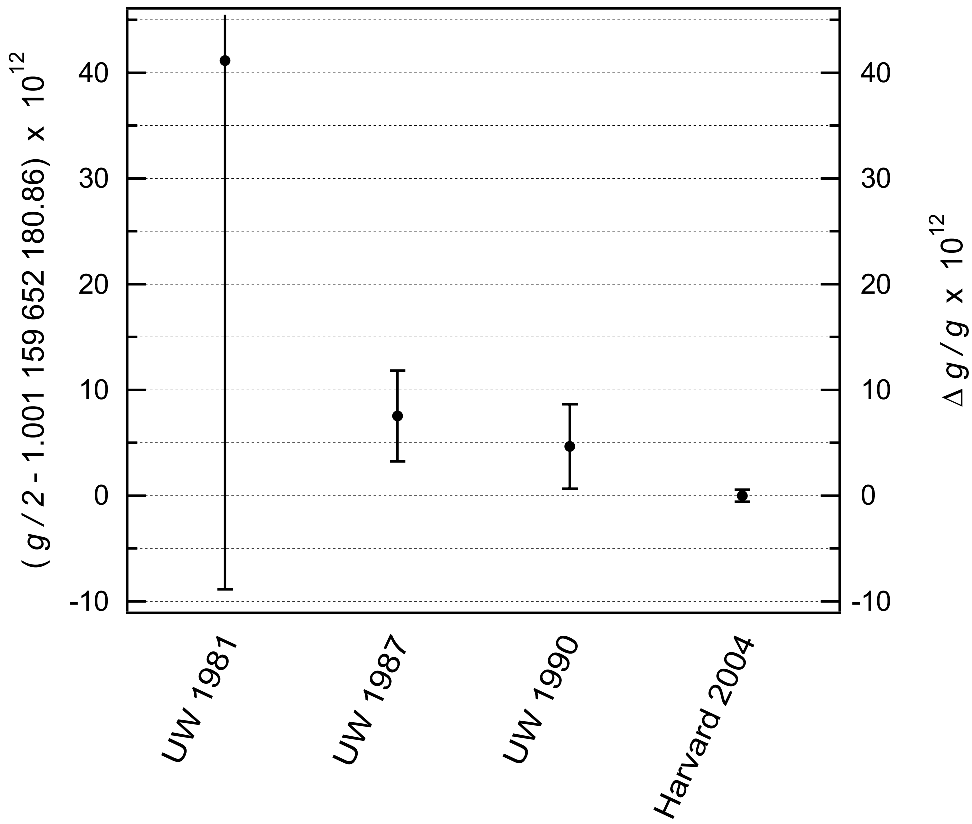

Figure 1.3: Comparison of recent g value measurements. The zero of vertical axes is set to the Harvard 2004 result presented in this thesis. "UW" denotes experiments [50, 2, 3] performed at the University of Washington.

In this thesis, we present a preliminary measurement of g with an accuracy of 0.6

ppt, which represents a factor of 7 improvement over previous measurements [2, 8], as shown in Fig. 1.3. Besides the fully-quantum spectroscopy already mentioned, other innovations which allow for the substantial improvement include cooling of the electron to below 1 Kelvin and the use of a cylindrical trap cavity with a well characterized radiation-field spectrum.

1.2.1 g Value Measurement Basics

The level diagram of Fig. 1.4 shows the quantized motions of a single electron in a Penning trap. Since $g \neq 2$, the cyclotron frequency ω_c and spin frequency ω_s are not quite equal, resulting in a non-zero anomaly interval $\hbar\omega_a$. The anomaly transition is a two-photon transition involving both a spin flip and a cyclotron jump.

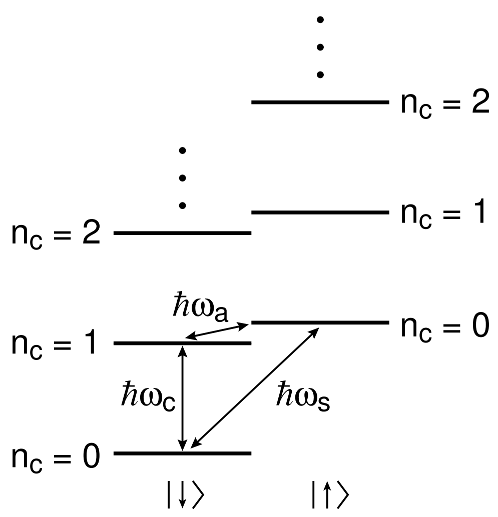

Figure 1.4: Diagram of spin and cyclotron quantum energies of an electron in a magnetic field. The effects of special relativity and of the electrostatic trapping potential are not included here.

As discussed in Ch. 6, g could be determined by measurement of cyclotron and spin frequencies: $g/2 = \omega_s/\omega_c \approx 1$. However, g - 2 can be obtained directly from the cyclotron and anomaly frequencies: $g/2 - 1 = \omega_a/\omega_c \approx 1 \times 10^{-3}$. Thus, given comparable precision in measurement of any of the frequencies, an experiment which measures g - 2 gains three orders of magnitude in precision over one that measures g directly.

1.2.2 Single Quantum Spectroscopy and Sub-Kelvin Cyclotron Temperature

Penning trap g value experiments typically operate at a magnetic field of about 5-6 Tesla, where the cyclotron level spacing corresponds to 7-8 Kelvin. A cyclotron oscillator in a Penning trap at liquid helium temperature (4.2 K) will spend about 20% of its time excited out of the ground state by blackbody radiation. Cooling the trap cavity to sub-Kelvin temperatures with a dilution refrigerator ensures that the cyclotron oscillator is essentially always in the ground state unless excited by an applied microwave drive [1].

As discussed in Sec. 6.2.1, the relativistic mass increase associated with a single cyclotron energy quantum creates a fractional cyclotron frequency shift $\Delta\omega_c/\omega_c \approx -1 \times 10^{-9}$, corresponding to $\Delta g/g \approx 1 \times 10^{-12}$. This is quite a large effect compared with the precision $\Delta g/g \approx 2 \times 10^{-13}$ presented in this thesis. When performing classical cyclotron spectroscopy at 4.2 K, as in previous g value experiments [8], errors caused by a combination of the relativistic anharmonicity and blackbody excitations can be as large as $\Delta g/g \approx 10^{-12}$ [51, 52].

Thus, it is advantageous to perform spectroscopy between the two lowest quantum states, where there is a precisely known relativistic frequency shift. Of course, performing single-quantum spectroscopy is not trivial. This feat requires excellent axial frequency resolution (see Sec. 2.3.7), a temperature lower than 4 Kelvin, and a trap cavity which provides a strongly enhanced cyclotron lifetime (see Sec. 5.3). Quantized cyclotron transitions have only recently been observed [53], and this thesis presents the first g value measurement using single-quantum cyclotron spectroscopy.

1.2.3 Sub-Kelvin Axial Temperature

The anomaly and cyclotron resonances acquire an inhomogeneous broadening proportional to the temperature T_z of the electron's axial motion (see Ch. 2). As discussed in Ch. 4, this broadening occurs because a magnetic inhomogeneity, the so-called "magnetic bottle", is introduced to allow detection of spin and cyclotron transitions. Finite temperature causes the electron to sample some range of this inhomogeneous B-field, resulting in an inhomogeneous broadening of the cyclotron and anomaly line shapes.

Cooling the axial temperature below the 5 Kelvin of previous g value measurements [54] narrows the cyclotron and anomaly line widths and yields improved precision of the Harvard g value measurement, in which $T_z \approx 300$ mK. When combined with our measurements of the electron's cyclotron temperature, this result demonstrates the coldest trapped elementary particle. The narrowing of resonance line shapes resulting from a colder axial temperature is shown in Fig. 1.5.

Axial cooling has also been achieved by the use of negative feedback, where a signal derived from the axial motion is sent back to the electron with the proper phase. This technique has been used to cool an electron in a 1.6 K environment to

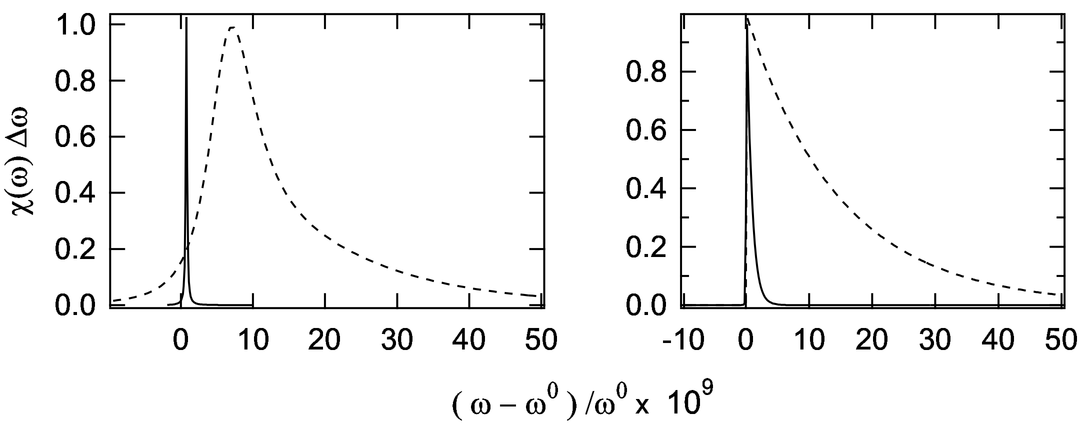

Figure 1.5: Theoretical anomaly (left) and cyclotron (right) line shapes for the 1987 University of Washington experiment [2] with $T_z = 5$ K (dashed) and for the 2004 Harvard experiment with $T_z = 300$ mK (solid). The frequency ω^0 corresponds to the resonance center in the limiting case of a 0 Kelvin electron, where the electron is motionless at the center of the trap.

$T_z = 700$ mK [55]. However, the 300 mK achieved by the brute force of a dilution refrigerator is colder, so feedback cooling was not used in the g value measurement presented in this thesis.

1.2.4 Cylindrical Penning Trap

The trap electrodes form a microwave cavity, and the standing-wave electromagnetic modes of this cavity interact with the cyclotron oscillator. Besides reducing the difficulty of machining the electrodes, there are two advantages of using cylindrical Penning traps rather than the hyperbolic Penning traps of previous g value experiments.

The first advantage is that the cavity modes of cylindrical traps are expected to have higher Q values and a lower spectral density than those of hyperbolic traps [56], allowing better detuning of the cyclotron oscillator from the nearest coupled mode. This detuning causes an inhibition of the cyclotron spontaneous emission [57] so that the lifetime is longer than the free-space value of ~ 0.1 s. The longest cyclotron lifetime reported in a hyperbolic trap is 1.2 s [58] whereas a lifetime of 13 s has been reported in a cylindrical trap [1]. The substantial enhancement of cyclotron lifetime in a high-Q cylindrical Penning trap makes possible the single-quantum spectroscopy used in this experiment.

The other advantage of using a cylindrical rather than a hyperbolic trap is that frequency-shift systematics can be better controlled. The same interaction between the cyclotron oscillator and the cavity modes which leads to inhibited or enhanced spontaneous emission also produces shifts in the cyclotron frequency. These shifts were the leading source of uncertainty in the 1987 University of Washington g value measurement [2].

As discussed in Ch. 5, in a cylindrical trap the cavity modes are the familiar and well characterized electromagnetic TE and TM modes. Calculated cavity shifts and cyclotron damping rates for the frequency region used for g value measurements in this thesis, based on the independently measured and identified mode spectrum of our trap, are shown in Fig. 1.6. An ideal g value measurement is performed approximately half-way between the well-separated cavity modes.

In this work, we demonstrate the first mapping of cyclotron lifetime versus detuning of the oscillator frequency from independently measured cavity modes (see Sec. 5.3). We observe the expected result that the cyclotron lifetime increases with detuning. Also, although g value shifts which vary with detuning from cavity modes

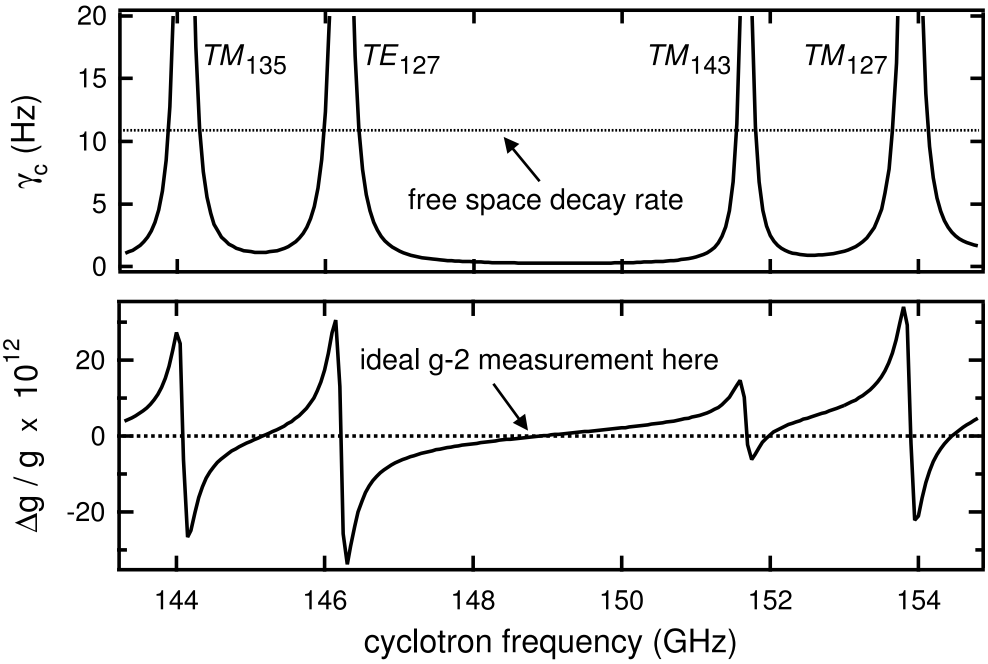

Figure 1.6: Calculated cyclotron damping rate and cavity shift for the cylindrical trap, based on the independently measured and identified cavity mode spectrum.

have long been expected [59], we present the first observation of this important effect. As shown in Ch. 6, our measurement of the g value shift agrees well with the prediction for the measured mode spectrum of the trap cavity, and this measurement is the first for which the appropriate cavity-shift correction is applied.

1.3 Recent Electron g value Measurements

The first g value measurements using free electrons [60], beginning in 1953, constituted a famous series of University of Michigan experiments. It was in these experiments that the idea of gaining three orders of magnitude in accuracy by measuring g - 2 rather than g was developed. The final version of the experiment [61] used bunches of a few thousand electrons in a magnetic mirror trap, where the relative difference in orientation between the precessing spin vector and the orbital momentum vector was directly observed. (Incidentally, observation of the difference between spin and orbital vectors is still the method used for muon g - 2 experiments [62].) These measurements culminated [63] in the reported value $g/2 = 1.001\ 159\ 656\ 700\ (3500)$.

The advent of single-electron detection in Penning traps [64] opened the way for precision study of single electrons, allowing huge improvements over the previous experiments in plasmas. Several generations of g value measurements were performed at the University of Washington, from 1977 [65] to 1999 [40], on single electrons in hyperbolic Penning traps. Experiments through 1987 at the University of Washington used traps with molybdenum electrodes. The first single-electron g value experiment, reported in 1977, measured the value $g/2 = 1.001\ 15\ 652\ 410\ (200)$; this result was limited by statistics and by the ability to correctly split the relatively broad line widths [65]. A subsequent g value measurement of the positron, reported in 1981, obtained $g/2 = 1.001\ 159\ 652\ 222\ (50)$; this result was limited by drive-shift systematics [50]. The most accurate result for the molybdenum traps obtained an accuracy of 4.3 ppt [2]. This 1987 result, $g/2 = 1.001\ 159\ 652\ 188.4\ (4.3)$, was limited by cavity-shift systematics (see Sec. 1.2.4 and Ch. 5). Beginning in 1990, a trap made from lossy phosphor bronze electrodes was used in order to reduce cavity shifts [54, 8]. The 1990 result, never published in a scientific journal, was $g/2 = 1.001\ 159\ 652\ 185.5\ (4.0)$ and was limited by non-gaussian scatter of g value results.

The preliminary Harvard 2004 measurement presented in this work is

$$\frac{g}{2} = 1.001\ 159\ 652\ 180\ 86\ (57), \tag{1.9}$$

currently limited to an accuracy of 0.6 ppt by knowledge of the cavity mode frequencies. As discussed in Sec. 5.4.2, the final choice of error assignment for this measurement is still under discussion and might be revised before publication. Comparison of the Harvard 2004 result with other recent g value measurements is shown in Fig. 1.3. Agreement with the 1990 University of Washington result is considered reasonable. The disagreement with the 1987 University of Washington result is nearly $2\,\sigma$. As discussed in Sec. 5.5, this rather large disagreement is likely due to an underestimate of cavity-shift effects in the 1987 University of Washington experiment.

Chapter 2

A Single Electron in a Sub-Kelvin Penning Trap

In this work, we report a preliminary result for a new measurement of the electron g value. With a preliminary assigned uncertainty of 0.6 parts per trillion (ppt), this result is the most accurate g value measurement to date. As with the best previous result [54], which achieved 4.0 ppt, we measure the cyclotron and anomaly frequencies of a single electron in a Penning trap. In this chapter we discuss the refrigerator, trap, and detection apparatus along with the dynamics of a single electron in the sub-Kelvin Penning trap. The low temperature achieved in the dilution refrigerator environment and the ability to resolve single-quantum cyclotron jumps, both discussed in this chapter, are crucial factors contributing to the accuracy of this result.

2.1 Refrigerator and Trap

In order to measure the properties of a sub-Kelvin electron, a cylindrical Penning trap is attached to the mixing chamber of a dilution refrigerator [53], shown in Fig. 2.3. The dilution refrigerator and trap fit inside the bore of a 5.5 Tesla superconducting solenoid.

A slightly earlier version of this apparatus was used [1] to make the first observation of the quantum limit of an electron in a magnetic field–a quantum cyclotron. Cooling the cyclotron oscillator to its ground state and observing single quantum jumps is a technique which plays a crucial role in the current experiment. Also, more recent versions of the apparatus were used to demonstrate electronic feedback cooling of a single electron [55] and the first single-particle self-excited oscillator (SEO) [66]. The SEO, useful because of its excellent frequency resolution, is used to monitor the electron's quantum cyclotron and spin states, as discussed in Sec. 2.3.4.

2.1.1 Penning Trap

In a Penning trap, charged particles are confined radially by a magnetic field and axially by an electrostatic potential applied to the electrodes. In this work, a closed endcap cylindrical trap geometry is used [67], as shown in Fig. 2.1. A basic biasing and detection schematic diagram is shown in Fig. 2.2.

The cylindrical geometry (as opposed to the hyperbolic geometry used in previous g value experiments) was chosen for its well-understood electromagnetic cavity mode structure, as discussed in Ch. 5. Gold-plated copper electrodes were used initially in this work, but they were replaced by gold-plated silver electrodes for reduced nuclear

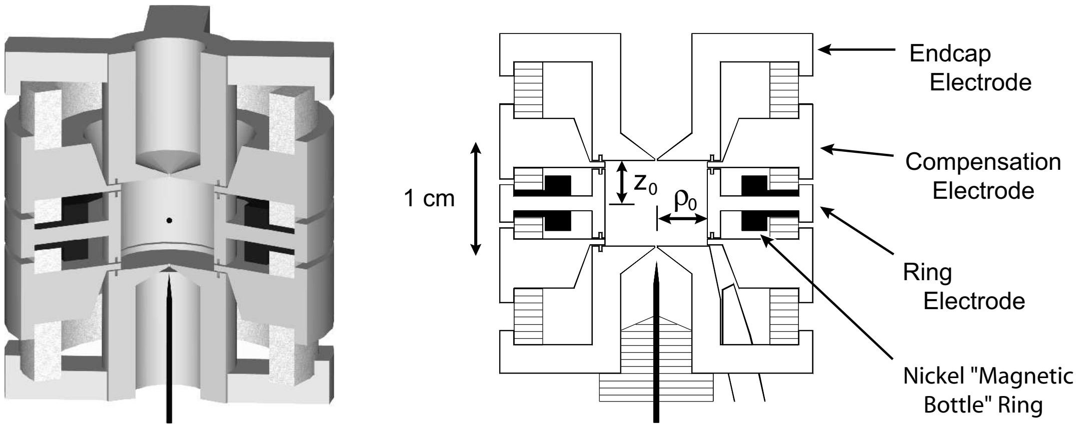

Figure 2.1: Three-dimensional (left) and two-dimensional (right) representations of trap.

paramagnetism, as discussed in Ch. 3.

2.1.2 Dilution Refrigerator and Magnet

One challenge is that the dilution refrigerator must fit inside a Nalorac 5.5 Tesla superconducting solenoid with exceptional spatial homogeneity ($< 10^{-8}$ over a 1 cm^3 sample), discussed in Ch. 3. The high field requirement and high homogeneity requirement along with cost constraints resulted in a 4 inch, 77 Kelvin magnet bore.

The requirements discussed above, along with the need to cool the dilution refrigerator to 4 K with cryogens separate from those for the magnet, result in a design with an impressive aspect ratio, shown in Fig. 2.3. The product used is an Oxford Kelvinox 300 dilution refrigerator, with a cooling power of 100 μW at 100 mK, specially designed for the Harvard precision experiments. To achieve a good magnetic environment for precision measurements, the refrigerator is composed of only copper, brass, and titanium (no stainless steel) below the refrigerator still.

2.1.3 Vacuum Enclosure

The Penning trap itself is enclosed within a dedicated indium-sealed vacuum "trap chamber" inside another vacuum enclosure–the inner vacuum chamber (IVC) of the dilution refrigerator. The Penning trap apparatus used originally in this work [53] was enclosed in a grease-sealed trap chamber. The advantage of the grease-sealed trap chamber was that it required a very small additional diameter in the premium real-estate market of our 3.0" inner-diameter IVC. This compact design allowed space for the so-called cold shield, which provides necessary radiation shielding for the mixing chamber if operating below 50 mK.

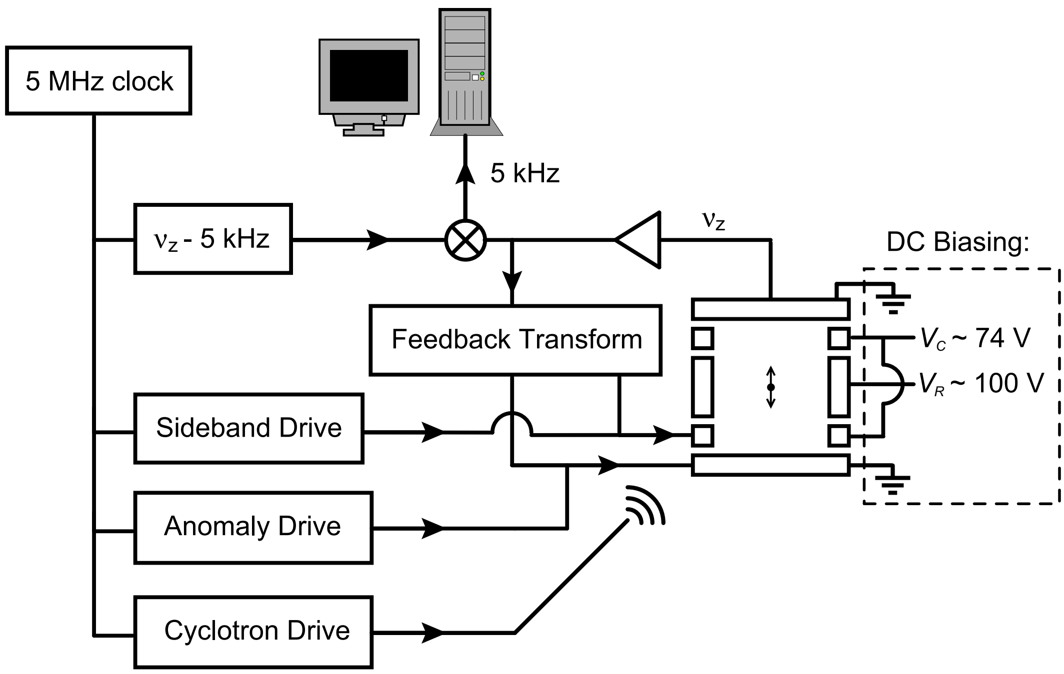

Figure 2.2: Basic schematic of drives, biasing and axial detection using the self-excited oscillator.

While this apparatus did prove capable of obtaining a vacuum good enough to trap and detect a single electron at 4 K, it required special attention if it was to

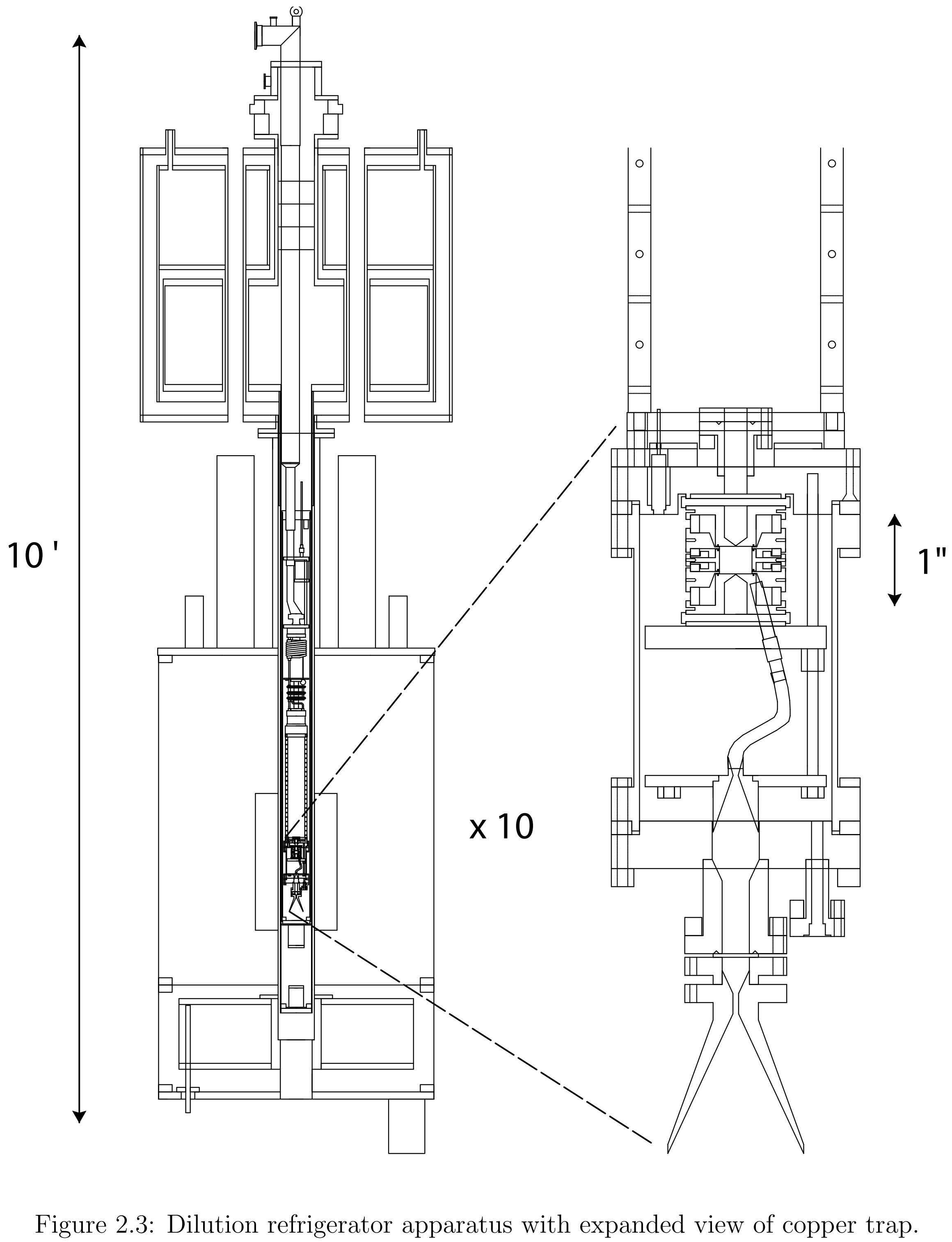

Figure 2.3: Dilution refrigerator apparatus with expanded view of copper trap.

operate properly. In addition, in its later years performance was intermittent and seemed to degrade, typically requiring operation below 2 K in order to achieve a good enough vacuum for single-electron work. The difficulties involving the grease-sealed trap chamber were largely due to the lack of a pressure differential holding the seal in place when the IVC was evacuated in order to run the refrigerator.

Over the course of this work, an indium-sealed copper trap chamber replaced the grease-sealed trap chamber. Eventually, for reasons discussed in Ch. 3, the copper chamber was replaced by an indium-sealed titanium trap chamber. Diagrams of the two types of trap chambers are shown in Fig. 2.4. The extra space required for the indium-seal designs required removal of the cold shield, limiting operation of the mixing chamber to temperatures above 50 mK.

Similar indium-sealed enclosures at 4 Kelvin have measured vacuums better than 5×10^{-17} Torr [68], which eliminates collisions between the trapped electron and background gas atoms seen in some experiments [64].

2.2 Electron Motions

An electron in a Penning trap has four resonance frequencies, corresponding to its three spatial degrees of motion (Fig. 2.5) plus spin. The Harvard g value experiment operates exclusively in the ground and first excited states of the spin and cyclotron degrees of freedom.

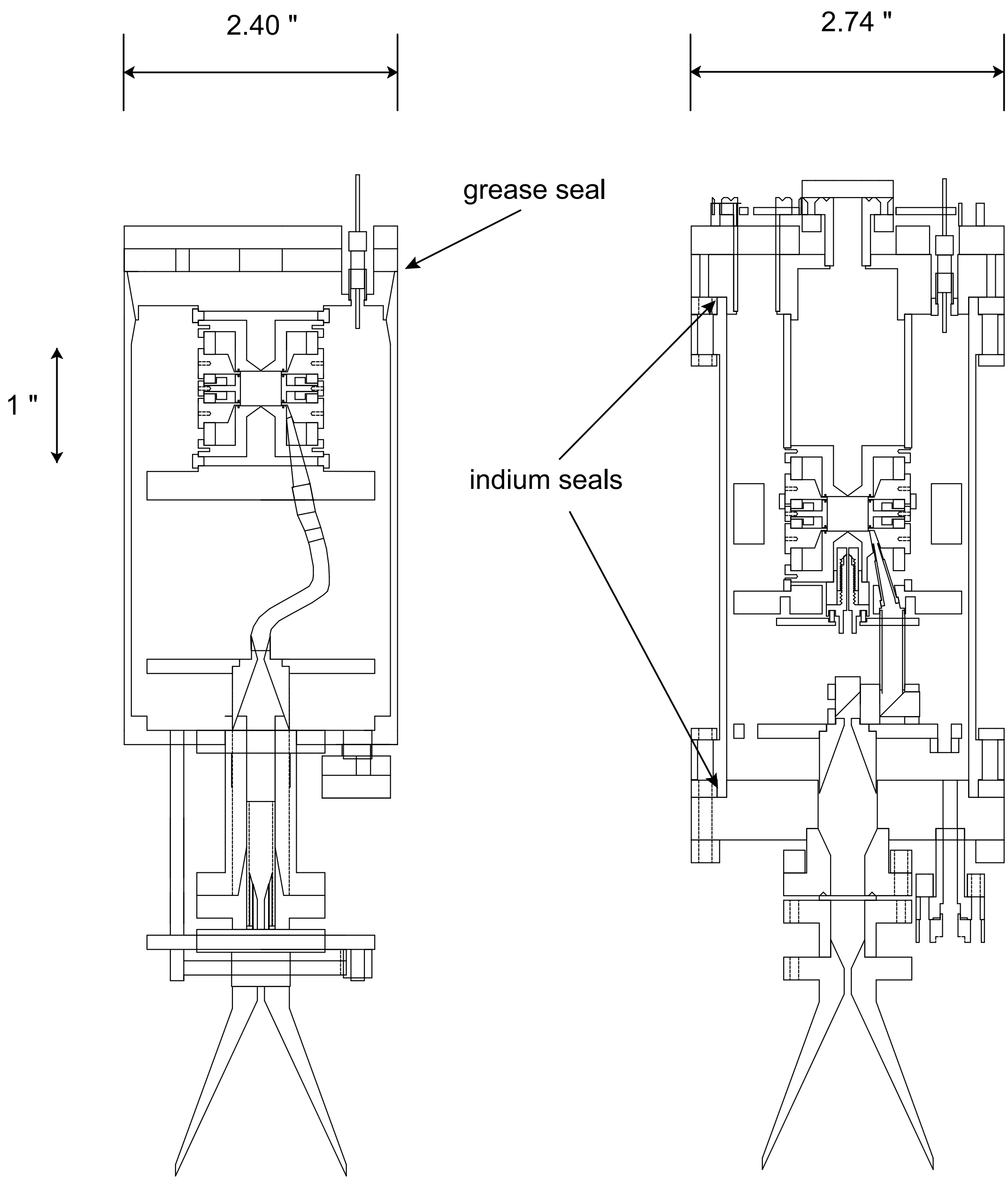

Figure 2.4: Grease-sealed copper trap chamber with copper electrodes (left) and indium-sealed titanium trap chamber with silver electrodes (right).

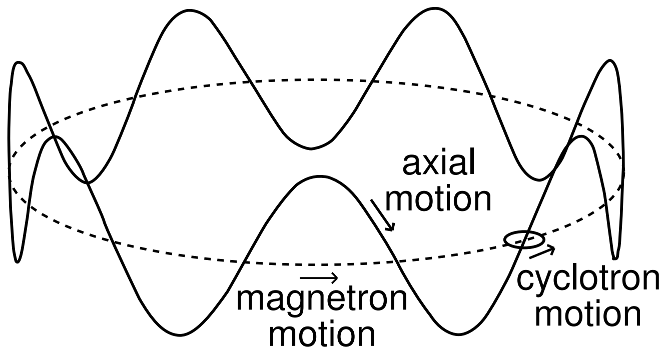

Figure 2.5: Motions of a single electron in a Penning trap.

2.2.1 Resonance Frequencies

The dynamics of a single electron in a Penning trap are well understood [69]. For a trapping potential V_R applied to the ring electrode (see Fig. 2.2), the axial frequency $\omega_z = 2\pi\nu_z$ is given by

$$\omega_z^2 = \frac{-qV_R}{md^2}(1 + C_2)\,, \tag{2.1}$$

where $q = -e$ is the electron charge and m is the electron mass. The characteristic trap dimension d is given by

$$d^2 = \frac{1}{2}\left(z_0^2 + \rho_0^2/2\right), \tag{2.2}$$

where the trap dimensions ρ_0 and z_0 are shown in Fig. 2.1. The magnetron frequency $\omega_m = 2\pi\nu_m$, corresponding to the slow $\vec{E} \times \vec{B}$ drift, is given by

$$\omega_m = \frac{\omega_z^2}{2\omega_c}\,. \tag{2.3}$$

Neglecting small corrections due to the electrostatic trapping potential of order $\omega_m/\omega_c \approx 10^{-6}$, the cyclotron frequency $\omega_c = 2\pi\nu_c$ is given by

$$\omega_c = \frac{|eB|}{m}, \tag{2.4}$$

where B is the magnetic field, and c is the speed of light. The spin frequency $\omega_s = 2\pi\nu_s$ is given by

$$\omega_s = \frac{g}{2}\omega_c\,, \tag{2.5}$$

where g is the electron g value.

The frequencies of the spatial motions of a single trapped electron are well separated. Sample oscillation frequencies and damping rates are shown in Table 2.1 for a

transition:	frequency:	$h\nu/k_b$:	damping:
magnetron	$\nu_m = 134.1$ kHz	$\frac{h\nu_m}{k_b} = 6.4\ \mu$K	$\frac{\gamma_m}{2\pi} \approx 10^{-17}$ Hz
axial	$\nu_z = 199.9$ MHz	$\frac{h\nu_z}{k_b} = 9.6$ mK	$\frac{\gamma_z}{2\pi} \approx 1$ Hz
cyclotron	$\nu_c = 149.0$ GHz	$\frac{h\nu_c}{k_b} = 7.2$ K	$\frac{\gamma_c}{2\pi} \approx 0.02$ Hz
spin	$\nu_s = 149.2$ GHz	$\frac{h\nu_c}{k_b} = 7.2$ K	$\frac{\gamma_s}{2\pi} \approx 10^{-12}$ Hz

Table 2.1: Trapped electron frequencies and damping rates for $V_R = 101.3$ V, $V_C = 74.0$ V, and a representative magnetic field value.

trapping potential V_R near 100 V. Only the cyclotron motion has significant natural damping, and this damping is suppressed by a factor of up to 100 by the microwave cavity formed by the trap electrodes [1]. The axial motion is damped by the tuned circuit used for its detection.

2.2.2 Quantization

Perhaps the most important innovation of this experiment is that the spin and cyclotron motions are entirely quantum mechanical. The level diagram for all four motions is shown in Fig. 2.6.

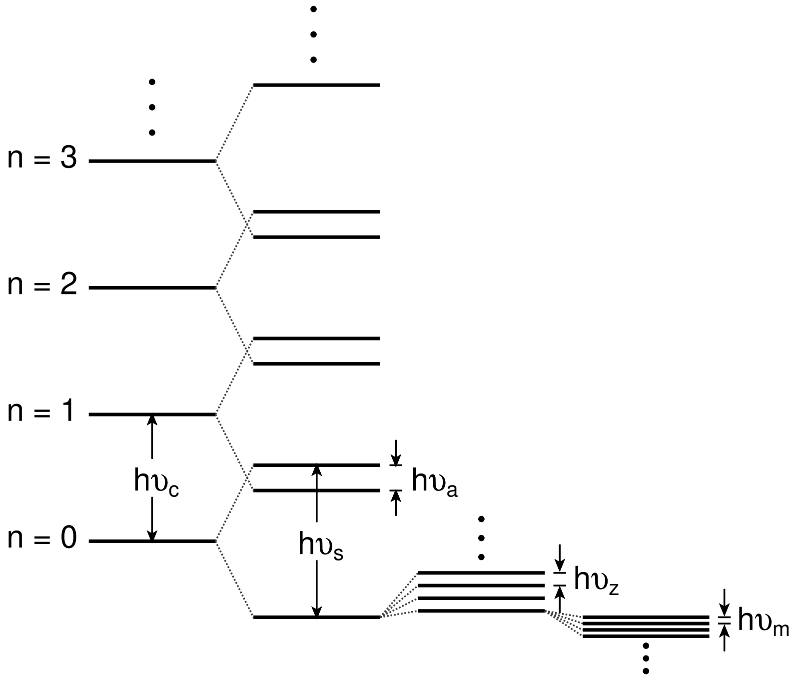

Figure 2.6: Energy levels of the four oscillation frequencies of a single electron in a Penning trap: cyclotron (ν_c), spin (ν_s), axial (ν_z), and magnetron (ν_m). The so-called anomaly transition, at frequency ν_a, involves simultaneous spin and cyclotron transitions.

Because of the low temperature achieved with the dilution refrigerator, the cyclotron oscillator decays by synchrotron radiation to its ground state and remains there until excited by a photon sent from outside the refrigerator. The spin state has a very long life time, so it does not change states unless excited by a drive. This exquisite quantum control allows the g value experiment presented here to be performed in only the three lowest energy levels of spin and cyclotron motions. This degree of quantum control allows serious complications involving relativistic corrections of classical cyclotron spectroscopy to be completely avoided.

2.3 Detection

Unlike the cyclotron and spin frequencies, the axial frequency is low enough that it is practical to build cryogenic radio-frequency (rf) amplifiers (see Sec. 2.3.2) for detection of axial oscillations. Coupling to the axial motion, discussed in Sec. 2.3.7, allows magnetron, cyclotron, and spin energy changes to be detected as shifts in the axial frequency.

2.3.1 Synthesizers and Clocks

A PTS (Programmed Test Source) synthesizer is used to generate the anomaly drive at $\sim$ 170 MHz, by which spin-flip transitions are driven (see Ch. 6). The thirteenth harmonic output of a GaAs Schottky-barrier diode, driven by an 11 GHz signal from an Agilent E8251A synthesizer, is used to excite cyclotron transitions at $\sim$ 150 GHz. Both PTS and Stanford Research Systems synthesizers are used to generate the reference drive (at ν_z - 5 kHz) used for mixing down the axial oscillation output signal.

As shown in Fig. 2.2, synthesizers which generate the anomaly and cyclotron drives and the ν_z - 5 kHz reference were all tied to the same 10 MHz rubidium clock for the data taken with a cyclotron frequency $\nu_c = 149.0$ GHz. For some of the data taken at $\nu_c = 146.8$ GHz, the 11 GHz synthesizer was on a separate ground, and the clocks were not tied together to avoid problems with ground loops. For this data, relative drift of the two clocks was regularly monitored, and corrections were applied upon analysis.

As discussed in Sec. 6.1, a g value measurement in a Penning trap entails taking a ratio of frequencies. Thus, the absolute accuracy of the 10 MHz clock is not important, as long as all synthesizers use the same clock and the clock is stable over the course of the measurement.

However, the absolute accuracy of the reference clock is important in the calibration of cavity mode spectra discussed in Ch. 5. An absolute measurement of cyclotron frequency at different magnet currents is used as a measurement of magnetic field. This calibration determines the best estimate of trap dimensions and is used in calculating cavity shift systematic error. The absolute accuracy of the 10 MHz clock used for the mode spectrum measurements was found to be better than 100 parts per billion (ppb), which is well below the error in mode map calibration introduced by other issues.

2.3.2 Cryogenic Amplifiers

Monitoring the current of a driven electron in a Penning trap, although an impressive feat, is routinely accomplished using cryogenic field effect transistors (FETs). Recent improvements in the amplifier design [70, 71] include the use of high electron-mobility transistors (HEMTs) and the addition of a second-stage amplifier, and operation at $\nu_z = 200$ MHz (as compared with the earlier $\nu_z = 60$ MHz).

The first-stage amplifier, depicted in Fig. 2.7, is located near the trap chamber. Its coaxial input extends into the trap can and forms a resonant circuit at 200 MHz. The resonator consists of a length of coaxial cable (shorter than $\lambda/4$ so that it behaves like an inductor) with the trap capacitance added on one end and with the opposite end shorted.

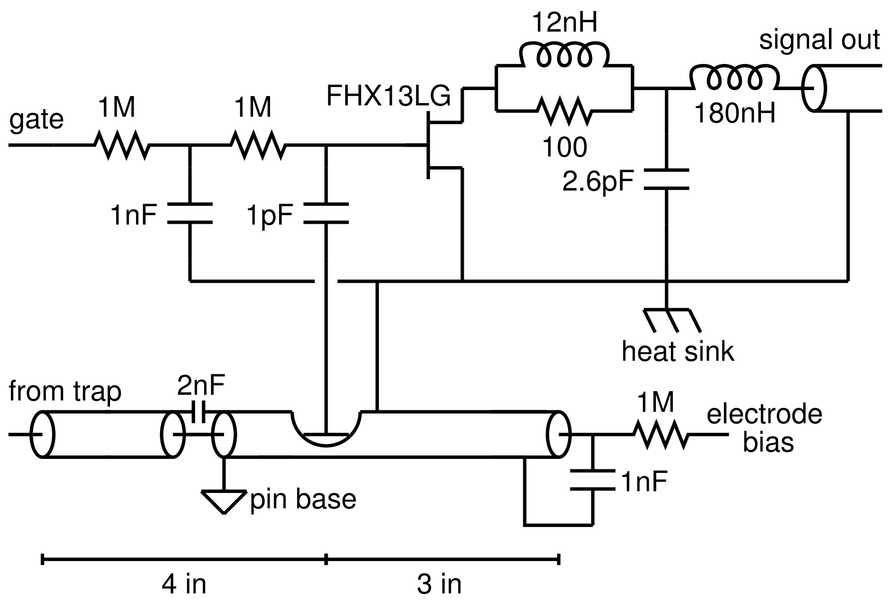

Figure 2.7: First stage 200 MHz amplifier schematic. Values without units are resistances in ohms.

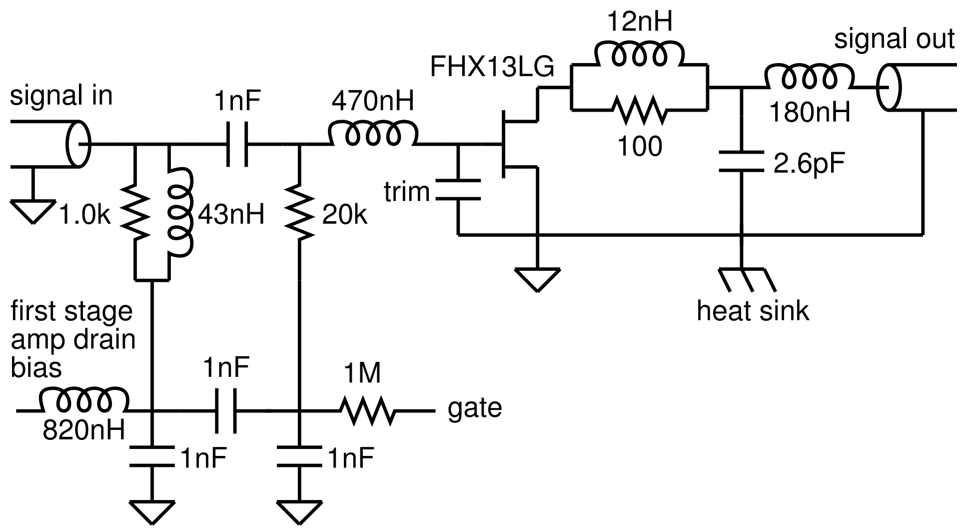

Figure 2.8: Second stage 200 MHz amplifier schematic. Values without units are resistances in ohms.

The second-stage amplifier improves the detection signal-to-noise-ratio (SNR) by boosting the 200 MHz signal before it arrives at the room-temperature amplifier, which has an input noise temperature of about 70 K. The second-stage amplifier is placed at a 600 mK stage of the refrigerator, where it can dissipate more power than an amplifier at the mixing chamber, but where the signal from the first-stage amplifier has been attenuated by only about 10 dB by the thermally insulating stainless coax running the length of the cryogenic experiment. Fig. 2.8 shows the schematic diagram of the circuit.

2.3.3 Externally-Driven Axial Detection

If one of the trap electrodes is driven with an rf voltage resonant with the electron axial motion, the electron signal at the first-stage amplifier input can exceed the

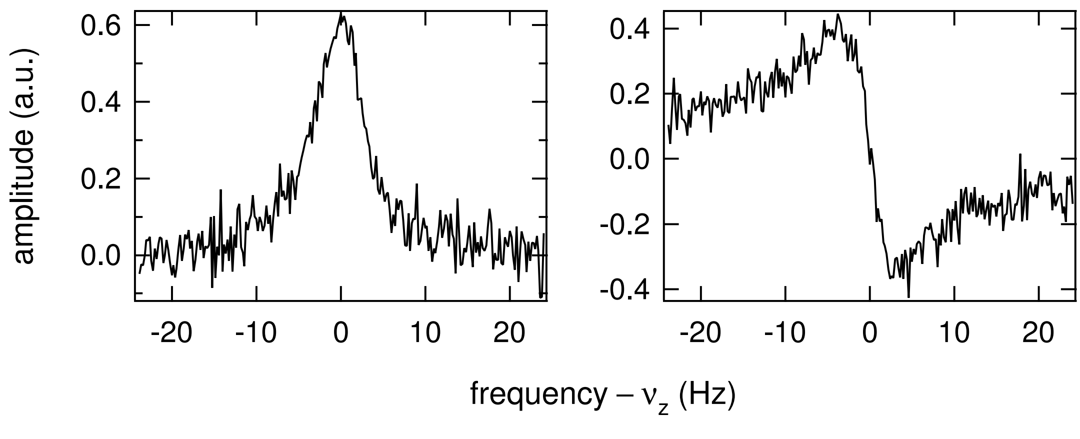

Figure 2.9: In-phase (left) and quadrature (right) driven axial response of a single electron with $\nu_z \approx 60$ MHz.

amplifier input noise after less than a second of averaging. The driven axial response of a single electron is shown in Fig. 2.10. For $\nu_z \approx 200$ MHz, the trapping potential is not currently stable enough to make a clean map of the resonance, since drift of the trapping potential shifts the resonance frequency on the order of a line width over a time scale comparable to that required for signal averaging [70].

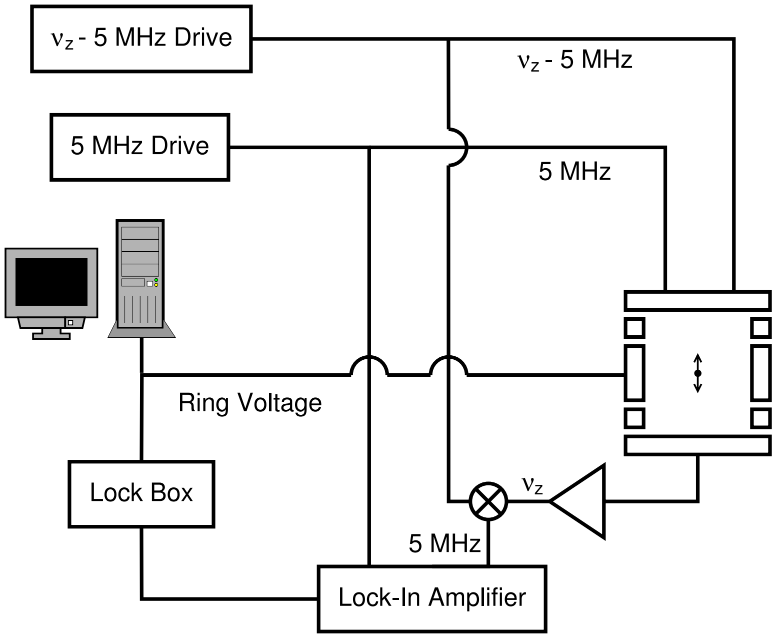

Figure 2.10: Schematic diagram for externally-driven axial detection.

Fig. 2.10 shows a schematic diagram for driven detection using an external rf source. In order to avoid direct feedthrough of the drive into the amplifier, rather than driving the electrode at ν_z, it is driven at both ν_z- 5 MHz and at 5 MHz. The result of the 5 MHz drive can be thought of as modulating the trapping potential, creating a sideband with which the ν_z- 5 MHz drive is resonant.

2.3.4 Self-Excited Axial Detection

Instead of driving the axial motion with an external source, positive feedback may be used to create a self-excited oscillator (SEO) [66, 70]. A schematic diagram for

SEO detection is shown in Fig. 2.2. The amplitude of oscillation is limited by a Digital Signal Processor (DSP), which is programmed to control a voltage-variable attenuator such that the signal amplitude (proportional to the amplitude of the electron oscillation) is kept constant.

In SEO detection, the problem of drive feedthrough to the amplifier is suppressed by splitting the feedback signal. One feedback drive is applied to the bottom endcap electrode, and the other feedback drive is applied to a compensation electrode. The relative amplitude and phase of the two feedback signals is adjusted such that the feedthrough signals at the amplifier cancel. The overall feedback signal seen by the

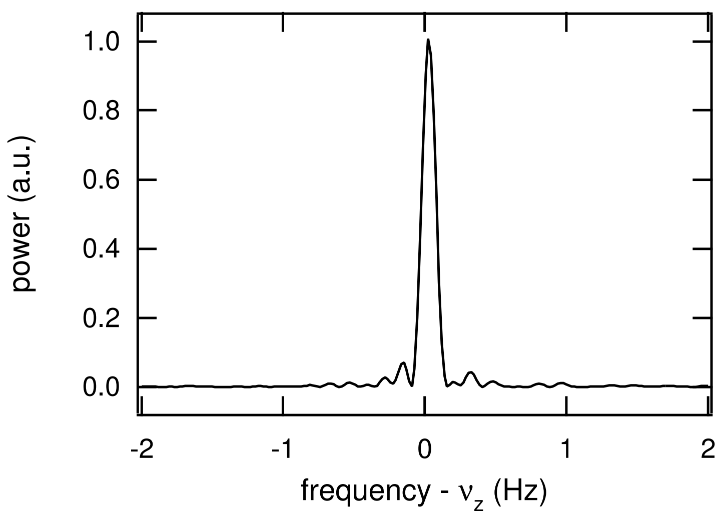

Figure 2.11: FFT of the detected self-excited oscillator axial signal at $\nu_z \approx 60$ MHz, with an 8 second square window.

electron, however, does not cancel and causes self-excitation if its phase is properly adjusted. A typical SEO response of a single electron is shown in Fig. 2.11.

The principle advantage of the SEO is that it allows axial detection to be performed under conditions where the electron is driven to very large axial excitations

[66]. Real Penning traps are anharmonic, despite careful efforts to reduce the anharmonic terms of the potential. Typically, a Penning trap is tuned so that the trap is locally harmonic about a vanishing excitation amplitude. Under these conditions, if the electron is driven to large amplitudes, it will eventually experience large frequency shifts as the anharmonic terms become significant.

On the other hand, the SEO is able to maintain an oscillation even in an anharmonic potential. The trap is tuned such that there is a locally harmonic potential at a large excitation amplitude. An external drive would not be able to follow the electron's oscillation frequency in order to excite it to this harmonic region. However, the SEO does so automatically if the DSP is programmed to lock the amplitude in the desired region.

Operating in this mode, large signals of the axial oscillator are available. This allows quantum jump detection (see Sec. 2.3.7) under conditions more favorable for g value measurements. One potential disadvantage of the SEO is that the electrostatic potential is locally anharmonic in the zero-temperature limit, near where g value measurements are performed. This issue, not currently a limitation, is discussed in Sec. 6.2.2.

2.3.5 Parametric Axial Detection

The axial oscillation at ν_z of trapped electrons is phase bistable to parametric excitation, i.e. excitations at twice ν_z [72]. However, above a sharp threshold in drive strength, a cloud of electrons spontaneously breaks this symmetry and synchronizes its axial oscillation. As discussed in Ch. 5, the degree of synchronization depends sensitively on the overall damping rate, making this technique a useful probe of the electromagnetic cavity mode structure [73].

When driving above threshold sufficiently near a cavity mode [74], the response at ν_z exhibits hysteresis in the sweep direction of the parametric drive [73]. If the anharmonicity term [69] C_4 is positive, a parametric drive swept down in frequency creates a large excitation at a well-defined frequency [73], as shown in Fig. 2.12. When

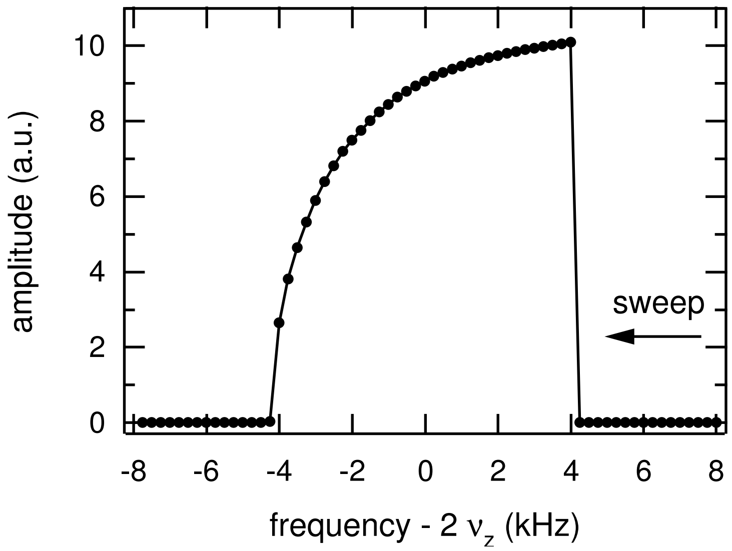

Figure 2.12: Parametric resonance of a cloud of 3 $\times 10^4$ electrons. Drive is above threshold and swept down in frequency.

this technique is used to map the electromagnetic cavity modes of the trap, the parametric drive is set above threshold at near $2\nu_z$.

2.3.6 Magnetron Excitation Detection

For precision measurements, the magnetron motion is reduced by so-called "side-band cooling" [69], where the unstable magnetron motion is pushed to the top of its potential hill by being coaxed to take energy from the axial frequency. In the unusual case of the magnetron motion, the shape of the potential is such that the maximum energy corresponds to the smallest radius, which is desirable for precision experiments.

To experimentally find the magnetron frequency, a sideband heating drive (which will cause the magnetron orbit to expand if it is resonant) at $\nu = \nu_z - \nu_m$ is applied to an electrode with the proper geometry [56]. The axial frequency shift caused by an increase in magnetron orbit can be observed, as shown in Fig. 2.13. In this figure, ν_z continues to shift as long as the drive is resonant with the heating sideband.

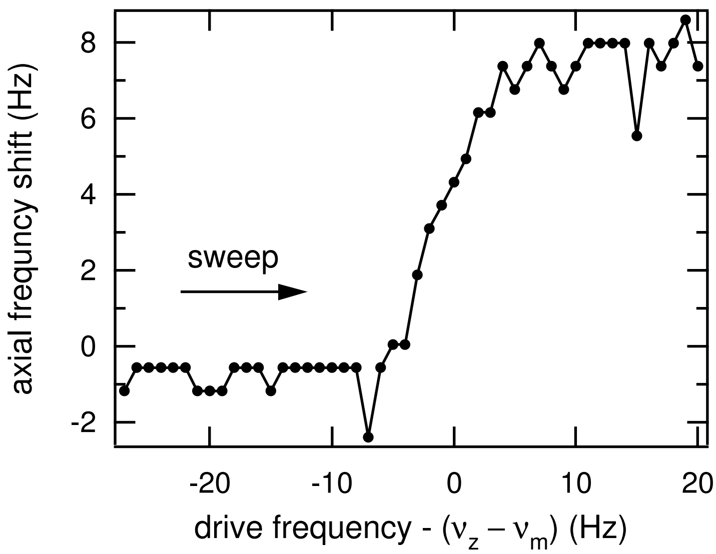

Figure 2.13: Response of a single electron (with $\nu_z \approx 200$ MHz) to a drive near the sideband heating frequency $\nu_z - \nu_m$. The drive is swept up in frequency.

When the magnetic field value is changed, a search for the cyclotron frequency can be time-consuming, especially if proton NMR (see Ch. 3) was not performed at the new field. In these cases, it saves time to find the magnetron frequency ω_m and then use Eq. (2.3) to estimate the experimental cyclotron frequency $\bar{\omega}_c$.

In this work, we found that the observed frequency $\overline{\omega}_c$ was typically larger than the value predicted from the observed magnetron frequency $\overline{\omega}_m$ by 50 to 150 ppm. The magnitude and sign of this disagreement contains information about the imperfections of the Penning trap [56], discussed in Sec. 6.2.7.

2.3.7 Cyclotron and Spin Transition Detection

A one-quantum change in cyclotron or spin energy can be clearly resolved [1] as a shift in ν_z, if a sufficiently large "magnetic bottle" is incorporated into the trap [75, 76]. Examples of quantized spin and cyclotron transitions are shown in Fig. 2.14 and Fig. 2.15, respectively.

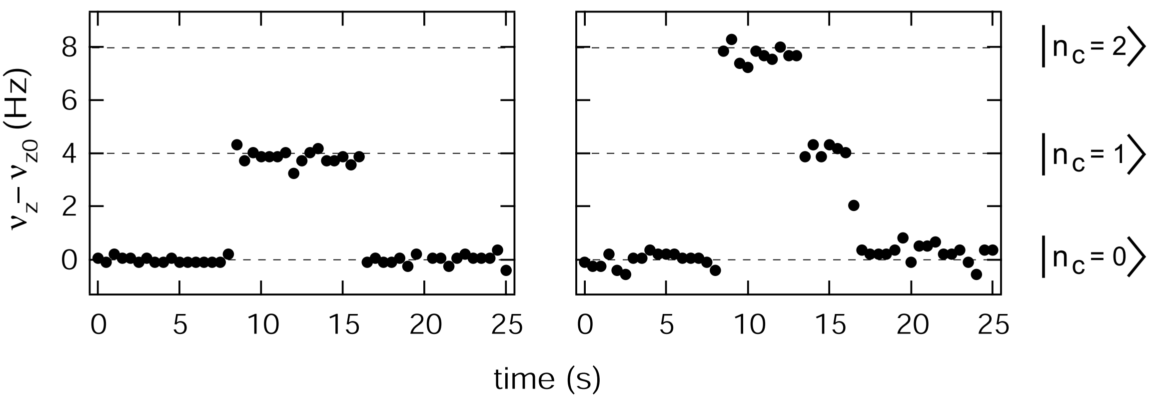

Figure 2.14: Axial frequency shift (with $\nu_z \approx 200$ MHz) caused by quantum cyclotron transitions of a single electron between the ground and first excited state (left) and between the ground and first two excited states (right).

The magnetic bottle is created by placing nickel rings (see Fig. 2.1) above and below the center of the trap. These ferromagnetic rings acquire a saturated magnetization described by a multipole expansion [69], given by

$$\vec{B}_b(\vec{r}) = \sum_{l=0}^{\infty} B_l r^l \left[P_l(\cos\theta)\hat{z} - (l+1)^{-1} P_l^1(\cos\theta)\hat{\rho} \right], \tag{2.6}$$

where P_l and P_l^1 are Legendre and associated Legendre polynomials. If the rings are symmetric under $z \to -z$, only the B_l with even l are non-vanishing. The expansion of Eq. (2.6) then becomes

$$\vec{B}_b(\vec{r}) = B_0\hat{z} + B_2\left[\left(z^2 - \frac{\rho^2}{2}\right)\hat{z} - (z\rho)\hat{\rho}\right] + B_4\left[\mathcal{O}(r^4)\right] + \dots \tag{2.7}$$

Henceforth, we shall refer to the "magnetic bottle" ΔB as the $\hat{z}$ component of the leading-order non-homogeneous term

$$\Delta B = B_2\left(z^2 - \frac{\rho^2}{2}\right). \tag{2.8}$$

The potential energy U of an electron with total magnetic moment $\mu_z = \vec{\mu}\cdot\hat{z}$ at $\rho = 0$ in the combined electrostatic and magnetic potential well is then given by

$$U = \frac{m\omega_{z0}^2 z^2}{2} - \mu_z B_2 z^2, \tag{2.9}$$

where $\omega_z 0$ is the axial frequency for $B_2 \to 0$. The overall spring constant k is then given by

$$k = m\omega_{z0}^2 - 2\mu_z B_2 \tag{2.10}$$

It is clear from Eq. (2.10) that the axial oscillation frequency ω_z depends on the magnetic moment of the electron.

In terms of the cyclotron and spin quantum numbers $n_c = 0, 1, 2, \dots$ and $n_s = 0, 1$, the total magnetic moment (see Sec. 2.2.2) can be expressed as

$$\mu_z = -2\mu_B(n_c + \frac{1}{2}) - g\mu_B(n_s - \frac{1}{2}). \tag{2.11}$$

Using $g \approx 2$ and $\mu_z B_2 \ll m\omega_z^2$, Eqs. (2.10) and (2.11) give

$$\omega_z \approx \omega_{z0}\left[1 + \frac{2B_2\mu_B}{m\omega_{z0}^2}(n_c + n_s)\right]. \tag{2.12}$$

The magnetic-bottle coupling to the axial detection circuit performs a quantum non-demolition (QND) measurement on the cyclotron and spin states, so a continuous series of measurements yield the same quantum state. As shown in Figs. 2.14 and 2.15, single-quantum cyclotron and spin transitions result in shifts in ν_z of about 4 Hz, in good agreement with Eq. (2.12) for the independently measured bottle $B_2 = 1540$ T/m^2.

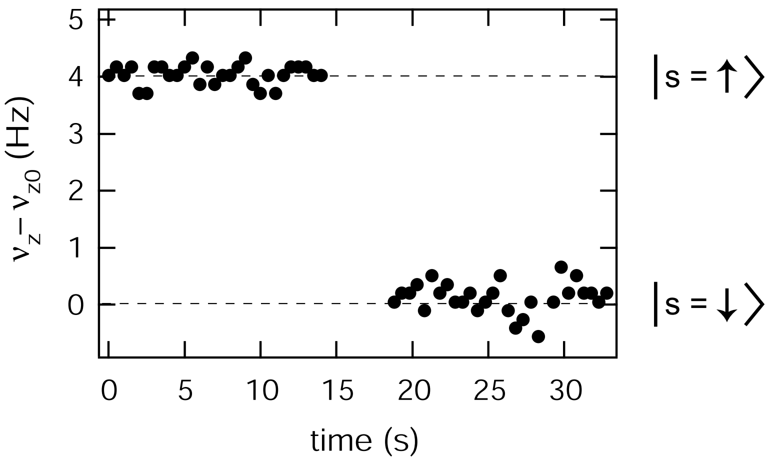

Figure 2.15: Axial frequency shift (with $\nu_z \approx 200$ MHz) caused by a spin flip transition of a single electron. The gap in data is for the drive pulse and SEO recovery time.

If the magnetic field is chosen such that ω_c is well-detuned from coupled cavity modes (see Ch. 5), the cyclotron lifetime τ_c can be much greater than the free-space cyclotron lifetime of ~ 0.1 s. This allows a magnetic bottle of a moderate size to be used for detection of single-quantum cyclotron transitions, and novel quantum-jump spectroscopy can be used to map the cyclotron line shape. Advantages of single-quantum cyclotron spectroscopy are discussed in Ch. 4. Unfortunately, coupling between the axial motion and the cyclotron and spin motions also has deleterious effects on a g value measurement; the cyclotron and anomaly lineshapes are thermally broadened in proportion to the strength of the coupling (see Sec. 4.2). For this reason, it is desirable to use a small magnetic bottle or a higher axial frequency (see Sec. 4.4) to make the cyclotron jump size as small as possible.

Chapter 3

Magnetic Field Stability

To lowest order, the g value measurement described in Chapter 6 does not depend on the details of the confining magnetic field. Measurement of the cyclotron frequency serves as a magnetometer, and measurement of the anomaly frequency in the known field determines g. In practice, measuring the cyclotron and anomaly frequencies takes several hours, so the temporal stability of the magnetic field is very important. To achieve a high stability, the trap center must not move significantly relative to the homogeneous region of the trapping field. Also, the magnetism of the trap materials themselves must be stable.

3.1 Monitoring the Magnetic Field

The sharp low-frequency edge of the near-exponential cyclotron line shape (see Ch. 4) serves as a convenient magnetometer. The algorithm for "edge-tracking", simply consists of increasing a microwave drive frequency until a cyclotron quantum jump occurs, recording that frequency, and then resetting the drive frequency to a lower value. In the exponential limit, the width of the edge is much smaller than the linewidth, so this technique yield sub-linewidth field measurements. Magnetic field stability is monitored by this technique.

3.2 Achieving Stability in the External Field

In order to achieve stability in the external B-field, the homogeneous region of the field is made large as possible, and efforts are made to keep the trap center from moving. We adjust a set of superconducting shim coils to achieve a homogeneity of about 1×10^{-8} per cm^3, as measured by the width of the NMR resonance of a water-filled 1 cm^3 probe.

3.2.1 Pressure regulation

It has been observed in previous Penning trap experiments [77] that regulation of the gas pressures above the cryogen baths plays a crucial role in obtaining a highly stable B-field. We regulate the gas pressure over each of the five cryogen baths separately, to better than 1 mpsi. By allowing pressures to drift slowly while monitoring the field stability, it has been determined that pressure regulation to this level is sufficient to regulate the magnetic field to better than 0.5 ppb.

3.2.2 Temperature Regulation

As the temperature of the dewar changes, the aluminum sides of the dewar undergo thermal contraction and expansion. In cases of a poorly shimmed magnet, the effects are clearly observable in the edge-tracking frequency, as shown in Fig. 3.1.

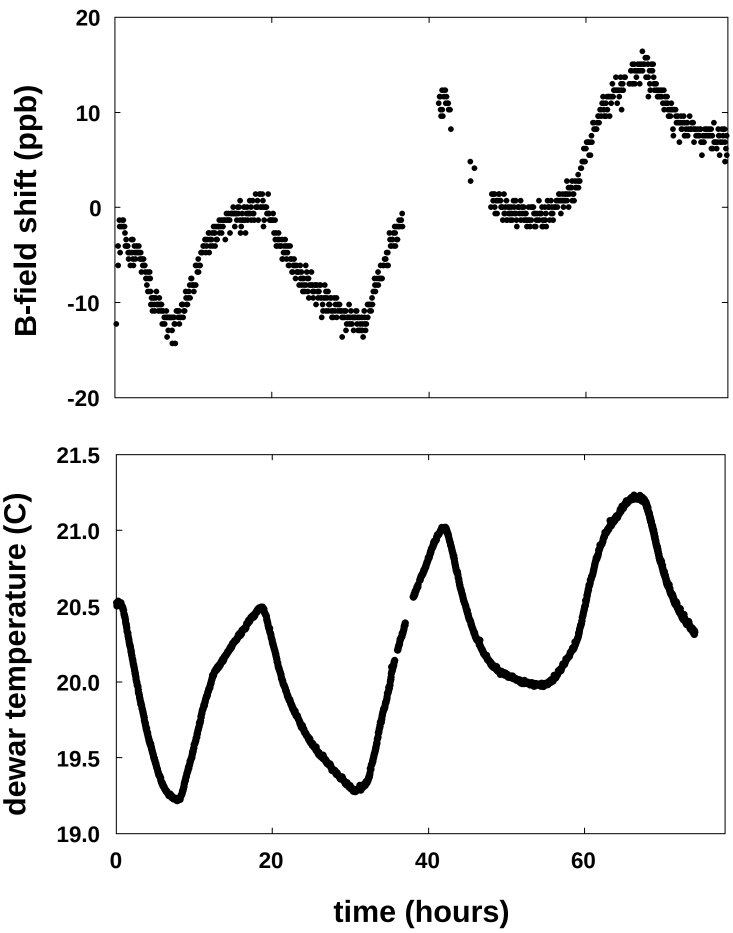

Figure 3.1: Thermal cycles of magnetic field when shimming was not good and the temperature of the dewar was not regulated.

To reduce thermal fluctuations of the trap position, the entire dewar and magnet are enclosed in an insulated shed [78], which uses forced-air circulation to maintain thermal equilibrium. The temperature is regulated using a water-circulation system that forces water from a heated bath through a radiator located in the shed. A lock loop regulates the temperature at a thermometer within the shed by heating or cooling the bath. This technique has demonstrated temperature stability within the shed of better than 0.1 K over 24-hour cycles within the shed, while the temperature of the room fluctuated by 1 to 2 K.

3.2.3 Adjustable Spacer

In order to guarantee that the trap center was located at the homogeneous region of the B-field, an adjustable-height spacer was added to the experiment [79] . The cyclotron frequency of a single electron is used to measure the field as the spacer height is adjusted, as shown in Fig. 3.2. The spacer height is then adjusted such that the trapped electron is at the local field minimum.

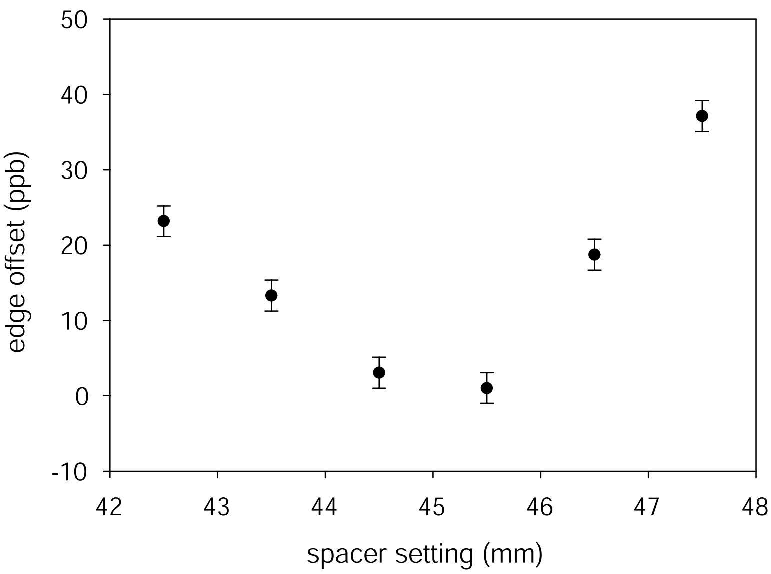

Figure 3.2: Map of field profile along $\hat{z}$ axis made by measuring the cyclotron frequency of a single electron versus spacer height.

3.2.4 Realized Field Stability

The various efforts discussed in this section contribute to a marked improvement (Fig. 3.3) in field stability compared to the poor stability shown in Fig. 3.1. For the g value measurements at $\nu_c = 146.8$ GHz, B-field stability was typically better than 1 ppb over 12 hours. Large field fluctuations shown in Fig. 3.3 correspond to work hours, on weekdays and Saturdays, of a nearby construction project.

Unfortunately, during the g value measurements at $\nu_c = 149.0$ GHz, the magnet exhibited a large drift. After two months of settling time, the drift was still on the order of 0.5 ppb per hour. Fortunately, the improvements discussed in this section prevent additional short-term variations of the field, so the linear component of the drift can be accounted for in g value measurements, as discussed in Sec. 4.5.4.

3.3 Achieving a Stable Trap Magnetism

Paramagnetic materials exhibit magnetism which follows the Curie law:

$$B = \frac{\lambda}{T}, \tag{3.1}$$

where λ is the curie constant for the material. In the g value experiments discussed here, the quantity of concern is not the magnetization itself, but its stability versus small temperature changes. Thus, the quantity of concern is

$$\left|\frac{dB}{dT}\right| = \frac{\lambda}{T^2}. \tag{3.2}$$

As we shall see, the T^{-2} sensitivity to temperature fluctuations causes some materials which are innocuous in a helium-temperature experiment to become highly problematic in a dilution refrigerator experiment. Eq. (3.2) shows that if the magnetism of a

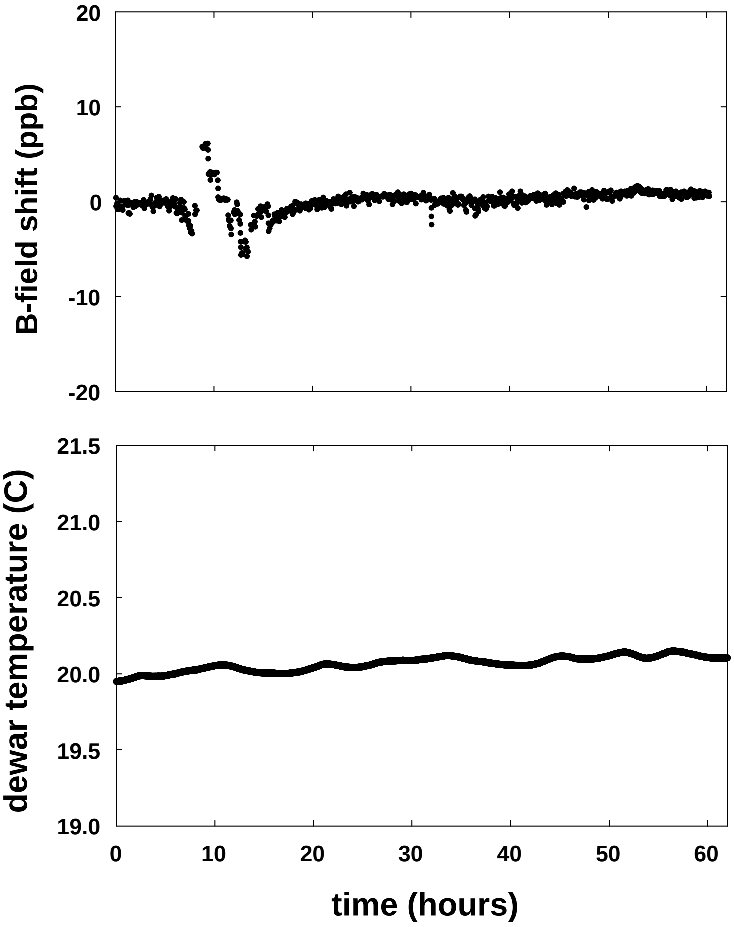

Figure 3.3: Stability of the B-field achieved by pressure and temperature regulation, shimming, and positioning of the trap center at the shimmed location. The zero of the x-axis corresponds to midnight. The noisy portions are during construction hours, where the relatively large field fluctuations are most likely due to shifts of the trap center induced by vibrations.

material follows the Curie law, its sensitivity to temperature fluctuations is a factor of 16 worse at 1 K than at 4 K.

Electronic paramagnetism is a well-known problem for cryogenic precision experiments sensitive to the magnetic environment. In one case, a G-10 support tube which was poorly thermally anchored caused field instabilities of worse than 1×10^{-6} at the center of a solenoid in a system which was designed for a stability of better than 1×10^{-10} [80]. In another case, the original molybdenum electrodes of a g value experiment were replaced by copper electrodes, because of the larger electronic paramagnetism of molybdenum [69]. (Since molybdenum is a metal, the paramagnetism of pure molybdenum is negligible [81]. However, some reports [82] have shown a large inverse-temperature dependence of molybdenum magnetism, which is presumably due to impurities.)

In previous experiments at 4 K, nuclear paramagnetism could be ignored since it is suppressed below electronic paramagnetism by a factor of $(\mu_N/\mu_B)^2 \sim 10^5$, where μ_N is the nuclear magneton and μ_B is the Bohr magneton. However, below 1 Kelvin, electronic paramagnetism saturates in a field of a few Tesla and nuclear paramagnetism becomes important. Table 3.1 lists the curie constants for nuclear paramagnetism of several materials.

3.3.1 Copper Trap

Unaware of the importance of nuclear paramagnetism in a sub-Kelvin g value measurement, we began work on this experiment using a Penning trap and accompanying apparatus constructed primarily of OFHC copper. The insulating spacers between

material:	λ (μK):
Ag	0.0020
Al	0.86
Au	0.0016
Be	0.22
Brass (70-30)	0.38
Cu	0.56
In	1.1
Mo	0.015
Ni	0.00072
Pb	0.0057
Sn	0.015
Ti	0.0066
Zn	0.0022
Fused Quartz	0.0022
G-10 (FR-4)	0.94
MACOR	0.15
Sapphire	0.68
Teflon	0.86

Table 3.1: Nuclear curie constants for various metals and insulators with naturally occurring isotopic abundances

electrodes were made from MACOR, a machineable ceramic which is unfortunately rich in aluminum (see Table 3.1). A diagram of the copper trap apparatus is shown in Fig 3.4.

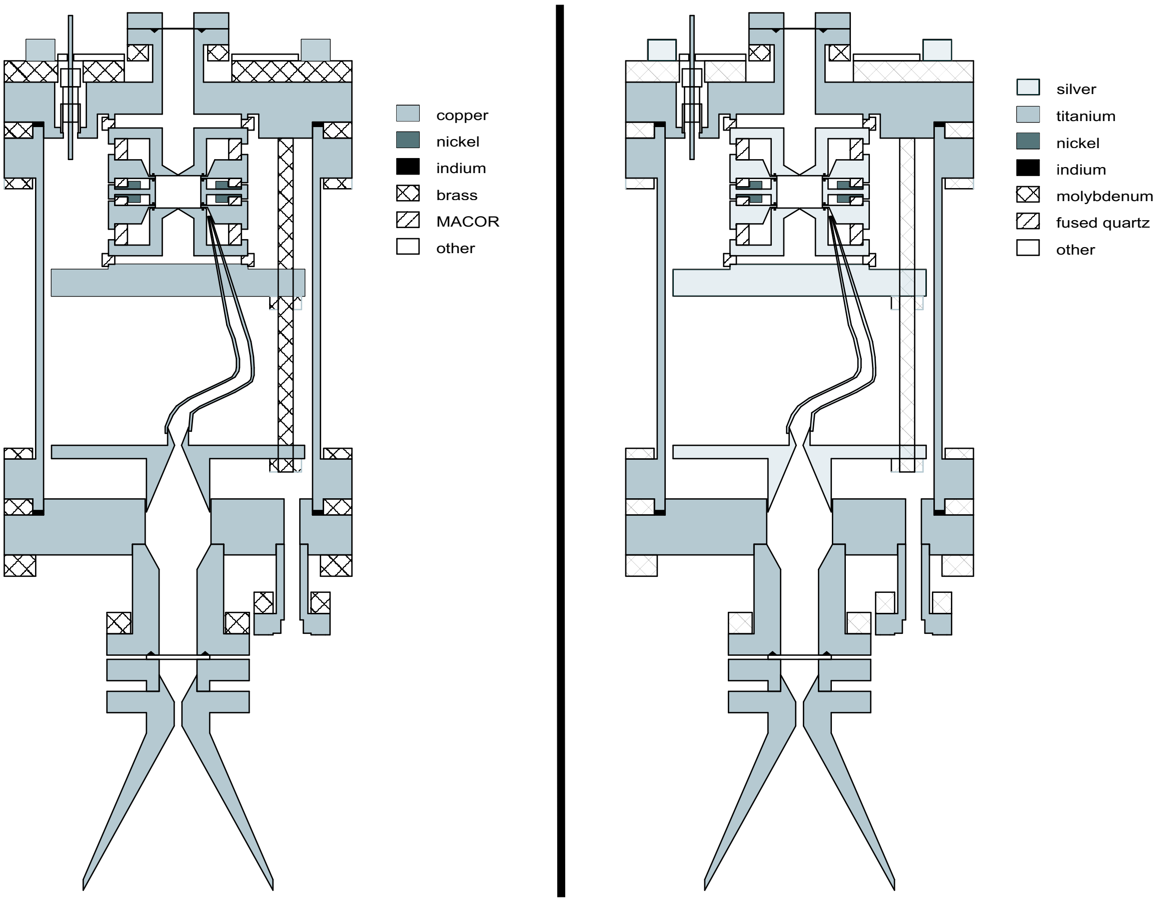

Figure 3.4: Copper and silver traps and vacuum enclosures

In order to obtain the narrow cyclotron and anomaly line widths afforded by the dilution refrigerator, the cryogenic FET amplifiers must be shut off while exciting these motions, as discussed in Ch. 4. The first-stage amplifier FET typically is set to dissipate about 10 μW and is heat-sunk to a post well-coupled to the mixing chamber. The 10 μW power dissipation causes a $\sim$ 10 mK change in the equilibrium temperature at the mixing chamber, which resulted in a $\sim$ 100 ppb shift in the B-field at the trap center. Such a field instability is far too large a shift for the sub-ppb measurement of ν_c required for sub-ppt g value measurements. Another source of power dissipation is the anomaly drive. As discussed in Ch. 4, anomaly transitions are driven by exciting the axial motion far off resonance, requiring a drive voltage that caused substantial heating in the sub-Kelvin environment.

Investigation of the dependence of the magnetic field shift as a function of temperature revealed the inverse-temperature dependence characteristic of paramagnetism, as shown in Fig. 3.5. Table 3.2 lists the magnitude of the nuclear paramagnetic contributions of various parts of the copper trap apparatus. The contribution of an element to the temperature dependence of B at the trap center depends on its geometry. (For example, the contribution of the same magnetic dipole can be either positive or negative, depending on its location relative to the trap center.)

The predicted coefficient for the nuclear Curie-law paramagnetism of 60 ppb / K^{-1} for the entire trap structure agrees reasonably well with the measured value of 40 ppb / K^{-1}. The contributions of the different trap electrodes lead to a substantial degree of mutual cancelation, so uneven heating of trap electrodes is a very good candidate for the discrepancy. Impurities in the copper electrodes is another candidate for the discrepancy between the predicted and observed temperature dependence.

One approach to dealing with the extreme B-field sensitivity to temperature is to carefully regulate the trap temperature and various heat flows. Toward this end, a radiofrequency drive matching the anomaly drive strength must always be applied, and a dummy heater matching the first-stage FET power must be turned on whenever the FET is turned off. Cyclotron line shapes in the copper trap at 100 mK were successfully measured using this technique.

description:	material	$\Delta B/B$ (ppb/K^{-1})
ring electrode	Cu	-89.0
compensation electrodes (2)	Cu	-7.8
endcap electrodes (2)	Cu	146.2
all trap electrodes	Cu	49.5
trap spacers	MACOR	-2.3
vacuum enclosure	Cu	12.1
total		64

Table 3.2: Nuclear paramagnetism of portions of the copper trap apparatus labeled in Fig. 3.4. At 100 mK, a 1 ppb/K^{-1} contribution causes a 0.1 ppb shift in the magnetic field at the trap center for a 1 mK temperature change.

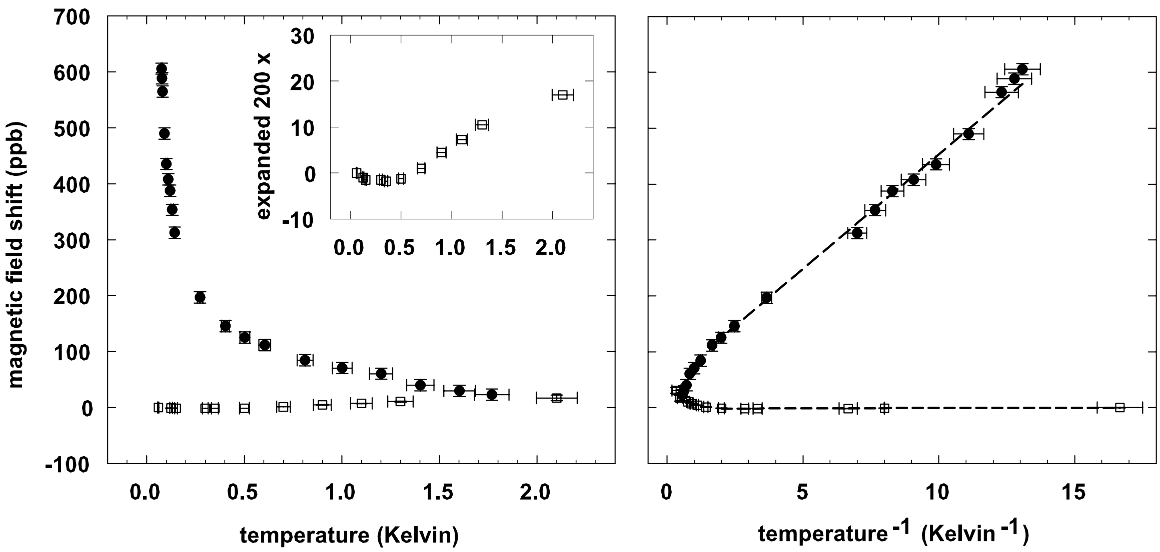

Figure 3.5: Temperature dependence of the magnetic field at the trap center in the copper trap (filled circles) and the silver trap (open squares). Fits to the data show 40 ppb / K^{-1} for the copper trap and 0.1 ppb / K^{-1} for the silver trap.

However, it was desired to further narrow the cyclotron and anomaly line widths by either increasing the axial frequency or by reducing the magnetic bottle (see Ch.

4). It was not clear that attempts to regulate the temperature and heat flows could be made sufficiently precise for line widths an order of magnitude narrower. Thus, the entire trap apparatus was rebuilt from materials with smaller nuclear paramagnetism, as discussed in Sec. 3.3.2.

3.3.2 Silver Trap

An entirely new trap and support structure was constructed from materials with low nuclear curie constants. Silver was used for the electrode material, and ground quartz was used for the insulating spacers between electrodes. The vacuum enclosure was made of titanium. To avoid cold welds when the titanium bolts were tightened to make indium seals, the pieces with threaded holes were made from molybdenum. Contributions to the overall paramagnetism of the most significant pieces is shown in Table 3.3.

The performance of the silver trap, which was quite satisfactory, is shown in Fig. 3.5. Of primary concern for a g value measurement is the stability of the B-field against short-timescale temperature changes, such as when the FET is shut off. Long-timescale temperature changes are not as important, since the trap temperature can be regulated on timescales longer than tens of minutes. Thus, temperature steps used to take the data for Fig. 3.5 were made as quickly as possible ($\sim$ 5 minutes per temperature step).

Current through the heater resistor, located on one side of the mixing chamber, was changed while the temperature was monitored on the other side of the mixing chamber. The mixing chamber heater was used for these tests rather than a heater

description:	material	$\Delta B/B$ (ppb/K^{-1})
ring electrode	Ag	-0.32
compensation electrodes (2)	Ag	-0.03
endcap electrodes (2)	Ag	0.55
all trap electrodes	Ag	0.20
trap spacers	Fused Quartz	0.01
vacuum enclosure	Ti	2.2
cancelation ring	Mo	-1.1

Table 3.3: Nuclear paramagnetism of the most significant elements of the silver trap apparatus. At 100 mK, a 1 ppb/K^{-1} contribution causes a 0.1 ppb shift in B at the trap center for a 1 mK temperature change.

closer to the trap in an attempt to evenly heat the entire trap apparatus. When the temperature of the mixing chamber was changed in this way, fast magnetic field shifts (timescales $\leq$ 2 minutes), followed by plateaus were observed. These fast shifts of B with temperature were clearly observable and were considered to be the quantities of interest, as discussed above. Any residual drift on longer time scales, if present, was relatively small and was ignored.

The observed temperature dependence of B at the lowest temperatures is approximately an order of magnitude less than expected for contributions of all materials in the area of the trap. It is consistent with heating of only the trap electrodes, but since the source of heat used for the tests was located at the mixing chamber, there is no reason to expect the electrodes to respond to the heater faster than much of the rest of the apparatus. The disagreement between the predicted and calculated temperature dependence of the silver trap apparatus was originally considered to be due to the success of the Mo cancelation ring, but is now considered to be fortuitous but not understood.

Chapter 4

Measurement of Cyclotron and Anomaly Frequencies

The basic ingredients of a g value experiment are the measurements of the cyclotron and anomaly frequencies. In this work we present the first fully quantum measurement of the electron g value. Although previous g value experiments [2, 3] measured the anomaly frequency by observing quantized spin flips, classical cyclotron spectroscopy was used. Quantum cyclotron spectroscopy eliminates systematic uncertainty associated with relativistic mass corrections of excited states, as discussed in Sec. 6.2.1. This work also represents the first sub-Kelvin g value measurement. Besides allowing quantum spectroscopy by cooling the cyclotron oscillator to its ground state, a reduced axial temperature narrows the cyclotron and anomaly line shapes, allowing a more precise measurement of the g value.

4.1 Cyclotron and Anomaly Transitions in a Penning Trap

As discussed in Sec. 6.1, a g value measurement is performed by measuring the ratio of anomaly to cyclotron frequencies, ω_a/ω_c. The quantum level diagram for these transitions is shown in Fig. 4.1.

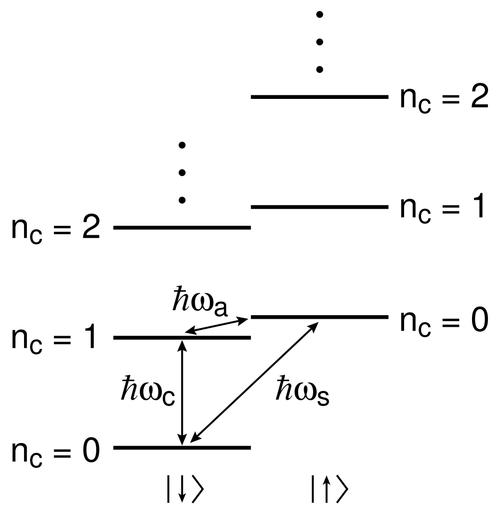

Figure 4.1: Diagram of spin and cyclotron quantized energies of an electron in a magnetic field. The effects of special relativity and of the electrostatic trapping potential are not included here. For $B = 5.5$ T and $\nu_s \approx \nu_c = \omega_c/(2\pi) \approx 150$ GHz, $\nu_a = \omega_a/(2\pi) \approx 170$ MHz.

As discussed in Sec. 4.5, all spectroscopy in the Harvard g value experiment is performed by constructing histograms of the success rate of driving one pure quantum state to another versus drive frequency. Cyclotron spectroscopy is performed by attempting to drive $|s=\uparrow, n_c = 0\rangle \rightarrow |s=\uparrow, n_c = 1\rangle$. Anomaly spectroscopy is performed by attempting to drive $|s=\uparrow, n_c = 0\rangle \rightarrow |s=\downarrow, n_c = 1\rangle$.

4.2 Theoretical Cyclotron and Anomaly Line Shapes

A semiclassical theory of the cyclotron and anomaly line shapes is presented by Brown [83], and a fully quantum theory is presented by D'Urso [70]. The discussion in this section only considers the line shape for transitions between two states of well-defined spin and cyclotron quantum numbers.

4.2.1 Magnetic Bottle Broadening

As discussed in Sec. 2.3.7, in order to allow detection of cyclotron and spin transitions, a small so-called magnetic bottle ΔB is imposed upon the homogeneous trapping field $\vec{B} = B\hat{z}$. The $\hat{z}$ component of the leading-order non-uniform term of this field, called the "magnetic bottle", is given by

$$\Delta B = B_2 \left(z^2 - \frac{\rho^2}{2} \right). \tag{4.1}$$

While the magnetic bottle has the beneficial effect of allowing detection of cyclotron transitions via shifts in the axial frequency (see Sec. 2.3.7), it also produces an undesirable inhomogeneous broadening of the cyclotron and anomaly line shapes. This broadening occurs because, in the presence of the bottle, the average magnetic field sampled by the on-axis ($\rho = 0$) electron is given by

$$\langle B_{total} \rangle = B + B_2 \left\langle z^2 \right\rangle = B + \frac{2B_2 E_z}{m\omega_z^2}, \tag{4.2}$$

where E_z is the axial energy. Thus, the magnetic field seen by the electron depends on its axial excitation.

4.2.2 Line Shapes

The theory governing line shape broadening is the same for both cyclotron and anomaly resonances, but the resonances acquire different shapes due to their different frequencies. The parameter which determines the shape of the broadened resonance is $\gamma_z/\Delta\omega$, where $\gamma_z/(2\pi)$ is the axial damping width. The thermal shift parameter $\Delta\omega$ is equal to the frequency offset of the weighted center of the line shape from the resonance frequency ω^0 of an electron at rest at $z = 0$. For a thermal distribution of axial states at temperature T_z, $\Delta\omega$ is given by

$$\Delta\omega = \omega^0 \frac{B_2}{B} \frac{k_B T_z}{m\omega_z^2}. \tag{4.3}$$

The theoretical curves for various values of $\gamma_z/\Delta\omega$ are shown in Fig. 4.2. Because of the frequency-time uncertainty principle, $1/\Delta\omega$ sets the scale for the observation time required to distinguish one frequency on the resonance from another. If $\gamma_z << \Delta\omega$, thermal fluctuations of the axial energy (and therefore of the magnetic field) are slow compared with the required observation time. In this case (the "exponential limit"), the resulting line shape vanishes below ω^0 and is a decaying exponential of width $\Delta\omega$ above ω^0. This distribution reflects the Boltzmann distribution of axial energies. In the "Lorentzian limit" where $\gamma_z >> \Delta\omega$, the magnetic field fluctuates rapidly compared with the time required by the uncertainty principle to observe one frequency on the resonance; the resulting line shape is a narrow Lorentzian, offset from ω^0 by $\Delta\omega$. The weighted center of a line shape in one of these limits, or anywhere in between, is at $\omega = \omega_0 + \Delta\omega$, regardless of the lineshape parameter $\gamma_z/\Delta\omega$. The

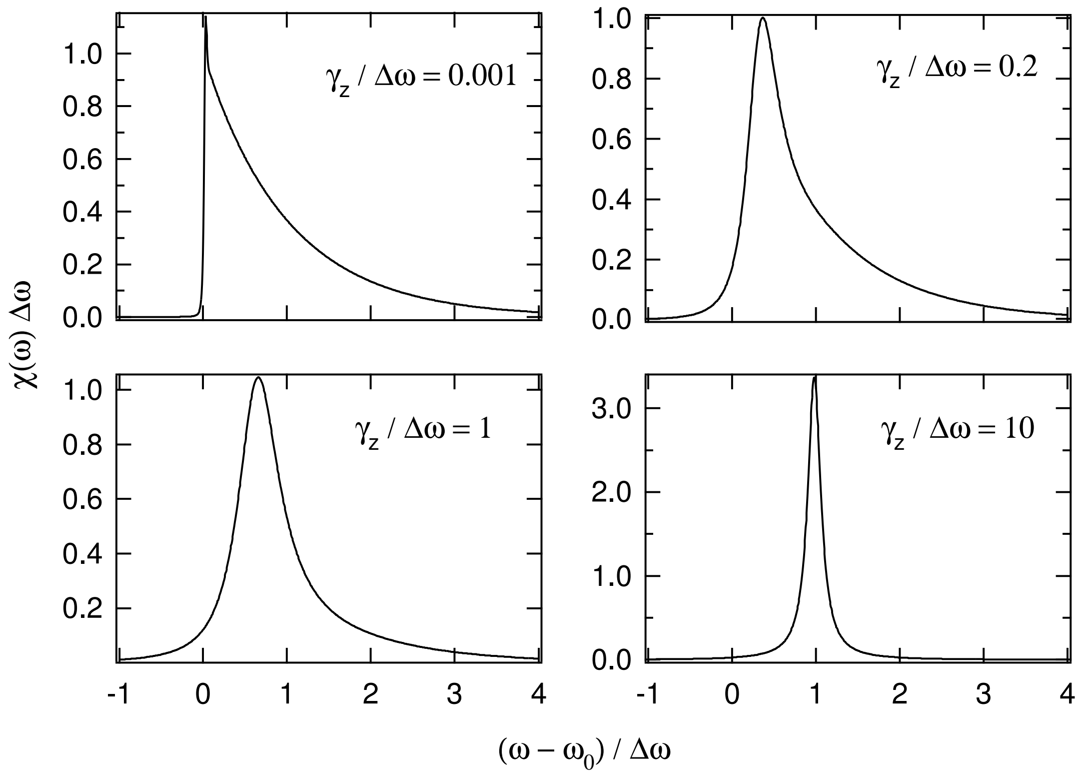

Figure 4.2: Cyclotron or anomaly line shapes at various values of the lineshape parameter $\gamma_z/\Delta\omega$. The "exponential limit" is obtained at the smaller values shown for this parameter, and the "Lorentzian limit" is obtained at the larger values.

expression for the theoretical line shapes [84] is

$$\chi(\omega) = \frac{4}{\pi} Re \frac{\gamma' \gamma_z}{(\gamma' + \gamma_z)^2} \sum_{n=0}^{\infty} \frac{(\gamma' - \gamma_z)^{2n} (\gamma' + \gamma_z)^{-2n}}{(n + \frac{1}{2})\gamma' - \frac{1}{2}\gamma_z - i(\omega - \omega_0)}, \tag{4.4}$$

(Note: the equation given by Brown and Gabrielse in the commonly used Ref. [69] has one term with a sign error). For the present experiment, the cyclotron resonance approaches the exponential limit, and the anomaly resonance approaches the Lorentzian limit, as shown in Figure 4.3.

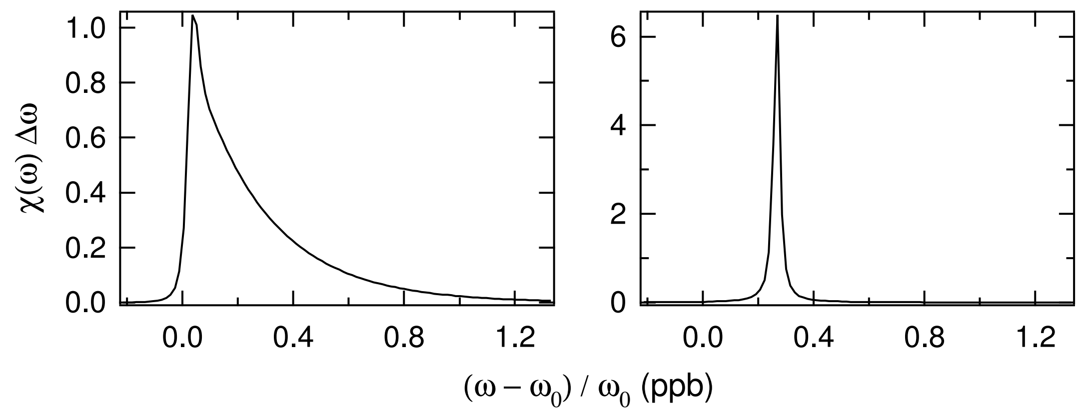

Figure 4.3: Theoretical cyclotron and anomaly line shapes for B_2 = 1500 T/m^2, γ_z = (2π) 1 Hz, T_z = 100 mK, ν_z = 200 MHz, ω_c = 149 GHz, ω_a = 173 MHz.

4.2.3 Frequency-Time Broadening

Owing to the high frequency of the cyclotron motion, frequency-time broadening from the finite cyclotron lifetime is negligible compared to the magnetic bottle broadening. However, the frequency-time uncertainty principle does modify the anomaly line shapes from those discussed in Sec. 4.2.2.

Anomaly spectroscopy is performed between $|s = \downarrow, n_c = 1\rangle$ and $|s = \uparrow, n_c = 0\rangle$. The finite lifetime of the $|s = \downarrow, n_c = 1\rangle$ state causes its energy to be broadened, resulting in a broadening of the frequency according to $\Delta\omega\,\Delta t \approx 1$. Much of the work reported here was performed at $\nu_c = 146.8$ GHz, where the measured cyclotron lifetime was 1.4 s (see Sec. 5.3). The resulting frequency-time broadening, $\Delta\nu \approx 0.1$ Hz ≈ 0.5 ppb, contributes substantially to the anomaly line shapes reported in Sec. 4.5.2 for this B-field. At 149.0 GHz, where the cavity modes are well decoupled from the cyclotron oscillator, $\tau = 6.7s$, and the line width is dominated by other non-ideal sources of broadening (see Sec. 4.6.1).

4.3 Axial Temperature

Although measurement of the axial frequency plays only a secondary role in measurement of the magnetic moment of the electron, as described in Sec. 4.2, the inhomogeneous broadening of the cyclotron and anomaly line shapes is directly proportional to the axial temperature. Thus, obtaining a low axial temperature plays a central role in improving the precision of g value measurements.

4.3.1 Measurement of the Axial Temperature

Owing to the presence of the magnetic bottle, a finite axial temperature T_z gives rise to a range of magnetic fields sampled by the electron. The result for the cyclotron and anomaly resonances is an inhomogeneous broadening $\Delta\omega$ proportional to T_z, described by Eq. 4.3.

Since the axial oscillator is strongly coupled to the tuned circuit, which includes the FET amplifier input (see Sec. 2.3.2), the temperature of the electrons in the channel of the transistor contributes to the trapped electron's axial temperature. To obtain a low axial temperature and the resulting narrow cyclotron and anomaly line widths, the amplifier is typically turned off while the cyclotron or anomaly excitations are applied.

The inhomogeneous broadening of the cyclotron line shape is used to measure the axial temperature T_z via Eq. 4.3. Other broadening mechanisms currently dominate the anomaly line width. So, the only observable effect of T_z on the anomaly line shape is to shift its center, and no information about T_z can be obtained from this resonance.

4.3.2 Achieving a Cold Axial Temperature

In the first experiments on a single electron in a dilution refrigerator environment [85, 53], it was found that T_z was 16 Kelvin when the HFET (Harvard Field Effect Transistor) [53] amplifier was left on during cyclotron excitation. When the HFET was turned off during cyclotron excitation, the failure to observe driven cyclotron excitations at the expected frequency led to speculation that the electron had cooled and the line shape was narrower than the drive frequency step. Equipment malfunctions prevented further investigation for some time.

Subsequent work at 1.6 Kelvin showed that, with the HEMT (High Electron Mobility Transistor) amplifier either on or off, the axial temperature T_z of the electron was consistently 16 Kelvin. In later experiments, a thermometer mounted on the amplifier circuit board registered a temperature of 4 K with the amplifier on. The time constant for heat to leave the circuit board after the FET was turned off was on the order of 20 minutes. The conclusion was that the amplifier was not well enough heat-sunk to the refrigerator, and its internal temperature was well above ambient. It is likely that in the original dilution refrigerator experiments, the inability to find a broad cyclotron resonance when the HFET was turned off [53], was actually due to a large magnetic field shift associated with nuclear paramagnetism of the copper trap (see Ch. 3).

In order to better heat sink the amplifier, the trap support structure was changed. The original structure was a single rod of annealed OFHC copper with many mounting holes drilled through it. This structure was replaced by an annealed OFHC tripod with square cross-sectioned legs. The new support structure provided better struc-

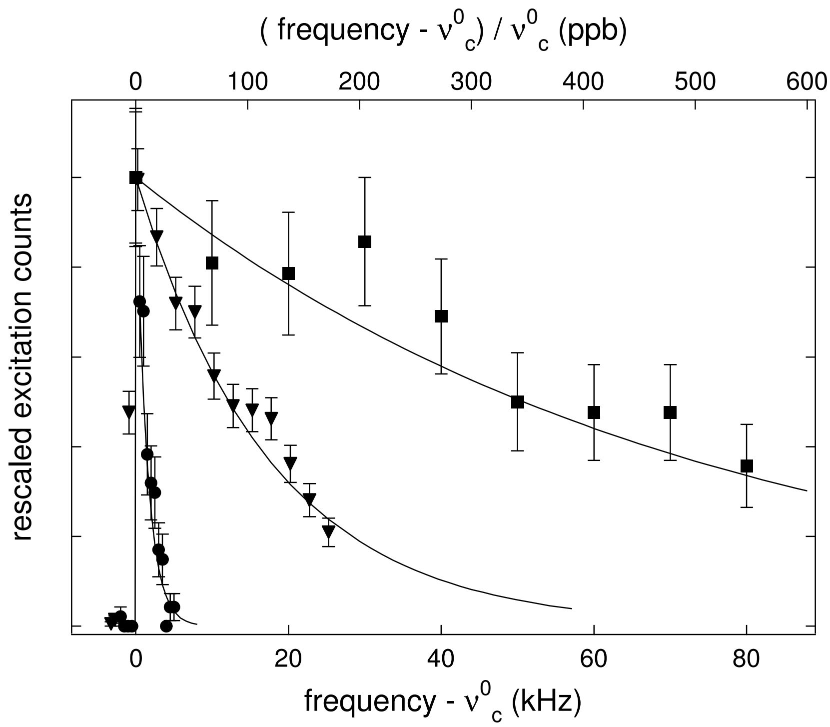

Figure 4.4: Cyclotron line shapes (with $\nu_z = 64$ MHz) for the HFET amplifier off during excitation (squares), HEMT 1st- and 2nd-stage amplifiers on during excitation (triangles), and HEMT 1st- and 2nd-stage amplifiers off during excitation (circles). The best fits yield 16 K, 3.7 K, and 0.32 K respectively.

tural stability (important for positioning the trap center reliably at the B-field center) and a flat surface well-connected to the mixing chamber for heat-sinking the FET.

To provide better heat-sinking, the amplifiers were rebuilt [70]. The new HEMT amplifier had a drain soldered directly to a copper plate, which was bolted to the tripod leg. Previously, the FET drain had been electrically floating. In order to avoid creating voltage offsets at the trap associated with return current from the FET, a floating power supply was used to supply the drain voltage. Also, a second-stage amplifier was added at the still to increase the cryogenic gain and to improve isolation of noise travelling down the drain coax from room temperature.

With the improved heat sinking, the axial temperature was measured to be an improved temperature of 3.7 K if both the first- and second-stage amplifiers were left on during cyclotron excitation. For these tests, the mixing chamber was held at 100 mK. Turning off the first-stage amplifier achieved an axial temperature of 600 mK. Turning off both amplifiers during the cyclotron excitation yielded $T_z = 320$ mK. The benefit of turning off the second-stage amplifier is most likely due to reducing its reverse conductance, which reduces the transmission of noise from the later stages [70].

The cyclotron resonances corresponding to these improvements are shown in Fig. 4.4. The sustained elevation of the electron temperature above the 100 mK of the environment is most likely due to heating from a noise drive [70].

4.4 Choice of Axial Frequency

This work was begun at $\nu_z = 60$ MHz, but it was realized [70] that there were two independent advantages of working at a higher axial frequency. Less anomaly drive power would be needed to create spin-flip transitions at a reasonable rate, and the thermal shift parameter $\Delta\omega$ would be reduced without a proportional reduction in the signal from a single quantum jump.

4.4.1 Axial Frequency and Anomaly Drive Strength

Anomaly transitions are created by driving the electron axially far off of its resonance frequency [53]. Far off resonance, the response function χ_a scales linearly with detuning, so driving the 170 MHz anomaly transition requires a factor of ~ 3 less drive power if the axial frequency is changed from 60 MHz to 200 MHz. A weaker anomaly drive causes less heating of the sub-Kelvin environment. Power dissipation is potentially a problem, because variations in temperature can cause magnetic field shifts associated with nuclear paramagnetism of material near the trap, as discussed in Ch. 3.

As discussed in Ch. 6, there are several sources of systematic error in a g value measurement associated with anomaly drive strength. The most significant of these errors are associated with the induced motion of the electron [86]. However, it can be shown that the weaker drive power afforded by $\nu_z = 200$ MHz does not help in this case, since the electron is still driven to the same amplitude to obtain a given anomaly transition rate.

4.4.2 Axial Frequency and Thermal Broadening

In order to improve the precision of g value experiments, it is desirable to make the thermal shift parameter $\Delta\omega$ of Eq. (4.3) as small as possible while maintaining the ability to resolve single-quantum cyclotron jumps (see Sec. 2.3.7). Above we have discussed the cooling of T_z toward this end. Since $\Delta\omega \propto B_2/\nu_z^2$, we can also consider using a smaller magnetic bottle or a larger axial frequency to reduce the inhomogeneous broadening of ν_c and ν_a. Eq. (2.12) shows that $\delta \propto B_2/\nu_z$, where δ is the axial frequency shift due to a single-quantum cyclotron jump. The thermal shift parameter and the jump size both decrease in the same way if B_2 is reduced. However, if ν_z is increased, $\Delta\omega$ shrinks faster than does δ. For the case of $\nu_z =$

65 MHz → 200 MHz without changing B_2, we get

$$\frac{\delta_{200}}{\delta_{65}} = \frac{1}{3}$$
$$\frac{\Delta\omega_{200}}{\Delta\omega_{65}} = \frac{1}{9}\,. \tag{4.5}$$

So reducing the thermal broadening of the cyclotron and anomaly line shapes is better accomplished by increasing the axial frequency than by reducing the magnetic bottle. This is true provided that axial frequency shifts of the same size can still be detected at the higher frequency, an issue discussed in Sec. 4.4.3.

4.4.3 Axial Frequency and Quantum Jump Resolution

As discussed in Sec. 4.4.2, to reduce the thermal shift parameter $\Delta\omega$, the ratio B_2/ν_z should be made as small as possible while maintaining the ability to resolve single-quantum cyclotron transitions. It was also shown that it is preferable to accomplish this by increasing ν_z rather than by decreasing B_2. However, it is not obvious, *a priori*, what effect the choice of ν_z has on quantum jump resolution.

In order to resolve a quantum jump in a given averaging time, the signal-to-noise ratio S/N of the axial signal must be larger than some value. Assuming the noise is thermal, the voltage noise N has no frequency dependence. The magnitude of the voltage signal S is proportional to the tuned circuit on-resonance resistance R (see Sec. 2.3.2) and to the current I that the driven electron sends through R:

$$\frac{S}{N} \propto IR. \tag{4.6}$$

If z is the instantaneous position of the electron, $I \propto \frac{dz}{dt} \propto \omega_z$. Using of $Q = R\omega_z C$ and assuming that C will not depend strongly on frequency, we can rewrite Eq. (4.6) as

$$\frac{S}{N} \propto Q. \tag{4.7}$$

So for any axial frequency, we expect that the ability to resolve quantum jumps of a given size is proportional to the amplifier Q value.

Next, we will consider how Q is expected to behave with frequency. Q can be expressed as

$$Q = \frac{1}{r\omega_z C}\,, \tag{4.8}$$

where r is the tuned circuit loss represented as a series resistance. For optimal detection [77], the amplifier is designed such that the physical resistance r is primarily due to loss in the tuned circuit, rather than to loss in the FET channel. Since we expect that both the inductance and resistance will be proportional to the inductor length,

$$r \propto L \propto \frac{1}{\omega_z^2}\,, \tag{4.9}$$

where we have again assumed that C will not vary strongly with frequency. Thus, Eq. 4.8 becomes

$$Q \propto \omega_z. \tag{4.10}$$

Although many approximations were made to arrive at Eq. (4.10), when considered along with Eq. (4.7) and the other advantages of a higher axial frequency discussed above, it was decided to design and build a 200 MHz amplifier [70].

The actual 200 MHz amplifier which was constructed has $Q \approx 600$ [70], similar to the Q of the 60 MHz amplifier. So, the quantum jump resolution did not improve by increasing ν_z, but the motivating benefits discussed in Sec. 4.4.1 and 4.4.2 were achieved.

4.5 Single Quantum Spectroscopy

As discussed in Sec. 6.2.1, the presence of relativistic effects makes it advantageous to perform cyclotron spectroscopy between known pure quantum states. The enhanced cyclotron lifetime obtained by tuning the magnetic field well away from the nearest electromagnetic cavity mode (see Sec. 5.3), makes single quantum cyclotron spectroscopy possible while still using a relatively small magnetic bottle (see Sec. 2.3.7).

As shown in Fig. 6.2, there is no relativistic shift of the anomaly frequency. However, reduced lifetimes of excited cyclotron states would broaden the anomaly line shape, so it is desirable to perform anomaly spectroscopy between the lowest possible quantum states: $|s=\downarrow, n_c=1\rangle$ and $|s=\uparrow, n_c=0\rangle$.

Each time a cyclotron excitation is attempted, an off-resonant anomaly pulse is also applied, and vice versa. This procedure is used so that any affect that either of these drives has on the axial or magnetron state distribution occurs while both line shapes are being studied; any effects will tend to cancel out in a g value measurement.

4.5.1 Cyclotron Spectroscopy

In the work presented here, cyclotron spectroscopy is performed between the quantum states $|s=\uparrow, n_c=0\rangle$ and $|s=\uparrow, n_c=1\rangle$. The following steps are used to attempt to drive a cyclotron excitation:

1. Check that the electron is in the $|s=\uparrow, n_c=0\rangle$ state

2. Turn on a strong resonant magnetron cooling drive (see Sec 2.3.6); wait t_1 sec-

onds

3. Shut off the axial drive; wait t_2 seconds

4. Shut off the fist- and second-stage amplifiers; wait t_3 seconds

5. Shut off the magnetron cooling drive; wait t_4 seconds

6. Pulse the on-resonance cyclotron drive along with an off-resonance anomaly drive for t_5 seconds

7. Turn on the amplifiers and axial drive; wait t_6 seconds

8. Check for transition to $|s=\uparrow, n_c=1\rangle$

Examples of observed cyclotron excitations are shown in Fig. 2.14. The cyclotron line shape is constructed by building a histogram of successful excitations to $|s=\uparrow, n_c=1\rangle$ versus microwave drive frequency.

4.5.2 Anomaly Spectroscopy

Anomaly spectroscopy is performed between the $|s=\uparrow, n_c=0\rangle$ and $|s=\downarrow, n_c=1\rangle$ quantum states. The following steps are used to attempt an anomaly excitation:

1. Check that the electron is in the $|s=\uparrow, n_c=0\rangle$ state

2. Turn on a strong resonant magnetron cooling drive; wait t_1 seconds

3. Shut off the axial drive; wait t_2 seconds

4. Shut off the fist- and second-stage amplifiers; wait t_3 seconds

5. Shut off the magnetron cooling drive; wait t_4 seconds

6. Pulse the on-resonance anomaly drive along with an off-resonance cyclotron drive for t_5 seconds

7. Turn on the amplifiers and axial drive; wait t_6 seconds

8. Check for transition to $|s=\downarrow, n_c=0\rangle$; continue checking for t_7 seconds to allow for slow cyclotron decay from $|s=\downarrow, n_c=1\rangle$

9. If a transition to $|s=\downarrow, n_c=0\rangle$ was observed, reset the electron in $|s=\uparrow, n_c=0\rangle$ by successive cyclotron and anomaly drive pulses

An example of an observed spin transition is shown in Fig. 2.15. The anomaly line shape is constructed by building a histogram of successful spin flips versus anomaly drive frequency.

4.5.3 Choice of Quantum States for Spectroscopy

Cyclotron spectroscopy could be performed equally well between $|n_c=0\rangle$ and $|n_c=1\rangle$, in either the $|s=\downarrow\rangle$ or $|s=\uparrow\rangle$ ladder. However, as discussed in Sec. 6.2.1, the appropriate relativistic g value correction differs by 1.2 ppt, depending on spin state. So it is necessary to know which spin state was used for cyclotron spectroscopy. As outlined in Sec. 4.5.1 all cyclotron spectroscopy for g value measurements is performed between $|s=\uparrow, n_c=0\rangle$ and $|s=\uparrow, n_c=1\rangle$.

Anomaly spectroscopy is performed between $|s=\uparrow, n_c=0\rangle$ and $|s=\downarrow, n_c=1\rangle$. As discussed in 4.2.3, the frequency-time uncertainty principle sets the natural line width of the anomaly transition. This line width is the same regardless of whether

$|s=\downarrow, n_c=1\rangle$ or $|s=\uparrow, n_c=0\rangle$ is chosen as the initial state. However, there are also effects of the finite cyclotron lifetime which depend on the choice of initial spin state. If the electron begins in state $|s=\downarrow, n_c=1\rangle$ there is a probability $p_c\,dt$ that the electron will spontaneously decay to $|s=\downarrow, n_c=0\rangle$ in a time interval dt. If we apply an anomaly drive, and the the electron is still in $|s=\downarrow, n_c=1\rangle$, there is a probability $p_a\,dt$ that the electron will transition to $|s=\uparrow, n_c=0\rangle$ in a time dt. Thus the probability dP that, under the influence of a weak anomaly drive, the electron will transition to $|s=\uparrow, n_c=0\rangle$ between a time t and $t+dt$ is given by

$$dP = (p_a\,dt)(1 - \int_0^t p_c\,d\tau) \tag{4.11}$$

If the weak anomaly drive is applied for a time T, then the probability P that the electron will transition to $|s=\uparrow, n_c=0\rangle$ is given by

$$\begin{aligned} P = \int_0^T dP &= p_a T - \int_0^T dt\,p_a \int_0^t p_c\,d\tau \\ &= p_a T\left(1 - \frac{p_c T}{2}\right) \end{aligned} \tag{4.12}$$

So, in the case of a weak anomaly drive and the initial state $|s=\downarrow\rangle$, the transition probability is linear in drive strength but non-linear in time. The time non-linearity is absent if the initial state is $|s=\uparrow\rangle$.

It is not immediately obvious whether the time non-linearity of Eq. (4.12) creates distortions in the line shape function $\chi_a(\omega)$. For this reason, anomaly spectroscopy in this work is always performed by attempting to drive from $|s=\uparrow, n_c=0\rangle \rightarrow |s=\downarrow, n_c=1\rangle$. The disadvantage of this choice is that several cyclotron lifetimes τ_c must pass before a failure to drive the anomaly transition can be confirmed. Since building a non-saturated histogram involves far more failures to drive a transition than successes, there is a significant overhead for the choice of initial spin state $|s=\uparrow\rangle$. With an inhibited cyclotron lifetime of ~ 7 s, as at 149.0 GHz for the current trap (see Sec. 5.3), the overhead in wait time noticeably degraded the statistics in overnight scans.

In contrast, if anomaly spectroscopy were performed by driving the transition $|s=\downarrow, n_c=1\rangle \rightarrow |s=\uparrow, n_c=0\rangle$, one would only have to wait an average of τ_c (rather than a fixed value of several τ_c) to confirm a failed anomaly transition. If it were determined that the effects of performing anomaly spectroscopy from the initial state $|s=\downarrow, n_c=1\rangle$ were well-understood and acceptable, the quality of histograms for overnight scans could be greatly improved.

4.5.4 Data Collection

As discussed in Ch. 3, it was generally not possible to take g value data during daytime hours. This limited most scan lengths to 10 to 15 hours. At several (typically three or four) intervals over the course of a g value measurement, cyclotron edge-tracking was performed (see Sec. 3.1). These intervals provided information about changes in the magnetic field so that data over the course of a night could be normalized against field drift. Fig. 4.5 shows normalization for a cyclotron scan during a period when the field drift was quite large (see Sec. 3.2.4).

Between edge-tracking intervals, anomaly and cyclotron scans are alternated. One attempted excitation is made at each cyclotron frequency, and then one attempted anomaly transition is performed at each anomaly frequency, etc. During periods of large field drift, the frequencies for excitation attempts are shifted from one scan to

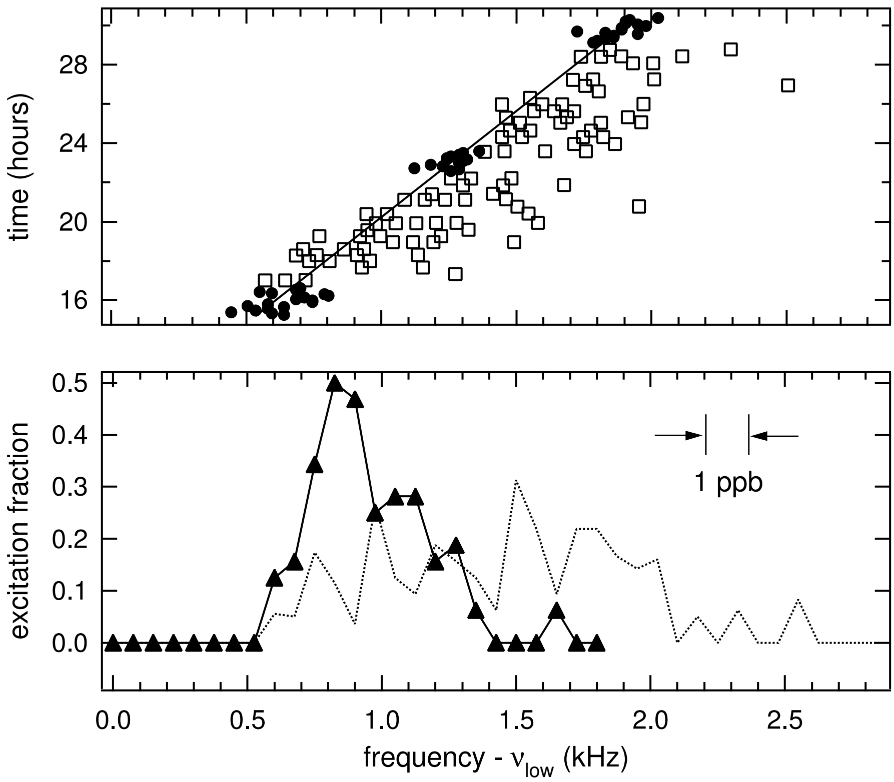

Figure 4.5: Correcting a cyclotron line shape for field drift of $\sim$ 0.6 ppb per hour. Upper: edge-tracking points (closed circles) with fit (line) and uncorrected cyclotron excitation events (open squares). Lower: uncorrected histogram (dotted line) and histogram corrected for drift (triangles).

the next in a manner projected to follow the field drift. Spans are made wide enough so that only an approximate prediction of the field drift for the night is needed. Each attempted excitation is recorded with a time stamp, and histograms normalized against field drift are later created for g value analysis, as shown in Fig. 4.5.

4.6 Extracting Frequencies from Resonance Histograms

One advantage of the Harvard g value measurement is that the cyclotron and anomaly line widths are substantially narrower than in previous experiments [2, 8]. Example line shapes are shown in Fig. 4.6. As a result of the narrow line shapes, a 1 ppt g value measurement can be performed with almost no line splitting and a very limited understanding of the resonance shapes. Such a measurement would already surpass previous measurements by a substantial factor. However, with minimal line splitting, the Harvard g value measurement can do even better.

Two line-splitting methods are used in this work. Conceptually, it is perhaps simplest to fit the cyclotron and anomaly line shapes to the theoretical curves and then extract the frequencies ν_c^0 and ν_a^0 corresponding to the resonances of an electron at 0 Kelvin. In practice, there are several complications with this procedure. An alternative to fitting the lines is to split the measured resonances statistically, by taking their weighted averages. The latter method is what is actually used for analysis of the Harvard g value data.

4.6.1 Line-Fit Method

Previous g value measurements [54] were performed by extracting from the measured cyclotron and anomaly resonances the frequencies ν_c^0 and ν_a^0, corresponding to the electron at rest in the center of the trap. (See Sec. 4.2.2 for a discussion of the theoretical line shapes.) Experimentally, this is achieved by determining ν_c^0 from the left edge of the cyclotron line shape and T_z from the width of the exponential tail. The value of T_z is then used to deduce the offset of ν_a^0 from the measured center frequency of the Lorentzian anomaly resonance.

Line-Fit Method Results

At $\nu_z = 60$ MHz, the Harvard line shapes showed good agreement with the expected line shapes of Sec. 4.2.2, as can be seen for the cyclotron line shapes in Fig. 4.4. However, as shown in Fig. 4.6, the 200 MHz cyclotron line shapes were found to have rounded low-frequency edges. Although the rounding width is less than the exponential tail width, the rounding still contributes substantially to the overall line shape. It is unknown whether the same rounding was present at $\nu_z = 60$ MHz since, due to complications with B-field stability present at that time, the edges of those line shapes (which are also an order of magnitude wider than the $\nu_z = 200$ MHz line shapes) were never examined with sufficient precision.

The origin of the rounding is unknown, although it is speculated that magnetic field jitter or mechanical vibrations might be responsible. Since the edge-tracking resolution (see in Sec. 3.1) performs less well than expected at 200 MHz, it is believed that the broadening mechanism occurs on time scales faster than ~ 10 minutes, so slow drifts seem to be ruled out.

For the purposes of line fitting, it seems reasonable to assign a Gaussian distribution to the broadening, since it is likely associated with a random process. Line fits are performed by first fitting the measured cyclotron histogram to a convolution of the ideal (near-exponential) line shape with a normalized Gaussian function. The

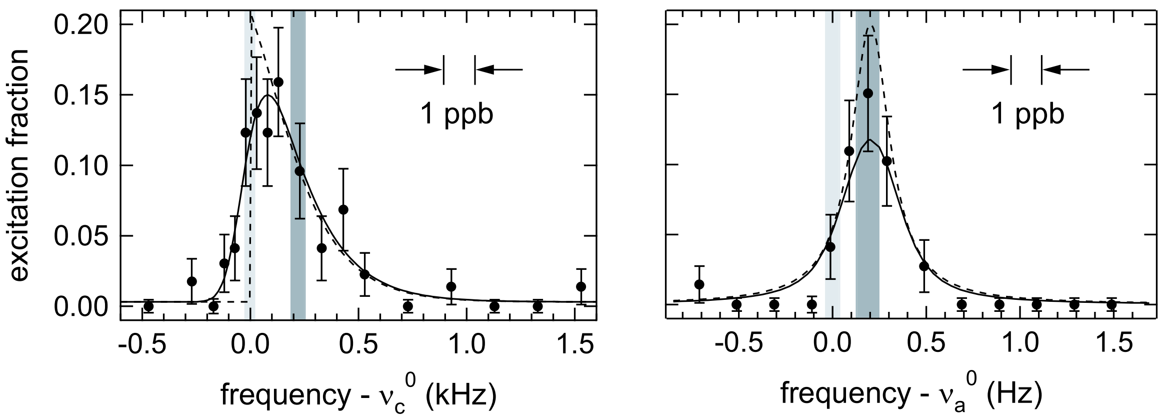

Figure 4.6: Measured cyclotron (left) and anomaly (right) line shapes with $\nu_z = 200$ MHz and $\nu_c = 146.8$ GHz. The data for both line shapes were collected over a period of about 10 hours. Solid lines represent the best fits including Gaussian broadening. Dashed lines show the predictions for the same fit parameters but with the Gaussian broadening parameter set to zero. The relatively short cyclotron lifetime τ_c at this field value causes substantial broadening of the anomaly resonance width. Light bars represent the 68% confidence interval for the ν_c^0 and ν_a^0 from the line-fit method. Dark bars represent the 68% confidence interval for the ν_c^* and ν_a^* from the line-center method.

three free parameters of this fit are the overall amplitude, the axial temperature, and the Gaussian broadening width. An estimate of the frequency ν_c^0 is thus extracted. The axial temperature and the Gaussian broadening are then used as input parameters for the anomaly fit. As discussed in Sec. 4.2.3, the measured cyclotron lifetime also needs to be included as a fit parameter for the anomaly line.

The results of the line-fitting method on a small data set are shown in Fig. 4.7. The data set used was actually part of a search for an anomaly systematic power shift. Later studies confirm that there is no observable power shift, so it is expected that all g value measurements in Fig. 4.7 should yield the same value. As far as can be judged from the limited data set in the figure, the line-fitting method behaves well; the estimated fit uncertainties and the observed scatter seem consistent.

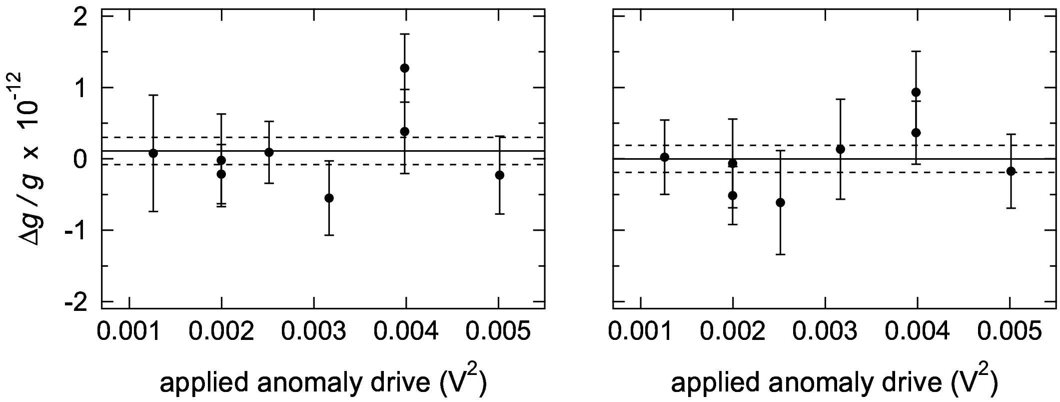

Figure 4.7: Demonstration of equivalence of the line-fitting method and the line-center method for determining the g value, using data from a search for an anomaly power shift at $\nu_c = 146.8$ GHz. g is calculated using the line fit-method (left) and line center-method (right). Solid lines indicate weighted averages and dashed lines indicate uncertainties in the weighted averages. An uncertainty $\Delta g/g \approx 1 \times 10^{-12}$, if due in equal parts to the uncertainties in the anomaly and cyclotron line fitting, would correspond to an error of $\Delta\nu/\nu \approx 0.7 \times 10^{-9}$ in the line shapes shown in Fig. 4.6.

Line-Fit Method Drawbacks

Further studies of the quality of fits were not performed because it was judged that the line-center method, discussed in Sec. 4.6.2, was a better way to extract frequencies from the measured histograms. There are several drawbacks of using the line-fitting method for a g value measurement which contribute to this conclusion.

First, the data of Figs. 4.6 and 4.7 were taken at $\nu_c = 146.8$ GHz. Here, the relatively poor decoupling from the nearby cavity mode, a situation which is unfavorable for a g value measurement, did not enhance the cyclotron lifetime by a large factor, allowing more sweeps to be taken in an overnight scan (see Sec. 4.5.3). At $\nu_c = 149.0$ GHz, where decoupling from cavity modes is much more favorable for a g value measurement, the longer cyclotron lifetime made the statistics of the collected histograms noticeably worse. Overnight scans at 149.0 GHz seldom yielded traces which could be fit with confidence.

A related drawback of the line-fitting method is that the effects of the thermal shift parameter $\Delta\omega$ and of the Gaussian rounding parameter are difficult to reliably separate. For the cyclotron line shapes, both of these parameters contribute to the overall line width. Therefore it is expected that a fitting algorithm will have some difficulty in accurately determining these fit parameters and their associated uncertainty. Since the axial temperature is used as an input parameter to the anomaly line fit, the possibility of introducing systematic shifts into g value measurements from poorly fit cyclotron line shapes seems substantial.

Even with line shapes without extra broadening and with good statistics, the line-fitting method is not ideal. In particular, one would like to avoid relying on the fit of the cyclotron line shape in order to calculate the required *offset* to apply to the anomaly line center. It would be much preferred to use the center of the anomaly line as a measurement of ν_a.

The line-center method of extracting ν_c and ν_a from measured histograms, discussed in Sec. 4.6.2, addresses all these concerns.

4.6.2 Line-Center Method

As discussed in Sec. 4.2.2, the presence of the magnetic bottle makes the resonance frequencies ν_c and ν_a dependent upon the axial energy. Thus, to determine the g value accurately, a measurement of the cyclotron and anomaly frequencies corresponding to the *same* axial energy must be obtained. Although in principle, as discussed in Sec. 4.6.1, the frequencies ν_c^0 and ν_a^0 corresponding to a vanishing axial energy can be extracted from the thermally shifted line shapes, in practice there are complications with this procedure. It was realized over the course of this work that the quantities ν_c^* and ν_a^*, corresponding to the resonance frequencies at the average axial energy, serve just as well for a g value measurement and are substantially easier to measure.

Averaging the Spectral Distribution

Sec. 4.2.2 discusses how the same distribution of axial energies can yield different line shapes, depending on the time constants involved. Here, we will use the generic term "magnetic oscillator" to represent either the cyclotron or anomaly oscillator. The magnetic oscillator has a range of frequencies, caused by the thermal distribution of the axial energies in the presence of the magnetic bottle. Essentially, the different line shapes arise depending on whether a coherent or an incoherent sampling of the magnetic oscillation is performed.

If the axial energy changes very slowly compared with the time required by the uncertainty principle to probe the magnetic line shape, then spectroscopy essentially performs an incoherent sum over the distribution of magnetic oscillator frequencies. In this case, the spectrum acquires an exponential shape because of the Boltzmann distribution of axial energies. If, on the other hand, the axial energy changes very quickly compared with the time required to probe the resonance, a coherent sum over the magnetic oscillation is performed. In this case, the phases over the range of oscillation frequencies cancel on average except at the central value, producing a narrow Lorentzian line shape.

As can be seen in Fig. 4.2, the average value of the resulting spectrum always corresponds to the average axial energy. Coherent summing, incoherent summing, or an arbitrary combination of the two always produces a spectrum which preserves the mean oscillation frequency. Thus, the frequencies ν_c^* and ν_a^* can be obtained simply by taking the weighted mean of the measured cyclotron and anomaly histograms.

Line-Center Method Advantages

As explained above, we can use a statistical method to split the lines and obtain ν_c^* and ν_a^*, which correspond to the cyclotron and anomaly resonance frequencies at the average energy of the axial oscillator. Compared with the line-fit method of Sec. 4.6.1, which attempts to extract ν_c^0 and ν_a^0, the line-center method has two advantages.

First, the requirements on good histogram statistics are reduced. In a fit of the cyclotron histogram, the sources of broadening from the rounding parameter and from the temperature parameter need to be distinguished, so good statistics are required. The requirements on statistics for computing a weighted average are not as stringent.

Secondly, no model for the rounding of the measured line shapes needs to be developed in the line-center method. The rounding of the line shapes occurs because, through an unknown mechanism, the distribution of B-field values sampled by the electron is modified from a Boltzmann distribution. However, the particular form of the non-thermal distribution is not important, since the weighted mean of the modified cyclotron and anomaly histograms will both reflect the modified average oscillation frequency.

Line-Center Calculation Details

The weighted center ν^* of a frequency distribution is given by

$$\nu^* = \frac{\sum \nu_i w_i}{\sum w_i}\,, \tag{4.13}$$

where ν_i are the frequencies and w_i are the assigned weights. The weight for a particular point should be proportional to the area under the portion of the curve represented by that point. In the algorithm used for this work, the weight is approximated by a trapezoid rule, where lines to the neighboring points are used to estimate area under the curve. Each point in the histogram is assigned a height uncertainty based on the binomial distribution, and that error is propogated through Eq. (4.13) to obtain an estimate of uncertainty in the weighted center ν^*. Since $g/2 \approx 1 + \nu_a/\nu_c$, the error in g is given by

$$\frac{\Delta g}{g} \approx 10^{-3}\sqrt{\left(\frac{\Delta\nu_a^*}{\nu_a^*}\right)^2 + \left(\frac{\Delta\nu_c^*}{\nu_c^*}\right)^2}\,. \tag{4.14}$$

The results of the line-fit method and the line-center method for one pair of anomaly and cyclotron scans is shown in Fig. 4.6.

Line-Center Calculation Results

The uncertainty estimate discussed above will not be accurate for poor statistics or for too few frequency bins. Therefore, the spread of a sample of many g value measurements is considered a better estimate of the true statistical uncertainty associated with the line-center method. To evaluate the statistical performance of the line-center method, we consider data sets taken at $\nu_c = 149.0$ GHz, shown in Fig. 4.8. These data were taken as searches for anomaly and cyclotron drive-power systematic effects. As discussed in Ch. 6, the fits shown in the graphs are consistent with vanishing power shifts, but for our purposes here we simply consider the fit residuals. A histogram of the residuals is shown in Fig. 4.9.

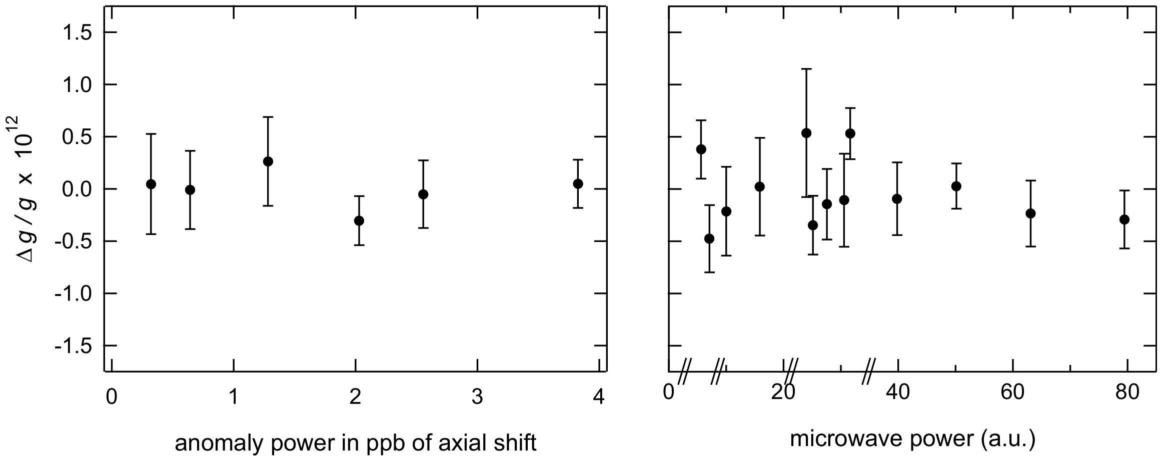

Figure 4.8: Searches for anomaly (left) and cyclotron (right) drive systematics taken at $\nu_c = 149.0$ GHz. The g value measurements are obtained using the line-center method. Due to an anharmonicity-induced systematic shift which was not properly accounted for in the data of the left graph (see Sec. 6.2.2), there is a small offset ($\sim$ 0.2 ppt) between the g value measurements obtained from the two graphs which has been subtracted out here.

A few things are to be noted from these plots. First, the total repeatability of the g value data is quite impressive: there is about 1 ppt full range scatter, with a standard deviation of 0.32 ppt. Propogating errors through the line-center method and then averaging the results yields a mean uncertainty of 0.36 ppt. The agreement between these two error assignments is good; it can be concluded that the line-center method does not grossly underestimate the uncertainty. (This conclusion is also fairly obvious by cursory inspection of the distributions and error bars shown in Fig. 4.8.)

There is no known reason to expect systematic errors in the line-center calculations, since the frequency bin width is less than the width of the sharpest features

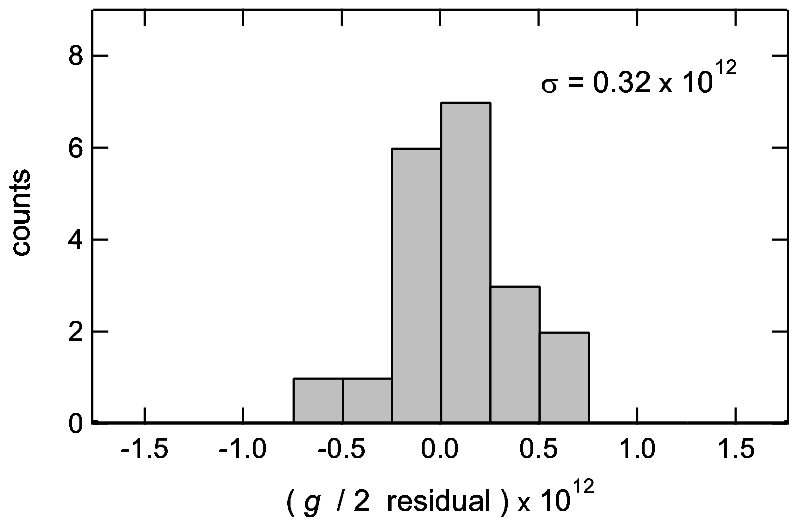

Figure 4.9: Histogram of residuals of linear fits to the data shown in Fig. 4.8.

in the histograms. However, in order to search for a possible systematic effect, the results of the line-center method can be compared with the results of the line-fit method. This comparison is shown in Fig. 4.7. Besides noting that the error bars obtained from the line-center calculation once again seem consistent with the scatter, it is also noted that the two methods show very good agreement. There is no reason to expect any systematic shifts of the two methods to be correlated, so the agreement between the g value measurements shown in Fig. 4.7 is taken as an encouraging sign. Comparison of the line-center method to a more crude line-fit method (one which does not include a rounding parameter) has been performed [78]. The agreement between these two techniques was also found to be good. Thus, the line-center method is used in the final g value analysis presented in this thesis.

Chapter 5

Cavity Shifts

Standing-wave modes of the electromagnetic field in the cavity formed by Penning trap electrodes modify the behavior of the cyclotron oscillator. The cyclotron damping rate is altered, and the cyclotron frequency can be substantially shifted. Cavity shifts, which were estimated but not observed, limited the accuracy of a previous g value measurement in a hyperbolic trap to 4.3 parts per trillion (ppt). In contrast with a hyperbolic Penning trap, a cylindrical trap allows the identification of observed electromagnetic modes with TE and TM modes, each having a well-characterized coupling to the cyclotron oscillator. The cavity-induced systematic shift of a g value measurement in the cylindrical Penning trap can then be calculated precisely [87].

In this experiment, we observe and identify cavity modes of the cylindrical trap in the frequency region of interest. We also present the first demonstration of the dependence of inhibited spontaneous emission with detuning of the cyclotron frequency from cavity mode frequencies. Finally, we present the first demonstration of g value shift with detuning from mode frequencies and find that the cavity-induced shift agrees well with theory for the measured mode spectrum of the trap. The preliminary g value measurement presented here obtains a 0.6 ppt uncertainty due to cavity shifts, which is currently the leading uncertainty of the measurement.

5.1 Calculation of Cavity Effects

In free space, a cyclotron oscillator with $\omega_c = (2\pi)$ 150 GHz loses energy via synchrotron radiation with a time constant $\tau_c = 1/\gamma_c = 0.08$ s. In a lossless microwave cavity, synchrotron radiation only occurs at certain eigenfrequencies of the electromagnetic field with the correct geometry. In a lossy cavity, synchrotron radiation at frequencies between these mode frequencies is not forbidden, but its suppression leads to inhibited spontaneous emission, i.e. an enhanced cyclotron lifetime [57]. When the cyclotron frequency ω_c is tuned near the frequency of a coupled cavity mode, spontaneous emission is enhanced.

The cyclotron oscillator also experiences frequency shifts due to interaction with the electromagnetic cavity modes. It is tempting to guess that the cyclotron oscillator will shift *toward* the nearest cavity mode, where synchrotron radiation is more strongly allowed. However, as discussed in Sec. 5.1.4, the effect of the interaction with a cavity mode is to repel the cyclotron oscillator *away* in frequency. The result of a repelled frequency is what one would expect considering that, in general, the eigenfrequencies of a system of coupled oscillators are repelled from one another.

5.1.1 Cavity Shifts of a g value Measurement

The field geometry, resonant frequency, and quality factor of each cavity mode determines its contribution to the cyclotron damping rate γ and to the shift of the cyclotron frequency $\Delta\omega \equiv \omega - \omega_c$ [88, 68]. The effects of the cavity modes on the spin frequency are well below the projected accuracy of foreseeable g value experiments [89, 90].

Neglecting small corrections, the g value is calculated from the measured anomaly frequency ω_a and the measured cyclotron frequency ω_c by

$$\frac{g}{2} \approx 1 + \frac{\omega_a}{\omega_c} = 1 + \frac{\omega_s - \omega_c}{\omega_c} = \frac{\omega_s}{\omega_c}\,. \tag{5.1}$$

Since ω_s is not modified by cavity mode interactions, the cavity-induced shift in the g value is given by

$$\frac{\Delta g}{g} = \frac{\Delta\omega}{\omega_c}\,. \tag{5.2}$$

5.1.2 Coupled Cavity Modes

Cavity modes with an electric field at the trap center perpendicular to $\vec{B} = B\hat{z}$ couple to the cyclotron oscillator. The electromagnetic eigenmodes of a cylindrical cavity are commonly labeled as TE_{mnp} and TM_{mnp} [91]. The TE modes have $E_z = 0$ over all space, and the TM modes have $B_z = 0$, where $\hat{z}$ is the cylinder axis. Of interest for a g value measurement are the TE and TM modes with $m = 1$ and odd p, which have a non-vanishing transverse electric field at $z = 0$, as depicted in Fig. 5.1. A non-vanishing transverse electric field at $z = 0$ allows these modes to couple to the cyclotron motion of a centered electron.

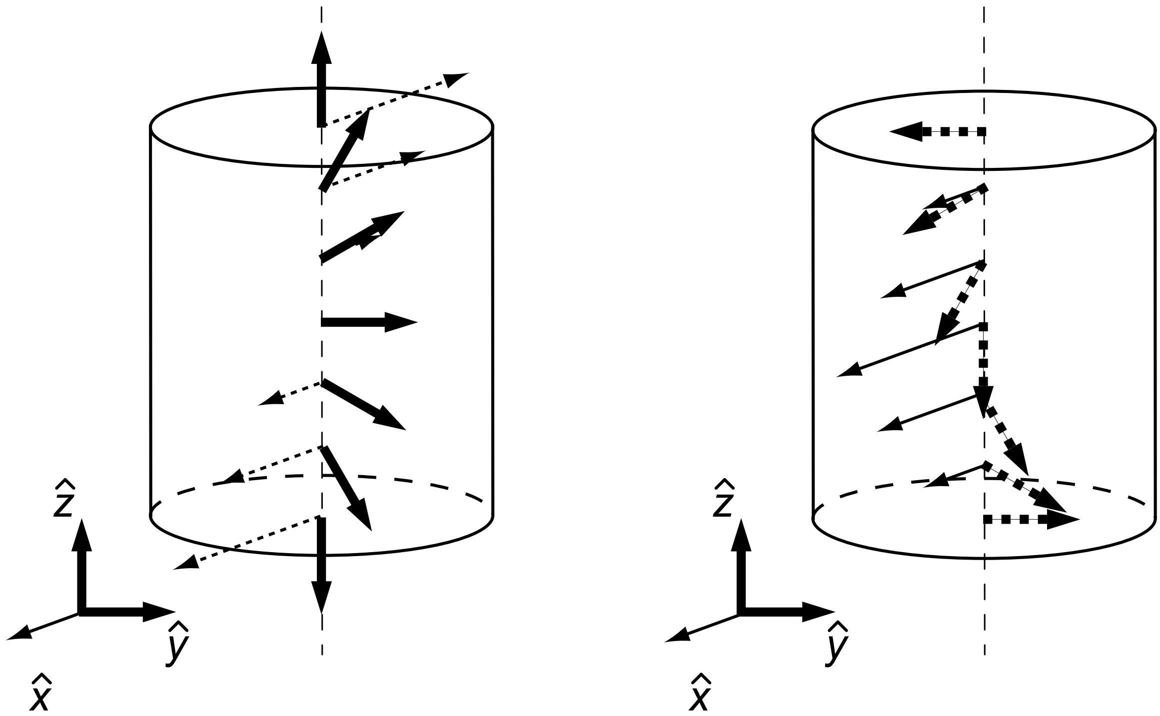

Figure 5.1: Field geometry of cavity modes TM_{1n1} (left) and TE_{1n1} (right) along the cylinder axis $\hat{z}$. Magnetic field is represented by a dashed vector and electric field by a solid vector. Heavy vectors are confined to the $\hat{y} - \hat{z}$ plane, and light vectors are parallel to $\hat{x}$. The non-vanishing transverse electric field of these modes at the trap center allows them to couple to the cyclotron oscillator. Modes with $p > 1$ have more transverse field nodes along $\hat{z}$.

5.1.3 Cavity Effects in a Hyperbolic Trap

In a traditional hyperbolic Penning trap cavity, although the standing-wave modes of the radiation field do not correspond to TE and TM modes, the effects of the modes on a g value experiment can be calculated [56]. However, there are a few drawbacks that make hyperbolic traps less favorable than cylindrical traps for minimizing cavity shift errors.

Because of its reduced symmetry, a hyperbolic trap geometry has roughly twice the density of coupled modes than does a cylindrical trap of equivalent size [56].

The lower symmetry of the hyperbolic geometry and the poorly defined boundary conditions of the asymptotic region are expected to make the mode Qs tend toward lower values. This effect, combined with the higher mode density, raises the question as to whether the coupled modes of an actual hyperbolic trap can be experimentally identified, which is necessary for accurate calculation of cavity shifts [68]. Cavity modes of a hyperbolic trap have been observed [92], but they were not identified with a predicted spectrum.

One solution to the cavity shift problem is to construct trap electrodes from a lossy material, deliberately lowering the Q of the trap in an approximation to the free-space limit. A lossy phosphor bronze trap [3, 8] demonstrated some success in this approach, but the observed inhibited spontaneous emission factor of up to 2 to 4.5 over a 2% change in B showed that cavity modes were still playing a role. However, this measurement was limited to $\Delta g/g = 4.0$ ppt by other problems (some of which were actually incurred by complications associated with the short cyclotron lifetime.)

Another solution to the cavity shift problem, used in the Harvard g value measurement presented here, is to work in a high-Q trap where the geometry is more conducive to precise understanding of cavity shifts. In fact, it was the problem of cavity shifts which originally led to the development of cylindrical Penning traps [73].

5.1.4 Cavity Effects in a Cylindrical Trap: Mode Sum Calculation

Cavity effects in a cylindrical Penning trap can be approximated as a sum over cavity modes [84, 88]. The interaction between the cyclotron oscillator at frequency

ω_c and only one cavity mode would impart to the cyclotron oscillator a damping rate γ and a frequency shift $\Delta\omega$ given by

$$\Delta\omega = \frac{\gamma_M}{2}\frac{\delta}{1+\delta^2}\,, \tag{5.3}$$

$$\gamma = \gamma_M \frac{1}{1+\delta^2}\,, \tag{5.4}$$

where δ is the detuning parameter (defined below) and γ_M is the maximum cyclotron damping rate obtained at $\delta = 0$. The unperturbed resonance frequencies of the cyclotron and cavity oscillators are related by

$$\omega_c = \omega_M + \frac{1}{2}\Gamma_M \delta, \tag{5.5}$$

where ω_M and Γ_M are the frequency and width of a TE or TM mode. Γ_M is related to Q_M, the mode quality factor, by $Q_M = \omega_M/\Gamma_M$. It is convenient to express the maximum damping rate γ_M in terms of the measured mode frequency and quality factor and the analytically calculated coupling constant λ_M:

$$\frac{\gamma_M}{\omega_M} = 2\,Q_M \left(\frac{\lambda_M}{\omega_M}\right)^2. \tag{5.6}$$

We can now express the frequency shift and damping rate, summed over all cavity modes, in terms of measured mode frequencies and quality factors and calculated coupling constants:

$$\Delta\omega - \frac{i}{2}\gamma = \sum_M \frac{\omega_c \lambda_M^2}{\omega_c^2 + i\,\omega_c\,\omega_M/Q_M - \omega_M^2}\,. \tag{5.7}$$

For the TE_{mnp} modes,

$$\lambda_{mnp}^2 = \begin{cases} \dfrac{r_e c^2}{z_0 \rho_0^2}\dfrac{1}{\alpha_{mn}^2 - 1}\dfrac{2\alpha_{mn}^2}{J_m(\alpha_{mn})^2} & \text{for } m = 1 \text{ and } p \text{ odd} \\ 0 & \text{for } m \neq 1 \text{ or } p \text{ even} \end{cases} \tag{5.8}$$

$$\omega_{mnp}^2 = \left(\left(\frac{p\pi}{2z_0}\right)^2 + \left(\frac{\alpha_{mn}}{\rho_0}\right)^2\right) c^2, \tag{5.9}$$

mode	eigenfrequency (GHz)	$\lambda_M^2 \times 10^{10}$ (s^{-2})	measured frequency (GHz)
TM_{131}	108.8	0.3	
TE_{125}	111.8	5.8	
TM_{125}	121.6	4.7	
TM_{133}	121.8	2.5	
TE_{141}	124.7	12.5	
TE_{135}	132.0	9.2	131.7
TE_{143}	136.2	12.5	135.7
TE_{117}	136.7	2.8	136.7
TM_{117}	141.2	3.8	141.4
TM_{141}	141.6	0.3	141.9
TM_{135}	144.3	4.9	144.5
TE_{127}	146.5	5.9	146.3
TM_{143}	151.7	2.1	151.8
TM_{127}	154.2	5.8	154.3
TE_{145}	156.6	12.5	
TE_{151}	157.6	15.8	
TE_{137}	162.4	9.2	
TE_{153}	166.8	15.8	
TM_{145}	170.3	4.6	
TM_{137}	172.6	6.7	

Table 5.1: Calculated cavity mode frequencies and coupling constants (second and third columns) for modes near the region used for g value measurements. The mode-frequency calculation uses the experimentally determined best-fit trap dimensions discussed in Sec. 5.2.4. The final column gives measured frequencies of the observed modes.

where $r_e = e^2/mc^2$ is the classical radius of the electron, ρ_0 is the cavity radius, and α_{mn}, given by $J'_m(\alpha_{mn}) = 0$, is the nth zero of the derivative of the mth-order Bessel function.

For the TM_{mnp} modes,

$$\lambda^2_{mnp} = \begin{cases} \dfrac{r_e c^2}{z_0 \rho_0^2} \left(\dfrac{p\pi c}{z_0 \omega_{mnp}} \right)^2 \dfrac{1}{2J_0(\beta_{mn})} & \text{for } m = 1 \text{ and } p \text{ odd} \\ 0 & \text{for } m \neq 1 \text{ or } p \text{ even} \end{cases} \tag{5.10}$$

$$\omega^2_{mnp} = \left(\left(\frac{p\pi}{2z_0} \right)^2 + \left(\frac{\beta_{mn}}{\rho_0} \right)^2 \right) c^2, \tag{5.11}$$

where β_{mn} (given by $J_m(\beta_{mn}) = 0$) is the nth zero of the mth-order Bessel function.

Calculated mode frequencies and coupling constants for m=1, p-odd modes for best-fit trap dimensions (see Sec. 5.2.4) are given in Table 5.1. The calculated g value shift and damping rate due to an example cavity mode, TE_{127}, is shown in Fig. 5.2.

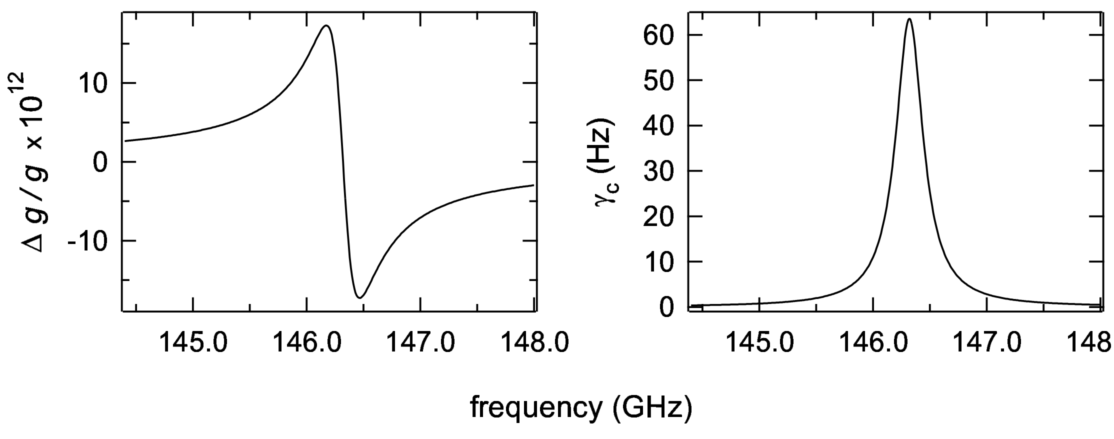

Figure 5.2: Mode sum prediction for g value shift (left) and cyclotron damping rate (right) for cavity mode TE_{127} with $Q = 500$. No other modes are included in the calculation.

5.1.5 Cavity Effects in a Cylindrical Trap: Renormalized Calculation

Unfortunately, the mode sum calculation discussed in Sect. 5.1.4 does not include renormalization corrections related to the self-field interaction of the electron. The mode frequencies shown in Table 5.1 remain correct, as they are actually derived from the full calculation discussed in this section. When applied far off resonance, Eq. (5.3) is dominated by the unphysical back-reaction of the electron self field. The resulting error becomes large when predicting the cavity effects far off resonance, and the results actually diverge. The exact solution, obtained by summation over image charges rather than over cavity modes, can be properly renormalized and does not suffer from self-field interaction problems [87] [68]. In the renormalized solution, Eq. (5.7) of the mode sum calculation is replaced by

$$\Delta\omega - \frac{i}{2}\gamma = -\frac{i}{2}\gamma_c + \omega_c \left[\Sigma_S(\tilde{\omega}_c) + \Sigma_P(\tilde{\omega}_c)\right], \tag{5.12}$$

where the complex frequency $\tilde{\omega}_c = (1 + i/2Q)\,\omega_c$ accounts for cavity lossiness. Σ_S describes the interaction with the sides of the cavity and Σ_P describes the interaction with the parallel plates. These expressions are given by

$$\Sigma_S(\omega) = -\frac{r_e}{z_0}\sum_{n=0}^{\infty}\left\{\frac{K_1'(\mu_n\rho_0)}{I_1'(\mu_n\rho_0)} + \frac{k_n^2c^2}{\omega^2}\left[\frac{K_1(\mu_n\rho_0)}{I_1(\mu_n\rho_0)} - \frac{K_1(k_n\rho_0)}{I_1(k_n\rho_0)}\right]\right\}, \tag{5.13}$$

$$\begin{aligned}\Sigma_P(\omega) =& \frac{r_e}{z_0}\ln\left[1 + e^{2i\,\omega z_0/c}\right] - \\ & \frac{r_e}{z_0}\sum_{n=1}^{\infty}(-1)^n\left[e^{2in\omega z_0/c}\left(\frac{ic}{2n^2 z_0\,\omega} - \frac{c^2}{4n^3 z_0^2\,\omega^2}\right) + \frac{c^2}{4n^3 z_0^2\,\omega^2}\right],\end{aligned} \tag{5.14}$$

where

$$k_n = (n + \frac{1}{2})\pi/z_0, \tag{5.15}$$

$$\mu_n = (k_n^2 - \omega^2/c^2)^{1/2}. \tag{5.16}$$

Unfortunately, in the renormalized model, cavity lossiness cannot be assigned individually for each mode, since the sum is performed over image charges rather than over modes. However, a slightly different treatment of cavity loss than described above can assign different quality factors Q_E and Q_M to the TE and TM modes respectively. This is achieved by taking $\omega \to (1 + i/2Q_E)\,\omega$ in the denominator function $I_1'(\mu_n\rho_0)$ of Eq. (5.13) while all other frequencies in Eqs. (5.13) and (5.14) are given by $(1 + i/2Q_M)\,\omega$.

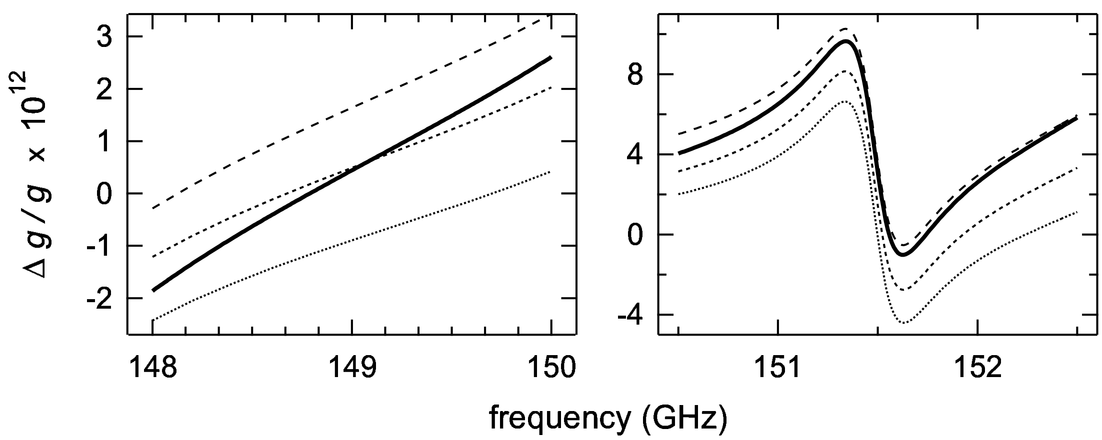

Figure 5.3: Left: comparison of g value shift between modes TE_{127} and TM_{143} of renormalized calculation (solid) and mode sum calculation for four (dots), six (short dash), and eight (long dash) modes included. Right: comparison of g value shift across mode TM_{143} using the renormalized calculation (solid) and mode sum calculation for three (dots), five (short dash), and seven(long dash) modes included.

Another drawback of the renormalized calculation is that frequencies of cavity modes cannot be individually adjusted; the only input parameters are the cavity Q

and trap dimensions ρ_0 and z_0. Even when the trap dimensions are determined *in situ*, perturbations due to slits between electrodes shift the mode frequencies (see Sec. 5.2).

Comparisons between results of the mode sum calculation and the renormalized calculation are shown in Fig. 5.3. The mode sum calculation is not sufficiently accurate to be used in a part-per-trillion g value measurement. However, since the mode sum calculation allows the couplings and frequencies of cavity modes to be individually adjusted, its flexibility can be useful in certain estimates of cavity effects. For instance, it is worth noting the 5 ppt offset from zero of the exact calculation in the right-hand plot of Fig. 5.3. Comparison to the mode sum calculations in this figure suggests that for a g value measurement, where ω_c is tuned between the two *nearest* modes, offsets caused by *non-nearest* modes can contribute at the few ppt level.

5.1.6 Dependence of Cavity Effects on Mode Q-Factor

To minimize cavity shifts in a g value measurement, the magnetic field should be tuned such that ω_c is between the frequencies of coupled cavity modes. Given a choice of cyclotron frequency, one can ask what the optimal mode Q-factor would be. Combining Eqs. (5.3) through (5.6), we arrive at

$$\Delta\omega_c = \left(\frac{\lambda_M^2 S_M}{\omega_M}\right)\frac{Q_M^2}{1+S_M^2 Q_M^2}\,, \tag{5.17}$$

$$\gamma = \left(\frac{\lambda_M^2}{\omega_M}\right)\frac{Q_M}{1+S_M^2 Q_M^2}\,. \tag{5.18}$$

where ω_M is the mode frequency and $S_M = 2|\,\omega_c - \omega_M|\,/\omega_M$ is the fractional mode spacing, assuming ω_c is tuned halfway between modes.

While Eq. 5.18 shows that lower mode Q-factors lead to smaller g value shifts, in practice one would need to make Q so low that the modes were significantly overlapping (and therefore difficult to identify) in order to substantially reduce the shift. Fig. 5.4 shows the effects of Q-factor on the damping rate and g value shift for one cavity mode.

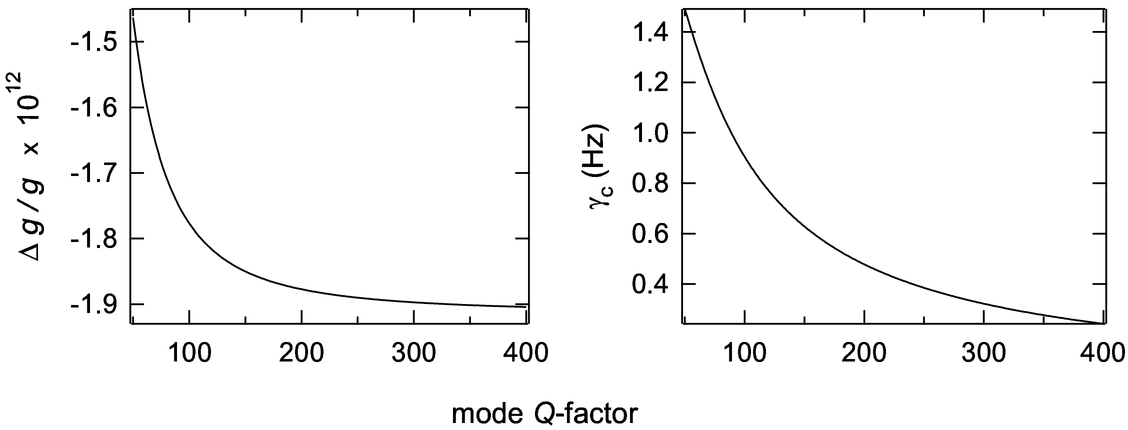

Figure 5.4: Dependence of g value shift and cyclotron damping rate on mode Q-factor. Results were obtained using the mode sum calculation with contributions only from TE_{127} and the cyclotron frequency tuned halfway between TE_{127} and TM_{143}. The renormalized calculation also yields saturated behavior for the g value shift at modest values of Q.

One important result shown in Fig. 5.4 is that, unlike the damping rate, the g value shift saturates for mode Q above ~ 100. Generally, the dependence of the g value shift on Q is saturated if ω_c is detuned from the nearest cavity mode by more than the mode width, a condition easily obtained in cylindrical Penning traps. Thus, the renormalized calculation for g value shifts is not limited by the fact that it does not individually parameterize mode Q-factors. Also, precise knowledge of mode Q-factors is not necessary for the g value measurement presented in this work. Fig. 5.17 shows the effects of a large range of Qs on the damping rates and cavity shifts.

5.2 Measured Mode Spectrum of the Actual Trap

To understand cavity shifts of ω_c, the cavity mode spectrum must be known. This measured spectrum is compared with predicted spectra to make a best-fit determination of actual trap dimensions and to identify the measured modes (see Sect. 5.2.3). Trap dimensions, obtained *in situ* by this technique, are used in the renormalized calculation of cavity shifts discussed in Sect. 5.1.5.

5.2.1 Mapping the Cavity Modes

The most direct technique for measuring the cavity mode structure would be to map the field-dependence of the cyclotron damping rate. This map would directly yield frequencies and Q-factors of only the coupled modes. It would also yield an absolute measure of the cavity coupling versus frequency and could thus be used as a test of the renormalized calculation.

In practice, making a mode map using the cyclotron damping rate presents several challenges. Gathering statistics at each field value takes several hours, making it a tedious process to obtain a detailed map. Also, it is technically challenging to measure the short cyclotron lifetime in the vicinity of a cavity mode.

In this work, we measure cavity mode frequencies by observing the response of a large cloud of electrons to an axial parametric drive [93], discussed in Sec. 2.3.5. For a cloud of electrons, the axial and perpendicular electron motions are coupled by collisions. The response of a cloud to the parametric axial drive depends on the total rate at which injected energy is lost, and thus through collisions is sensitive to synchrotron coupling to the cavity.

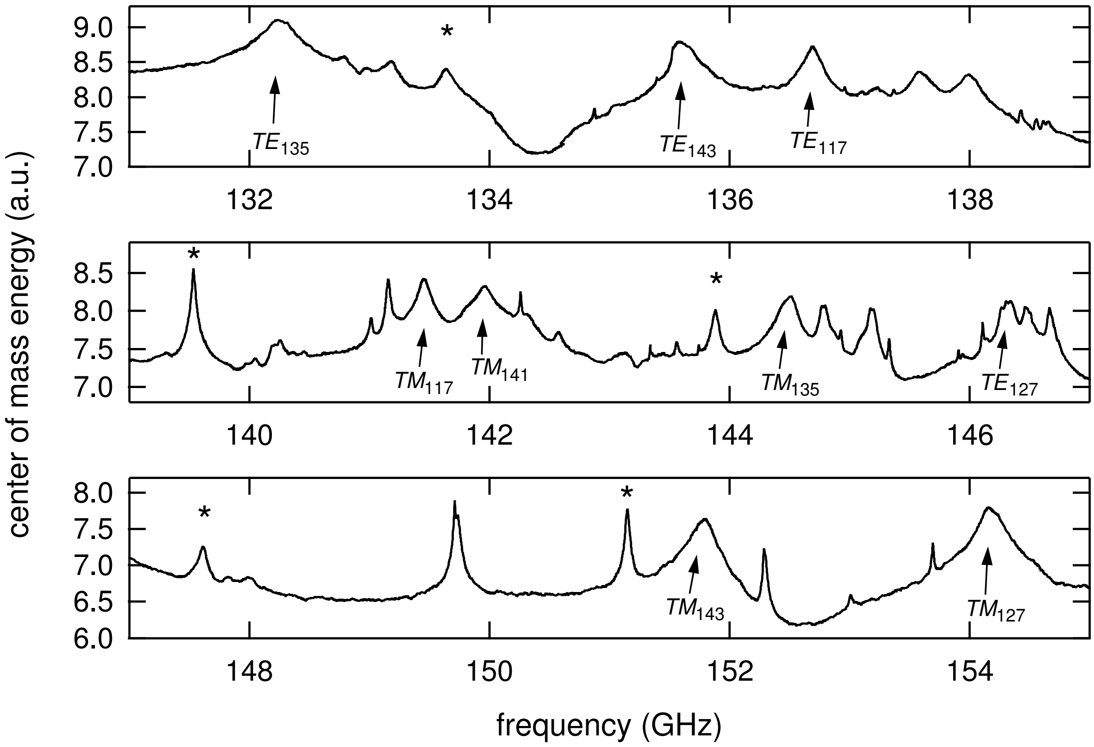

Figure 5.5: Mode map over the nine observed coupled cavity modes, made using a parametrically driven cloud of 3×10^4 electrons. Calibration peaks (see Sec. 5.2.2) are marked with asterisks.

From a map of the axial parametric response, the frequencies of modes which couple to the cyclotron motion can be determined. Fig. 5.5 shows such a mode map across several coupled cavity modes. Unlike for a single electron, the finite size of an electron cloud allows it to couple to cavity modes with vanishing transverse electric field at the trap center. Identification of the modes which couple to a single electron is discussed in Sec. 5.2.3 and Sec. 5.2.4.

5.2.2 Calibration of Cavity Mode Maps

A cavity mode map is created by observing the parametric axial response of a cloud of electrons as the magnet current is changed. Fig. 5.6 shows the schematic diagram of the magnet charging circuit. In order to create a map of parametric response versus field, the measured magnet current must be calibrated. For a constant charging voltage V, the magnetic field $B(t)$ as a function of measured return current $I_T(t)$ is given by [72]

$$B(t) = g\left(I(0) + \frac{V}{L}(t - \tau_0)\right), \tag{5.19}$$

where L is the coil inductance, g is a factor describing the coil geometry, I is the solenoid current, and the constant τ_0 is related to the fact that some charging current flows through the resistors R_1 and R_2. The solenoid current is given in terms of the measured return current I_T by

$$I(t) = I_T(t) - I_{R1}(t) - I_{R2}(t) - I_{shims} - I_{R3}(t). \tag{5.20}$$

Even though the presence of the constant τ_0 and the combination of all currents at the shunt resistor present complications, it is possible [72] to obtain a calibration for the magnetic field $B(t)$ versus measured return current $I_T(t)$.

Unfortunately, the equipment used for this work produced anomalies in charging behavior which prevent the use of Eq. (5.19) to calibrate the current. Oscillations of unknown origin in the measured current were on the order of 0.1 A; although not ideal, these could be averaged away. However, the measured charging rate, typically between 0.5 and 1.5 mA/s, was subject to sudden interruptions lasting several minutes before a similar, but not identical, charging rate returned. An example of the charging

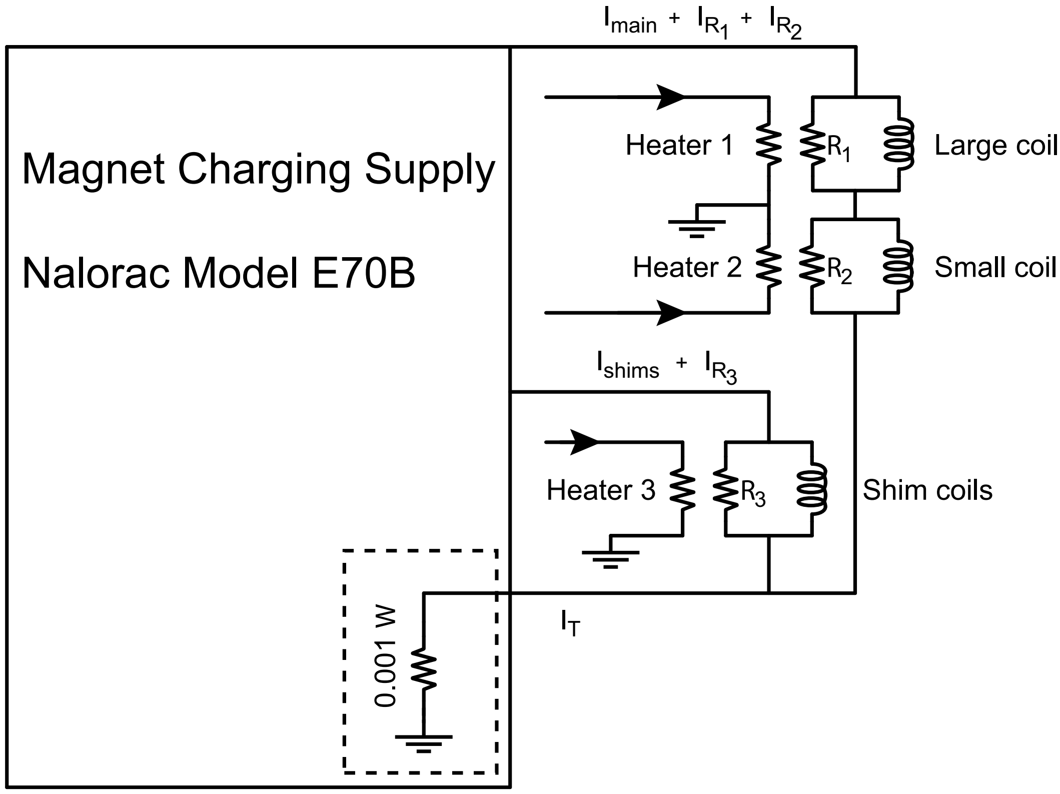

Figure 5.6: Schematic diagram of magnet charging circuit.

oscillations and interruption are shown in Fig. 5.7. When the current was calibrated by the method discussed below, it was found that the proportionality constant gV/L in Eq. (5.19) varied by as much as 5%. Since calibration of Eq. (5.19) requires sweeping back and forth across a cavity mode, but the proportionality constant tended to jump when the charging direction was changed, calibration of B versus I_T was impractical. The source of these problems is unknown, but they are presumably related to instabilities in the charging voltage or the value of the shunt resistor.

The final calibration of cavity mode maps was performed in such a way that knowledge of the exact relationship between return current and field was not needed.

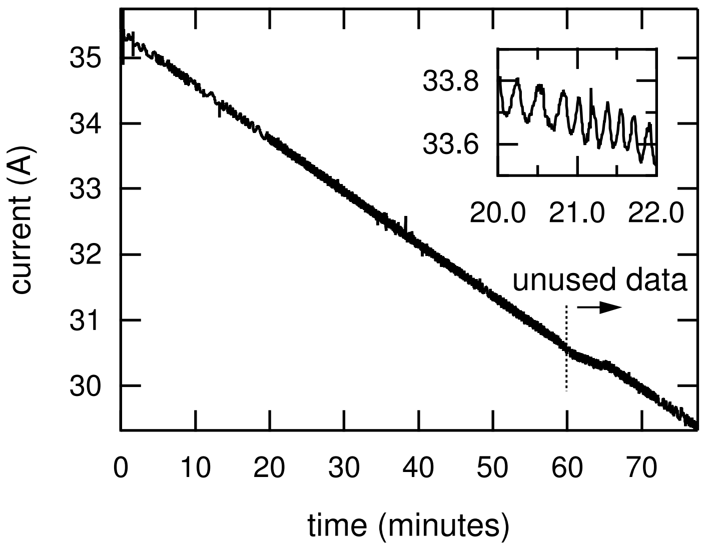

Figure 5.7: Return current through the shunt resistor while discharging the magnet using V_c = - 0.25 V. Data after the interruption in charging rate are not used. Inset: expanded graph showing return current oscillations.

The magnetic current was tuned so that the parametric response indicated that the cyclotron frequency was at a peak of one of the narrow cavity modes which couple weakly to a cloud but not to a single electron. The cyclotron resonance frequency of a single electron was then measured at each of these calibration peaks to obtain the B-field at these points. The calibration peaks are marked in Fig. 5.5.

This calibration technique allows each mode map to be calibrated individually. The current offsets from the shim current and from the parallel resistors do not need to be known. However, the technique relies on these offsets being static. Toward this goal, as indicated in Fig. 5.7, only portions of maps free of charge-rate shifts were used in any calibration. Although the constants vary, as shown in Fig. 5.8, the used portions of each map had good linearity between measured current and the cyclotron frequency at the calibration peaks. The rms value of residuals over all calibration

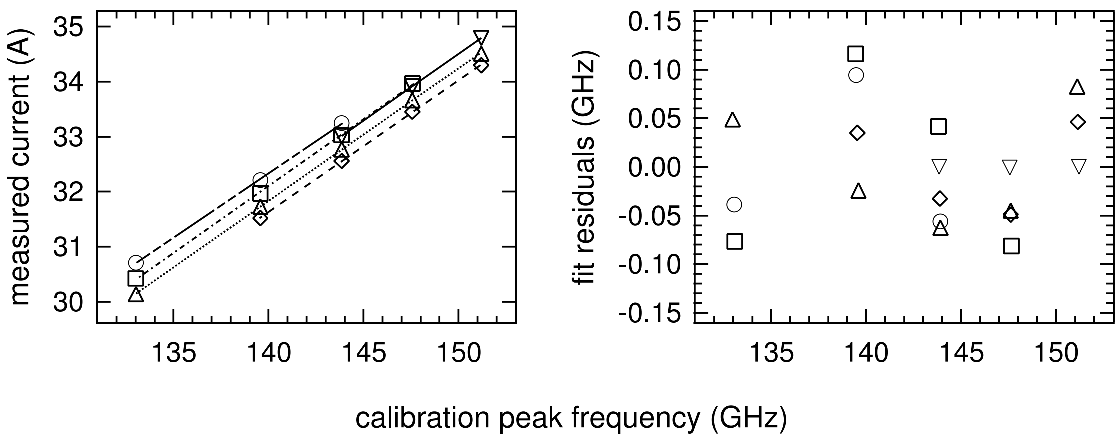

Figure 5.8: Left: measured return current at calibrated peak frequencies for used parametric mode maps. Right: frequency residuals of linear current-frequency calibration fits.

peaks on all maps is 0.060 GHz.

Several separately calibrated maps are combined in order to make best estimates of the frequencies of coupled cavity modes. The identification of these modes in each map is discussed in Sec. 5.2.3. The scatter of these frequencies, shown in Fig. 5.9, provides an absolute determination of the ability to assign a frequency to a feature of the mode spectrum, and is thus crucial for estimating cavity shifts in a g value measurement. The rms calibration scatter over all observed coupled modes is 0.27 GHz, corresponding to an average fractional scatter of 0.15%. One of the calibrated maps shown in Fig. 5.9 was taken at 60% the charging rate of the others, as well as after a (non-intentional) magnet quench and trap thermal cycling, demonstrating the mode structure to be robust against measurement technique and physical stresses on the trap.

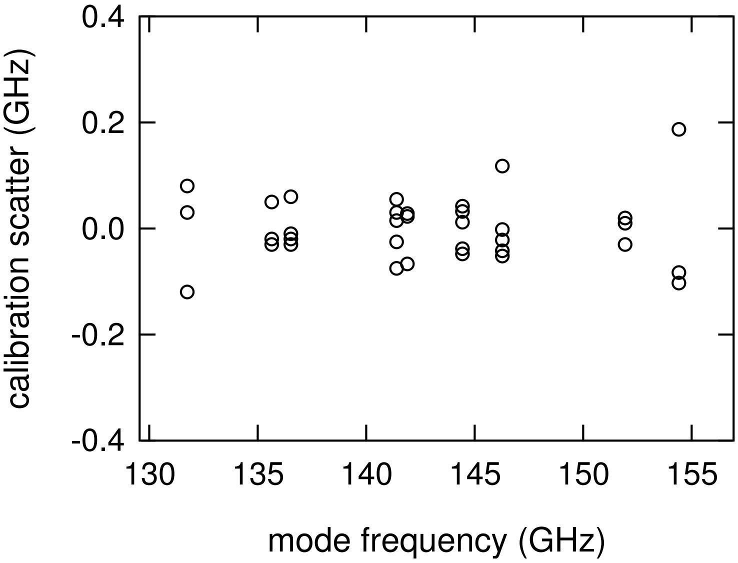

Figure 5.9: Scatter in determination of frequencies of coupled cavity modes.

5.2.3 Identification of Coupled Cavity Modes

Identification of coupled cavity modes in the measured mode maps is necessary in order to choose a magnetic field value for which the cyclotron frequency suffers from a minimal cavity shift. Also, as discussed in Sec. 5.2.4, the measured frequencies of observed coupled cavity modes is used in an *in situ* determination of the cavity dimensions.

Cavity modes which couple to a single electron can generally be recognized in mode maps such as the one shown in Fig. 5.5 as the modes of lower Q. This difference in observed Q arises because modes which couple to the single electron also couple more strongly to a cloud, creating a strong damping channel for energy in these modes. However, in some cases this indicator still leaves ambiguity. Unambiguous identification of coupled cavity modes can be made by observing which modes show saturation behavior in the parametric response of small electron clouds, as shown in Fig. 5.10.

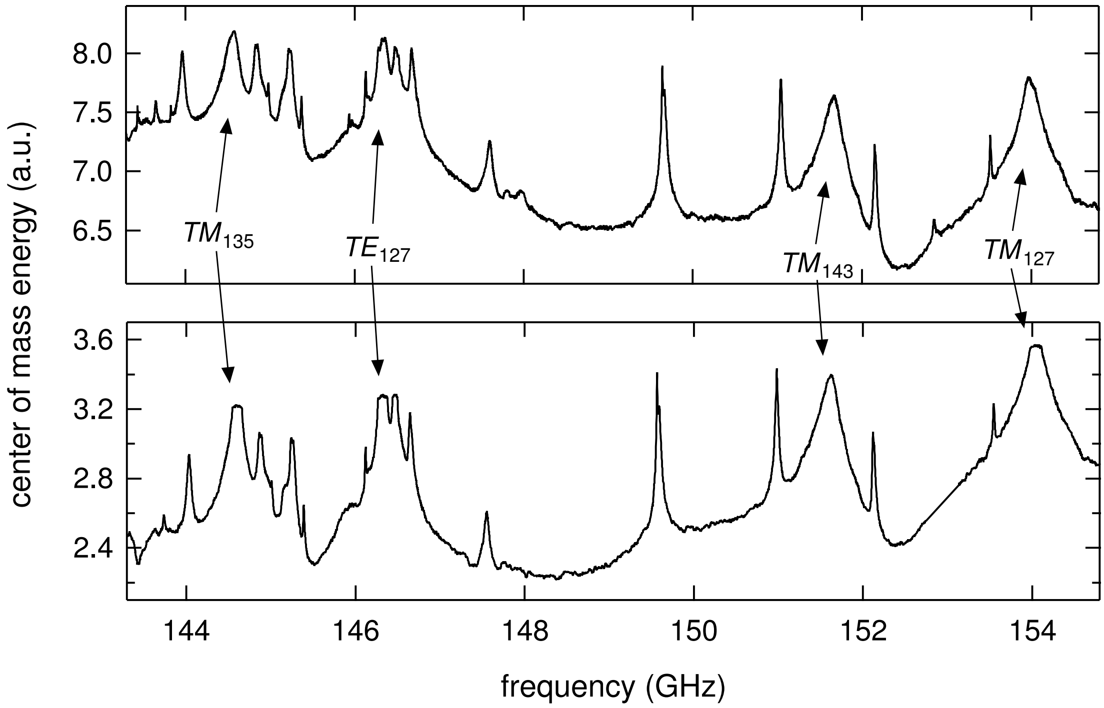

Figure 5.10: Mode map made by parametrically driving a cloud of 3×10^4 electrons (upper) and 1.6×10^4 electrons (lower). In the map made using the smaller cloud, the three strongly coupled modes with the largest coupling constants (see Table 5.1) exhibit saturation behavior. Mode maps made with even fewer electrons show more dramatic saturation.

The axial parametric response of a cloud of electrons is sensitive to cavity modes because increased cyclotron damping enables the cloud to more fully synchronize with the parametric drive, as discussed in Sec. 5.2.1. Saturation behavior is understood as full synchronization of the cloud, so that increased coupling to the cavity does not yield increased response to the parametric drive. However, the scaling of saturation threshold with cloud size is not understood. Larger clouds couple more strongly to the modes (a scaling which is understood), but they also have more electrons which must be synchronized before saturation occurs (a scaling which is not understood). In fact, earlier research [74] reports that larger clouds have a lower saturation threshold, contrary to the findings of this work.

5.2.4 *In situ* Determination of Cavity Dimensions

As discussed in Sec. 5.1.5, the mode sum calculation is not sufficiently accurate to determine cavity shifts for a g value measurement. Thus, even though the coupling strength of cavity modes can be accurately calculated, it is not sufficient to measure the frequencies of these modes to predict cyclotron frequency shifts. Instead, the dimensions of the microwave cavity must be determined and then used in the renormalized calculation.

In order to determine trap dimensions, a least-squares fit is used to find trap dimensions which best reproduce measured mode frequencies. In previous work [93], the azimuthally symmetric TE_{0np} were initially used because their induced surface currents, which flow parallel to most of the trap slits, are expected to induce mode frequency shifts smaller than those of modes with different geometries. The best-fit trap dimensions yielded an rms frequency deviation of 0.08% for these modes. Using this determination of trap dimensions, frequency deviations for the coupled modes were then observed to be typically 1%.

In this work, we use the measured frequencies of the coupled cavity modes, TE and TM with $m = 1$ and p odd. This method is used since these modes are most readily identified (see Sec. 5.2.3). Fig. 5.11 shows a contour plot of the disagreement between the frequencies of the nine observed coupled cavity modes and the frequencies predicted for a range of trap dimensions. The fitting algorithm demands a one-to-one correspondence between observed modes and predicted modes within the frequency span. Each local minimum represents a different identification of the observed cavity modes with predicted modes.

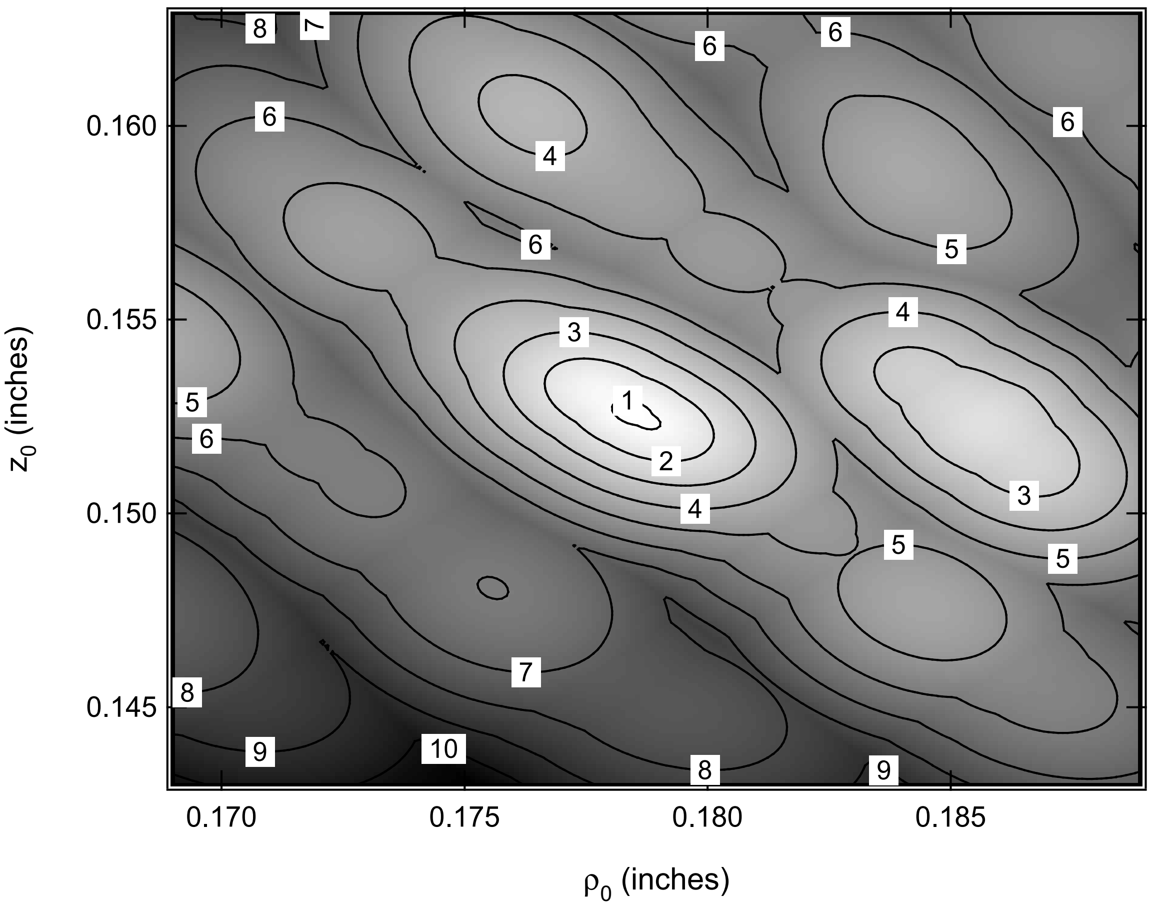

Figure 5.11: Cavity mode identification and *in situ* determination of trap dimensions ρ_0 and z_0. Shading corresponds to the rms disagreement between measured and best-match predicted spectra of coupled cavity modes for given trap dimensions. Contours are marked at intervals of 1 GHz rms error for the nine observed modes.

The global minimum, established convincingly in Fig. 5.11 as corresponding to the correct mode identification, is for trap dimensions $\rho_0 = 0.17861$ inches and $z_0 =$

0.15273 inches. (As discussed in Sec. 5.3, these dimensions differ slightly from those used for the g value analysis). For the trap dimensions given above, the rms fractional error between predicted and observed frequencies is 0.15%. The rms frequency error is 0.27 GHz. The trap was designed to have dimensions $\rho_0 = 0.1791$ inches and $z_0 = 0.1510$ inches at low temperatures. The disagreement between the targeted and observed trap dimensions is reasonable, given the expected 1-2 thousandths of an inch machining tolerance for the silver electrodes. As shown in Fig. 2.1, ρ_0 is determined by the dimension of the inner radius of each of the silver electrodes, so agreement between the expected value and the best-fit value is limited by electrode machining tolerances. Since the dimension z_0 depends on the $\hat{z}$ dimension of machining (which is in some cases more difficult) of all the silver electrodes, on the grinding of the glass spacers, and on how well these pieces fit together, a larger error is expected.

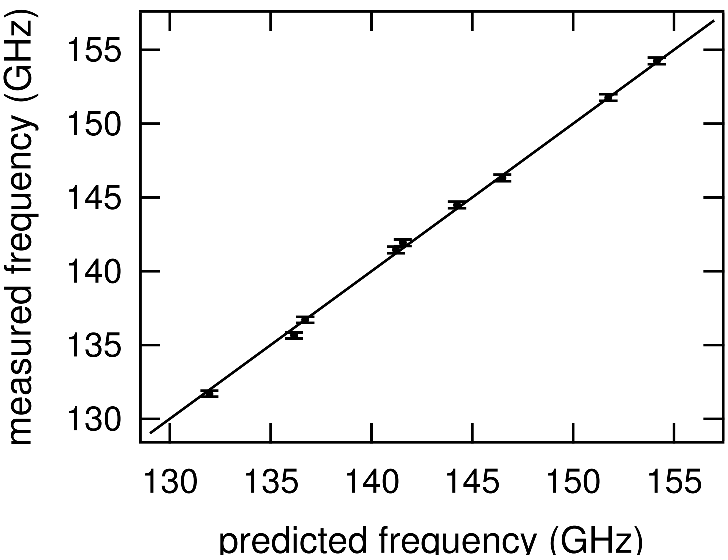

Figure 5.12: Comparison of predicted and measured frequencies of coupled cavity modes for best-fit trap dimensions $\rho_0 = 0.17861$ inches, $z_0 = 0.15274$ inches. Error bars represent the uncertainty in calibration of measured mode frequencies.

Fig. 5.12 shows good agreement between observed mode frequencies and the best-fit predictions. It is obvious in the figure that disagreements between observation and prediction are much smaller than the typical mode spacing. The uniqueness of the best fit and the agreement between predicted and observed spectra to within the calibration error confirm the mode identification and *in situ* determination of trap dimensions. Perturbations due to the slits between electrodes are also expected to cause mode frequency shifts [93], but they do not seem to present a problem for mode identification.

5.2.5 Problems with Q Determination from Parametric Maps

We found that the parametric mode-mapping technique was not as well behaved as in some previous work [72]. The 10 times deeper axial potential, the lower temperature, and the less noisy environment are candidates which might contribute to the discrepancy. Difficulties we encountered in this research might also be related to problems seen in other experiments which used the parametric resonance to measure cavity-cloud interactions [74].

As in previous work [72], the parametric response of large clouds of electrons yields mode maps with Q values of coupled modes appearing much lower than those of the non-coupled modes. There is no known reason to expect that that this would be true. The observed broadening is most likely induced by the coupling of the cloud to cavity modes, providing a strong damping channel for the mode energy. Mode maps made with fewer electrons would be expected to yield less broadening, but in this work they could not be used because of problems with saturation (see Sec. 5.2.3). Thus, the parametric mode maps we obtained are not expected to yield the correct cavity Q.

In fact, if interpreted naively, parametric maps suggests a cavity Q which is disappointingly far away from values obtained from the cyclotron lifetime data discussed in Sec. 5.3. Because of drifts and offsets in the parametric maps, the mode resonances obtained are not readily fit to Lorentzian shapes, but best attempts yielded Q values between 300 and 600. In contrast, fits using single-electron cyclotron lifetime data suggest Q values between 1000 and 10,000. Thus, the parametric mode maps are considered useful in locating the frequencies of the coupled cavity modes but not in estimating their Q values. Implications of this limitation of the parametric mode maps are discussed in Sec. 5.5.

5.3 Cyclotron Lifetime Map and Trap Parameters

In this section, we present the first map of cyclotron lifetime versus detuning from identified cavity mode frequencies. Although knowledge of the cavity Q is not critical for a g value measurement (see Sec. 5.4.3), Q_E and Q_M are estimated from the cyclotron lifetime map. Lifetime data are also used to resolve ambiguity in the assignment of TE_{127}.

5.3.1 Lifetime Measurement of a Quantum Cyclotron

The differential equation for the radial coordinates $\vec{\rho}$ of the damped cyclotron oscillator is

$$\frac{d^2\vec{\rho}}{dt^2} + \gamma\frac{d\vec{\rho}}{dt} + \omega^2\vec{\rho} = 0, \tag{5.21}$$

where γ, given by Eq. (5.12), is the damping due to interaction with cavity modes. For the underdamped case ($\gamma < \omega_0$), the energy of the oscillator obeys

$$E = E_0 e^{-\gamma t}\,, \tag{5.22}$$

which has the familiar differential form

$$\frac{dE}{dt} = -\gamma E. \tag{5.23}$$

The cyclotron damping rate is measured by observing spontaneous decays of the quantized single-electron oscillator, as discussed in Sec. 2.3.7. For the quantum cyclotron oscillator,

$$E = (n + \frac{1}{2})\hbar\omega_c, \tag{5.24}$$

where $n = 0, 1, 2, ...$ is the quantum state number. The ensemble average $\langle n\rangle$ is given by

$$\langle n\rangle = 0\cdot n_0 + 1\cdot n_1 + 2\cdot n_2 + \dots\,, \tag{5.25}$$

where n_i is the occupation fraction of the ith state. From Eq. (5.23) and Eq. (5.24), we see that the ensemble average $\langle n\rangle$ obeys

$$\frac{d\langle n\rangle}{dt} = -\gamma\langle n\rangle\,. \tag{5.26}$$

For the special case where only $|n=0\rangle$ and $|n=1\rangle$ are occupied, Eq. (5.26) and Eq. (5.25) give

$$\frac{dn_1}{dt} = -\gamma n_1, \tag{5.27}$$

which leads to

$$n_1 = e^{-\gamma t} \tag{5.28}$$

if the oscillator starts in the state $|n=1\rangle$ at $t=0$. It follows that a histogram of observed lifetimes of spontaneous decays from $|n=1\rangle \rightarrow |n=0\rangle$ forms an exponential curve with time constant $\tau = 1/\gamma$. Since Eq. (5.28) is independent of history, this is

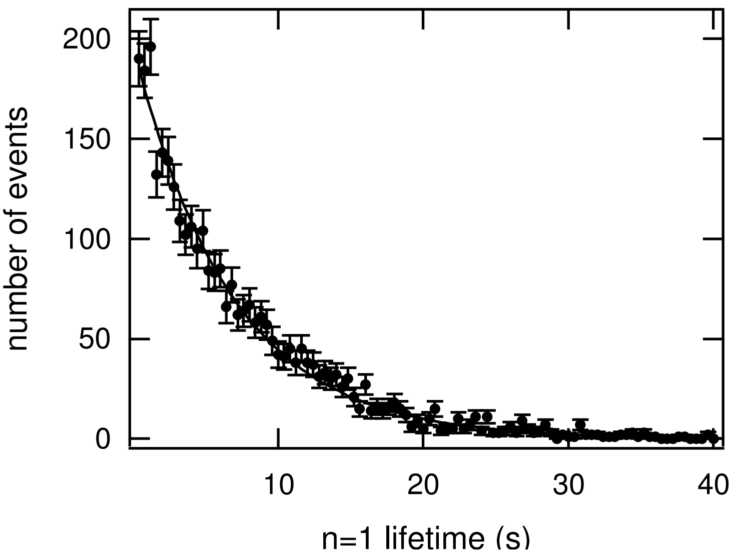

Figure 5.13: Histogram of observed lifetimes of spontaneous cyclotron decays from $|n=1\rangle \rightarrow |n=0\rangle$ at $\omega_c = (2\pi)$ 149.0 GHz. The fit gives $\tau = 1/\gamma = 6.70$ s $\pm$ 0.18 s.

true regardless of how the oscillator was prepared in the $|n=1\rangle$ state (i.e. whether it arrived there from $|n=0\rangle$ or $|n=2\rangle$) or how long it remained in that state before its lifetime began to be timed. Fig. 5.13 shows a histogram of $|n=1\rangle$ lifetimes at the value of magnetic field which yielded the longest observed lifetime in the silver trap. The measured lifetimes are given in Table 5.2.

5.3.2 Measured Damping Rates and Trap Parameters

The single-electron cyclotron lifetime has been measured at several values of magnetic field. The results are given in Table 5.2. The lifetime data are used to fit the values of Q_E and Q_M, holding trap dimensions fixed, as shown in Fig. 5.14. If more lifetime data were available, trap dimensions could also be varied in these fits, perhaps allowing trap dimensions to be determined without the use of parametrically driven electron clouds. The sizeable difference in cavity shifts induced by TE_{127} as compared to TM_{143} is due partly to the disparity of coupling strengths (see Table 5.1) and partly to the different Q values.

$\omega_c/(2\pi)$ (GHz)	cyclotron lifetime (s)
146.832	1.43 ± 0.13
147.567	5.50 ± 0.26
149.046	6.70 ± 0.18
151.196	1.38 ± 0.08

Table 5.2: Measured cyclotron lifetimes for the spontaneous decay $|n=1\rangle \to |n=0\rangle$ at various B-field values with ω_c tuned between the frequencies of TE_{127} and TM_{143}.

Fig. 5.10 shows that, of the three narrow peaks near the center of the TE_{127} pedestal, the left two peaks are the best candidates for TE_{127}. The broad pedestal, not typical of other cavity modes in the spectrum, is presumably due to contributions of many non-coupled cavity modes. Fits of Q_E and Q_M to the lifetime data are performed for both assignments of the TE_{127} frequency, as shown in Fig. 5.14. The results of the fits are given in Table 5.3. The more reasonable Q_E value obtained for the left-hand peak make this frequency assignment for TE_{127} the favored choice.

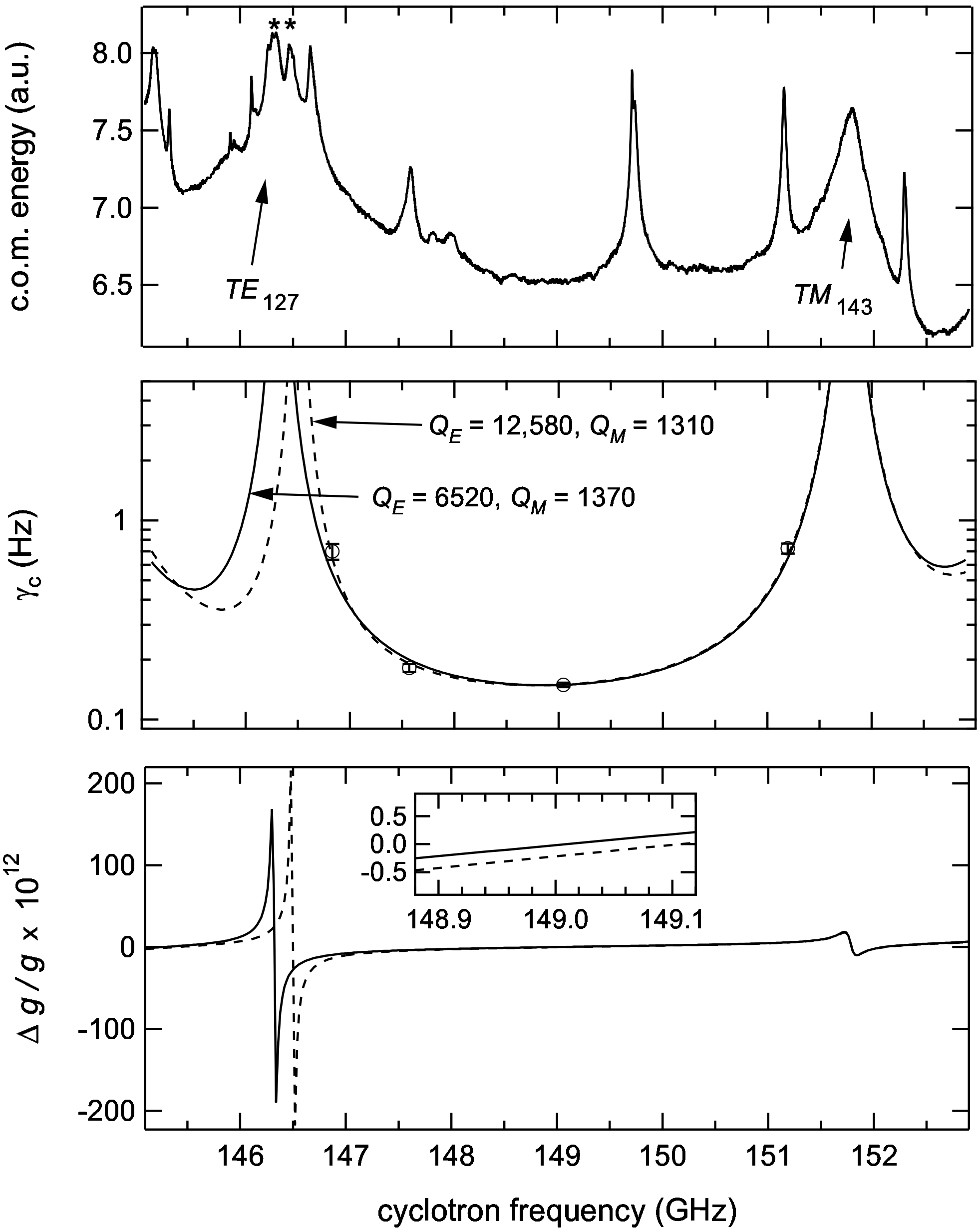

Figure 5.14: Differing choices for the frequency assignment of TE_{127}. Upper: parametric mode map in the region of the g value measurements. The two candidate peaks for TE_{127} are marked with asterisks. Middle: best fits to the lifetime data made by varying Q_E and Q_M and holding trap dimensions fixed. The solid (dashed) line show predictions for the trap dimensions corresponding to the left (right) asterisk. Bottom: predicted g value shift for the same parameters. The inset of the bottom plot, which has the same vertical scale as the larger plot, shows the region of the 149.0 GHz g value measurement.

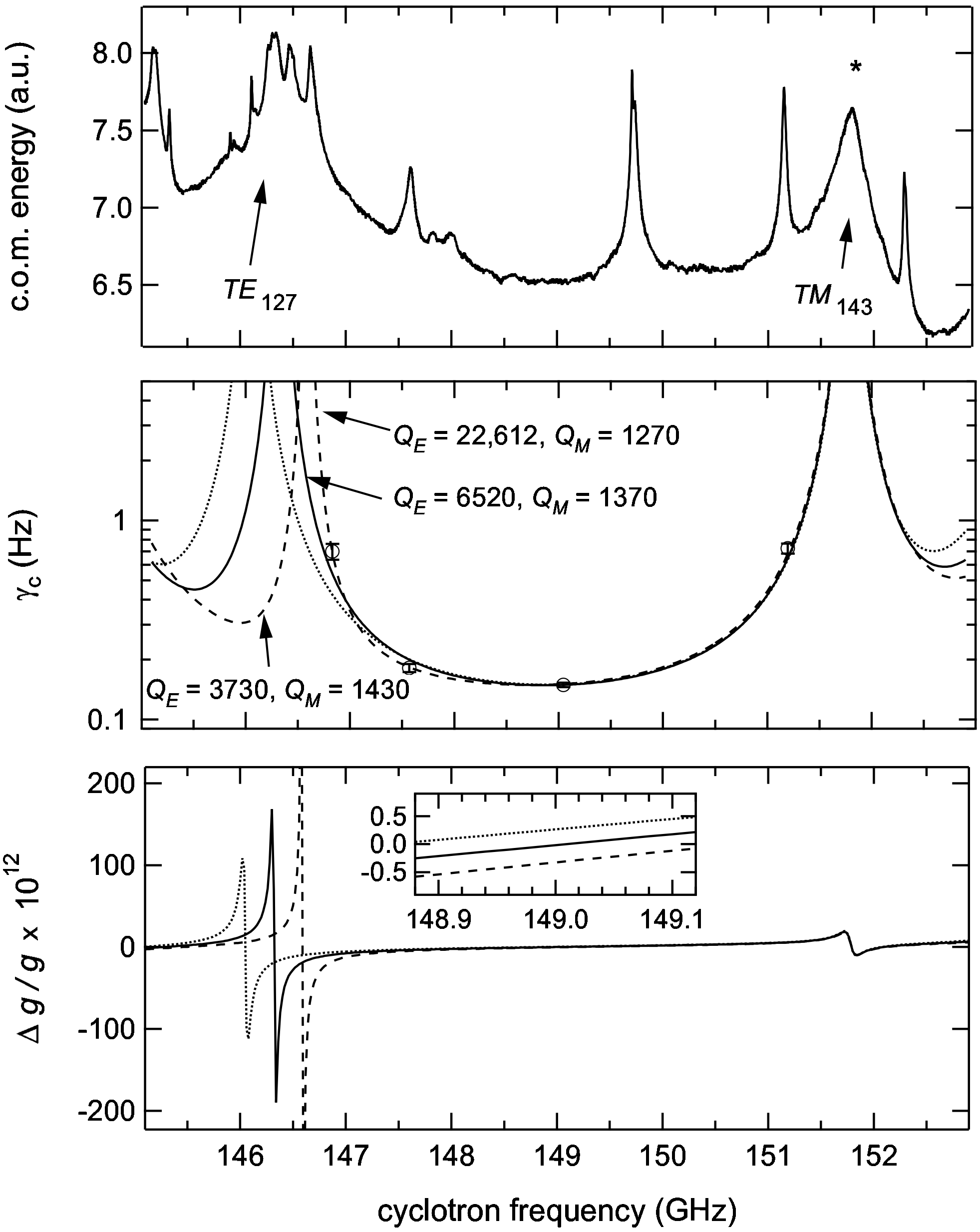

Figure 5.15: Variation of the frequency assignment of TE_{127}. Upper: parametric mode map in the region of the g value measurements. Middle: best fits to the lifetime data made by varying Q_E and Q_M and holding trap dimensions fixed. The solid line corresponds the best fit with the trap dimensions fixed at the favored frequency assignments from Table 5.3. The dotted (dashed) line shows best-Q-fit results for trap dimensions corresponding to the same frequency for TM_{143} (set at the asterisk) while the frequency of TE_{127} is decreased (increased) by 0.27 GHz. Bottom: predicted g value shift for the same sets of parameters.

parameter	left peak	middle peak	lower limit	upper limit
ρ_0 (inches)	0.17839	0.17844	0.17832	0.17846
z_0 (inches)	0.15286	0.15263	0.15320	0.15252
Q_E	6520	12,580	3730	22,610
Q_M	1370	1310	1430	1270

Table 5.3: Trap dimensions and best-fit Q_E and Q_M for various fits to the lifetime data. Values for "left (right) peak" correspond to the fit for the left (right) asterisk of Fig. 5.14. Values for "lower (upper) limit" correspond to the fit for the dotted (dashed) curve of Fig. 5.15. The "left peak" parameters are the favored values and are used for the final g value analysis.

Because of the broad pedestal at TE_{127}, there is also some question as to whether either of the candidate peaks of Fig. 5.14 actually correspond to TE_{127}, or whether it might be buried in the middle, or near an edge, of the pedestal. The lifetime data can be used to help constrain the location of TE_{127} within the pedestal, as shown in Fig. 5.15. In this figure, best fits for Q_E and Q_M are performed using trap dimensions which hold the frequency of TM_{143} fixed but vary the assignment of TE_{127} by ± 0.27 GHz (see Sec. 5.4.1 for details on this choice of frequency variation). The fit for the dotted curve shows poor agreement with the lifetime data, and the fit for the dashed curve yields an unreasonably high value for Q_E, as shown in Table 5.3. Thus, the lifetime data constrain the frequency of TE_{127} to be within ± 0.27 GHz of the favored value (but see Sec. 5.4.2 for further discussion).

5.4 Cavity-Shift Uncertainty in the g Value

Two g value measurements, at different values of magnetic field, are presented in Ch. 6. The first measurement, with $\omega_c = (2\pi)\,146.8321$ GHz, was performed quite near to cavity mode TE_{127}, and the associated cavity shift is large. The second measurement, at $\omega_c = (2\pi)\,149.0464$ GHz, is near the zero-crossing of the cavity shift between TE_{127} and TM_{143}. Calculated cavity shifts and uncertainties for these two B-field values are given in Table 5.4. The (good) agreement between the calculated and observed cavity shift is discussed in Sec. 6.2.6.

The cavity shift at each field has three sources of systematic uncertainty. First, there is error in estimation of trap dimensions due to mode frequency miscalibration. Second, there is error because slits and other trap imperfections cause shifts in the mode frequencies, which cannot be accounted for in the renormalized calculation. Finally, there is error from uncertainty in the cavity Q.

5.4.1 Mode-Frequency Error Contribution to Cavity Shifts

The first two sources of systematic error, frequency-calibration error and mode-perturbation error, can be treated together. Both types of error contribute to the 0.27 GHz rms discrepancy between measured and predicted mode frequencies described in Sec. 5.2.2.

Ideally, the g value uncertainty associated with a frequency shift of each cavity mode would be calculated independently. These g value errors would be summed in quadrature over all the modes. However, the renormalized calculation does not allow manipulation of individual mode frequencies, and the mode sum calculation is not

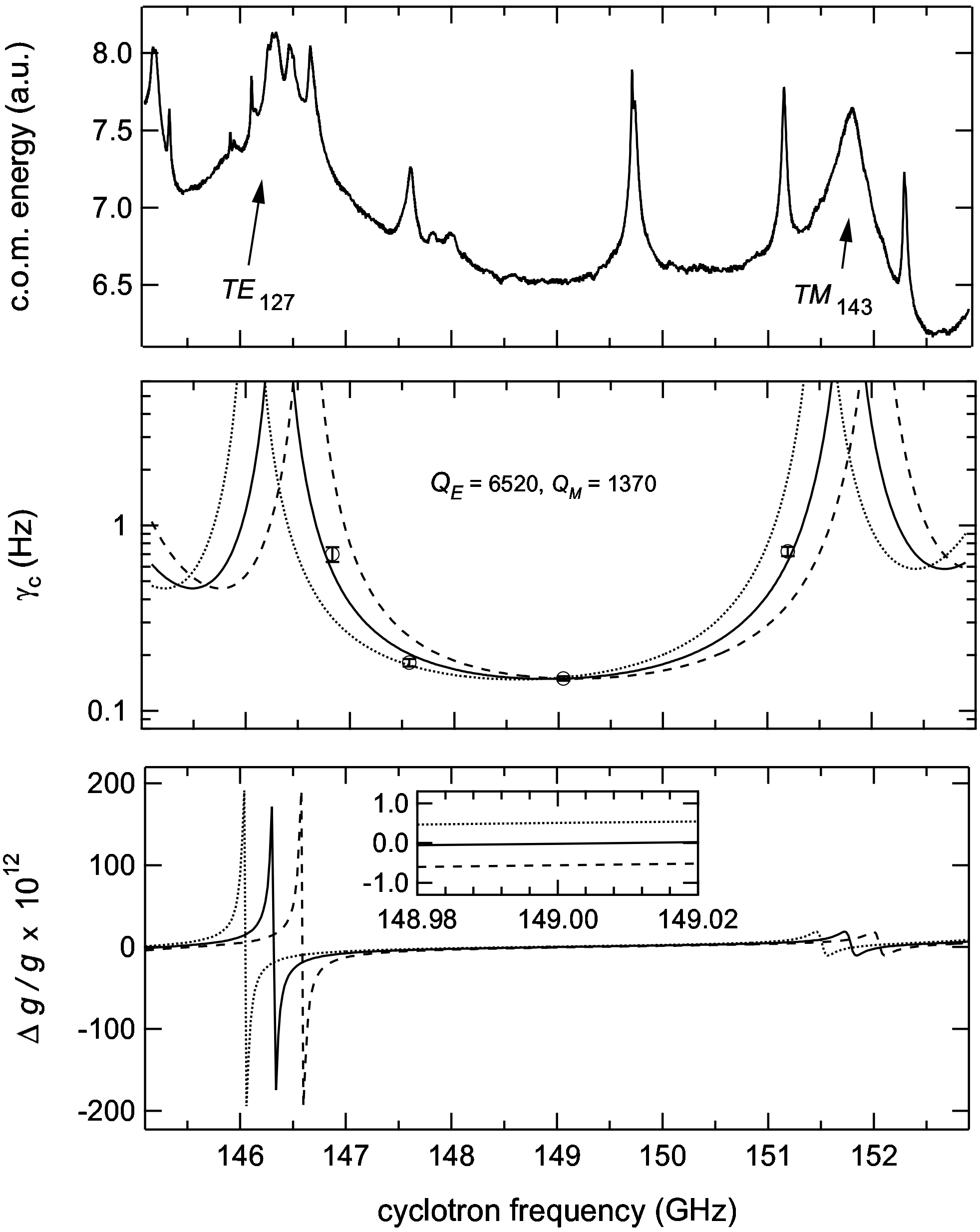

Figure 5.16: Effects of mode frequency variation across a portion of the mode spectrum. Upper: parametric mode map in the region of the g value measurements. Middle: predicted cyclotron damping rates for various trap dimensions. The solid curve gives results for the best-fit parameters from Table 5.3, and the dotted (dashed) lines shows results for trap dimensions that shift the frequencies of TE_{127} and TM_{143} down (up) by 0.27 GHz. Lower: calculated cavity shift for the same sets of trap dimensions. The inset, which has the same vertical scale as the larger plot, shows the uncertainty (at ν_c = at 149.0 GHz) associated with mode-frequency uncertainty, which is the dominant source of error in the g value measurement presented in this thesis. See Sec. 5.4.2 for a more conservative error estimate.

sufficiently accurate.

So, in order to convert frequency error from miscalibration and from mode perturbations into a g value error, a conservative approach is used. It is noted by examining Fig. 5.2 that, provided ω_c is detuned from the nearest mode by more than the mode width, a positive shift of the mode frequency creates a negative shift of the g value. This relation is true for both positive and negative detunings. Thus, if we calculate the resulting g value shift if all modes increased their frequency by a given uncertainty, we have calculated an uncertainty significantly higher than the more correct, but less practical, error estimate discussed in the previous paragraph.

ν_c (GHz)	$\Delta g/g$	$d\,(\Delta g/g)\ /\ d\,\nu_c$	error from $\Delta\nu_M$	error from ΔQ_M
146.832	-10.2 ppt	19.4 ppt / GHz	5.9 ppt	0.9 ppt
149.046	0.07 ppt	1.94 ppt / GHz	0.52 ppt	0.01 ppt
146.832*	-	-	-	-
149.046*	0.07 ppt	1.94 ppt / GHz	1.0 ppt	0.02 ppt

Table 5.4: Summary of cavity shifts and uncertainties for the two B-fields where g value measurements were performed. The second column gives the calculated g value shift. The third column gives the slope of the g value shift versus frequency. The final two columns give estimates of the calculated g value error from mode-frequency uncertainty and from mode-Q uncertainty. Entries with an asterisk correspond to the conservative error estimate discussed in Sec. 5.4.2. Values for the conservative error estimate at ν_c = 146.832 GHz are not given because the detuning of ν_c from the frequency of TE_{127} becomes negligible at one limit, preventing the same error analysis from being used.

.

This conservative error estimate is used to establish a cavity shift uncertainty from mode-frequency errors. Although not shown in Table 5.4, the g value shift incurred if all the modes shift up or down by 0.27 GHz is actually asymmetric; the error estimates given in the table are the averages of the upper and lower uncertainty intervals. The correct asymmetric error intervals are shown in Fig. 6.7.

5.4.2 A Conservative Mode-Frequency Error Estimate

At present, some of the researchers would prefer confirming data at other magnetic fields before concluding that the data in Fig. 5.15 establish the frequency of TE_{127} to be within $\pm\,0.27$ GHz of the favored value. The more conservative approach is to assign a mode-frequency uncertainty of $\pm\,0.5$ GHz, which corresponds to the half-width of the pedestal at TE_{127}.

This more conservative error estimate results in approximately twice the g value uncertainty from mode-frequency error at $\nu_c = 149.0$ GHz ($\Delta g/g \approx 0.5$ ppt $\rightarrow$ $\Delta g/g \approx 1$ ppt). Also, this approach sends the upper-frequency limit for TE_{127} to 146.8 GHz, making the uncertainty in the $\nu_c = 146.832$ GHz g value measurement very large. Results for the conservative error estimate are marked with an asterisk in Table 5.4. The conservative mode-frequency error estimate described in this section is not used in subsequent analysis. However, the final choice of error assignment is still being discussed within the research group and may be revised before publication.

5.4.3 Q-Error Contribution to Cavity Shifts

Finally, the uncertainty in cavity Q is estimated based on the measured cyclotron lifetimes, discussed in Sec. 5.3. As discussed in Sec. 5.3.2, estimates of Q from parametric mode maps yield incorrect results, and insufficient cyclotron lifetime data have been collected to reliably fit Q_E and Q_M. A conservative lower limit for cavity Q is made by taking the lowest possible value from a naive interpretation of parametric mode maps (see Sec. 5.2.5). A conservative upper estimate of cavity Q is made by assigning all Q values to a (somewhat arbitrary) factor of 1.5 times the favored Q_E value from Table 5.3. The results of these Q variations are shown in Fig. 5.17.

The inset of Fig. 5.17 shows the same conclusion as reached in Sec. 5.1.6–knowledge of cavity Q is of minimal importance for calculating the g value shift. The effects of cavity Q uncertainty on g value error, conservatively estimated as described above, are listed in Table 5.4.

5.5 Implications of Q Uncertainties

As discussed in Sec. 5.4.3, precise knowledge of the cavity Q values is not important at the current level of g value accuracy, provided the g value measurement is performed at sufficient detuning from the nearest cavity mode. However, the implications of the failure of our parametric mode maps to measure the true cavity Q (see Sec. 5.2.5), are important. If precise knowledge of mode Q is required, care must be taken when using a cloud of electrons to measure Q values, that the results are independent of cloud size. In the work presented here, this was not possible since saturation behavior was encountered before the cloud size could be sufficiently reduced.

Measurements of mode Qs in hyperbolic traps [92] have been cited to justify uncertainties assigned to the 1987 University of Washington g value measurement [2], where the proximity of the cyclotron frequency to coupled cavity modes was not known. This approach essentially uses the measured cyclotron damping rate along

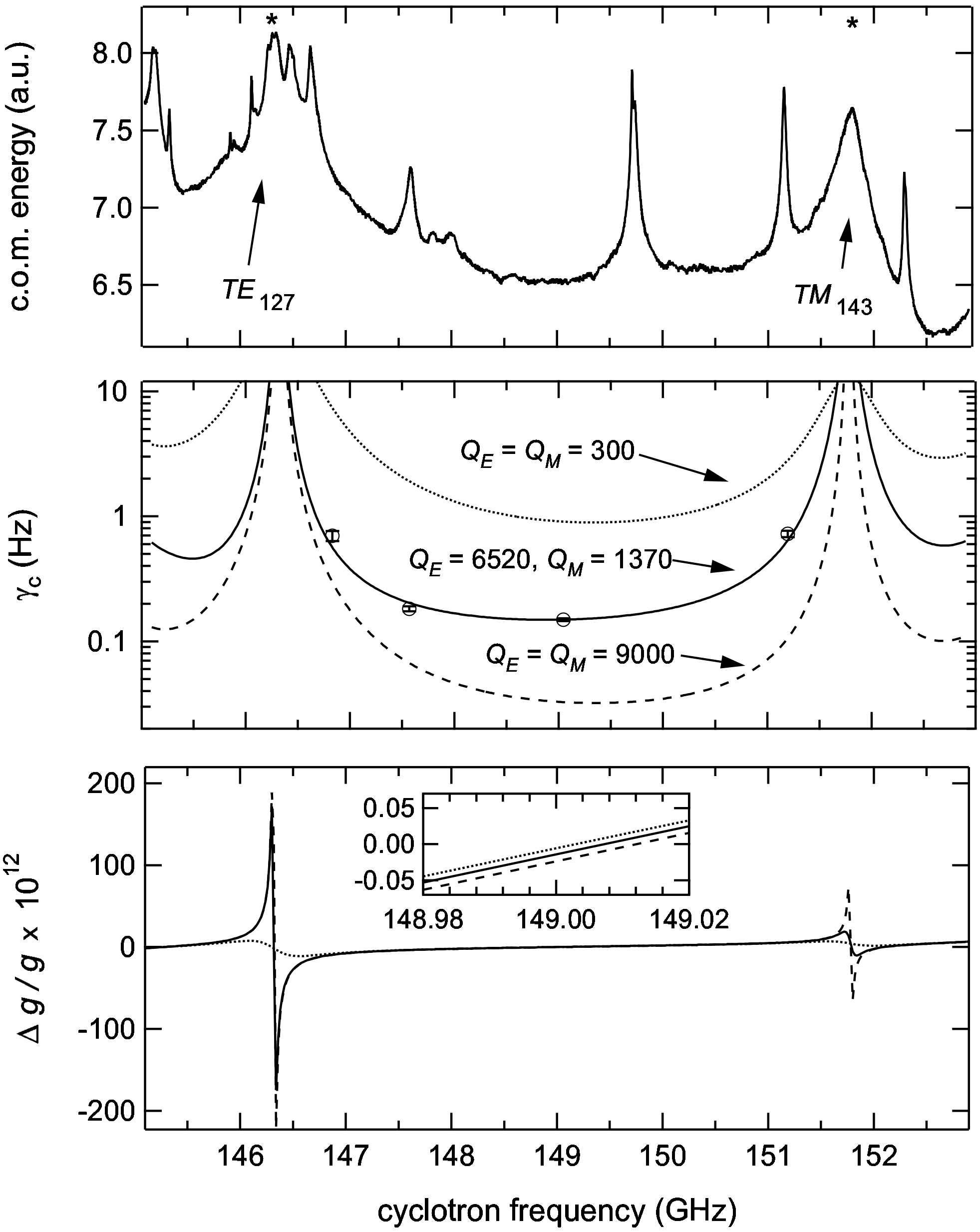

Figure 5.17: Effects of Q variation across a portion of the mode spectrum. Upper: parametric mode map in the region of the g value measurements. Middle: cyclotron damping rates for various Q values, using the favored trap dimensions of Table 5.3, which yield mode frequencies marked with asterisks in the upper plot. The solid line shows results for best fit to the lifetime data: $Q_E = 6520$, $Q_M = 1370$. The dashed (dotted) line shows results for $Q_E = Q_M = 9000$ ($Q_E = Q_M = 300$). Lower: calculated g value cavity shift for the same sets of Q values. The inset, which has the same vertical scale as the larger graph, shows that the effects of Q variation over this very large range of Qs has a negligible effect on the g value at 149.0 GHz.

with Q to estimate cyclotron frequency detuning from the nearest cavity mode. The cavity shift of the g value is then estimated based on that detuning. It is easy to show from Eqs. (5.3) and (5.4) that the estimate of cavity shift obtained by this method is proportional to the value used for Q. Thus, estimates of cavity shift require an accurate determination of cavity Q. The study of cavity Q in the hyperbolic trap used large electron clouds to measure the mode Qs but did not report that measured Qs were found to be independent of cloud size, leaving it unclear whether the difficulties discussed above with using electron clouds to measure cavity Q had been considered.

The technique used to estimate cavity shift in the hyperbolic trap experiment, discussed above, is contrasted with the technique used in this work. We obtain the detuning by comparing the cyclotron frequency to a known cavity mode spectrum. We only use the Q values in the final calculation of cavity shift, where they turn out to be unimportant. As shown in Sec. 5.1.6 and 5.4.3, this technique makes our g value measurement insensitive to a cavity Q over a very large range of values.

Chapter 6

Determination of the g value

In this chapter we present a result for the first fully quantum measurement of the electron magnetic moment. This result also represents the first demonstration of g value cavity shifts and the first comparison with predicted shifts based on an independently measured and identified cavity mode spectrum. The g value measurement presented here, with a preliminary uncertainty assignment of 0.6 parts per trillion (ppt), is a factor of 7 more accurate than the best previous results [2, 8].

6.1 Measurement of the g value

The electron's intrinsic g value is defined by the relation between its magnetic moment $\vec{\mu}$ and its spin angular momentum $\vec{S}$:

$$\vec{\mu} = g \frac{q\hbar}{2m} \frac{\vec{S}}{\hbar} \,, \tag{6.1}$$

where $q = -e$ is the electron charge and the quantity $e\hbar/2m$ is recognized as the Bohr magneton μ_B. As discussed in Sec. 1.2.1, all recent g value measurements [8] achieve a 10^3 increase in precision by directly measuring the quantity g - 2 rather than g.

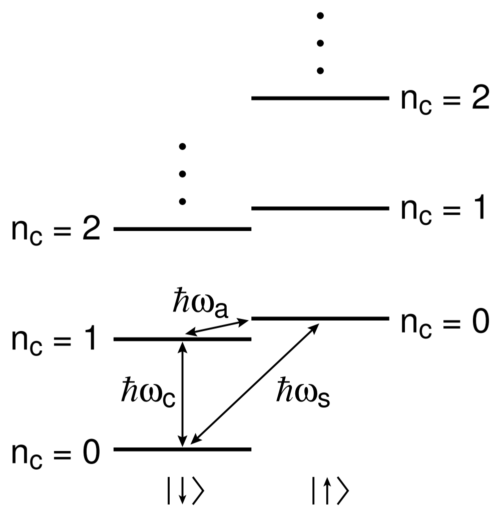

Figure 6.1: Diagram of quantized spin and cyclotron energies of an electron in a magnetic field. The effects of special relativity and of the electrostatic trapping potential are not included here. For $B = 5.5$ T, $\nu_s \approx \nu_c = \omega_c/(2\pi) \approx 150$ GHz, and $\nu_a = \omega_a/(2\pi) \approx 170$ MHz.

A quantum level diagram of spin and cyclotron motions for an electron in a magnetic field (neglecting small corrections from the electric field and from special relativity) is shown in Fig. 6.1. As discussed in the following sections, the observed eigenfrequencies in the Penning trap, $\bar{\omega}_c$, $\bar{\omega}_a$, and $\bar{\omega}_z$, are slightly modified from the corresponding free-space values ω_c, ω_a, and ω_z because of the electrostatic trapping potential. Corrections for the effects of special relativity are discussed in Sec. 6.2.1.

6.1.1 g Value Measurement in a Pure B-Field

It is easy to show that in the absence of an electric field, the ratio of anomaly to cyclotron frequencies is proportional to $g - 2$. The energy change ΔE associated with a spin-flip transition is given by

$$\Delta E = \hbar\omega_s = g\frac{e\hbar}{2m}B, \tag{6.2}$$

where ω_s is the spin-flip frequency, m is the electron mass, and where we have used the definition of g from Eq. (6.1). Using $\omega_c = eB/m$ and Eq. (6.2), we arrive at

$$\frac{g}{2} = \frac{\omega_s}{\omega_c} = 1 + \frac{\omega_a}{\omega_c} \tag{6.3}$$

where the anomaly frequency ω_a is defined as $\omega_a \equiv \omega_s - \omega_c$. An anomaly transition, shown in Fig. 6.1, is a two-photon transition involving both a spin flip and a cyclotron jump. Eq. (6.3) is often expressed in terms of the "electron anomaly" $a_e \equiv (g - 2)/2 = \omega_a/\omega_c$. Thus, without including perturbations from the electrostatic fields of the Penning trap, g - 2 is determined by measurement of the anomaly to cyclotron frequency ratio.

Although one would not choose to measure the g value by driving a direct spin-flip at ω_s, there is some theoretical interest in studying the interaction of this resonance with the electromagnetic modes of the trap cavity [90, 89]. However, it is difficult to generate a microwave field at the spin-flip frequency $\omega_s/2\pi \approx 150$ GHz strong enough to drive this transition directly; in fact, a direct spin-flip transition has not yet been observed in a Penning trap.

6.1.2 g Value Measurement in an Ideal Penning Trap

The presence of the electric field in an ideal Penning trap causes the eigenfrequency ω_c' corresponding to cyclotron motion to be slightly different from its free-space value

ω_c:

$$\omega_c' = \omega_c - \omega_m. \tag{6.4}$$

The magnetron frequency ω_m is given by

$$\omega_m = \frac{\omega_z^2}{2\omega_c'}\,, \tag{6.5}$$

where ω_z is the axial frequency. The spin frequency is not affected by the electrostatic trapping potential, so

$$\omega_a' = \omega_s - \omega_c'. \tag{6.6}$$

Combination of Eqs. (6.3), (6.4) and (6.6) yields g in terms of the eigenfrequencies of an ideal Penning trap:

$$\frac{g}{2} = 1 + \frac{\omega_a' - \omega_z^2/2\omega_c'}{\omega_c' + \omega_z^2/2\omega_c'}. \tag{6.7}$$

6.1.3 g Value Measurement in an Imperfect Penning Trap

Real Penning traps have a variety of imperfections, including misalignment of trap electrodes with respect to the B-field, misalignment of electrodes with respect to one another, and imperfections in electrode geometry. These imperfections cause the measured eigenfrequencies $\bar{\omega}_c$, $\bar{\omega}_a$, $\bar{\omega}_m$, $\bar{\omega}_z$ to differ from their corresponding values in an ideal Penning trap. For the leading-order corrections to the electrostatic potential (those that alter the quadratic terms) an invariance theorem [94] allows g to be determined precisely from the observed eigenfrequencies:

$$\frac{g}{2} = 1 + \frac{\bar{\omega}_a - \bar{\omega}_z^2/2\bar{\omega}_c}{\bar{\omega}_c + \bar{\omega}_z^2/2\bar{\omega}_c}. \tag{6.8}$$

Thus the invariance theorem conveniently allows a simple expression to be used to calculate g from the eigenfrequencies of an imperfect trap. It is not clear *a priori* that the expression in terms of the imperfect-trap eigenfrequencies, Eq. (6.8), would have the same form as Eq. (6.7), which expresses g in terms of the eigenfrequencies of an ideal trap. As verified in Sec. 6.2.7, the imperfections of the trap used in this work are sufficiently small to allow use of Eq. (6.8).

6.2 Corrections and Systematic Uncertainties

There are a few corrections and several sources of systematic uncertainty involved in using Eq. (6.8) to obtain a g value from measured frequencies. All significant corrections and sources of systematic error are collected in Table 6.2 of Sec. 6.3.

6.2.1 Relativistic Shift

The simple harmonic-oscillator level diagram shown in Fig. 6.1 does not include the effects of special relativity. As the cyclotron oscillator gains energy, its dynamics are modified by special relativity, making the oscillator slightly anharmonic. Amazingly, the accuracy of the current experiment is such that accounting for the relativistic mass increase associated with quantum *zero-point* energy is an essential correction to g, at the level of 0.6 ppt. For the choice of spin ladder used in this work (spin up), the relativistic mass increase of a spin flip requires a further 1.2 ppt correction.

The relativistic cyclotron frequency ω_c is given by

$$\omega_c = \frac{eB}{\gamma m}\,, \tag{6.9}$$

γ is the familiar relativistic correction factor. For small excitation energies $E_n \ll mc^2$, we can expand Eq. (6.9) as

$$\omega_c = \frac{eB}{m + E_n/c^2} \approx \omega_0 \left(1 - \frac{E_n}{mc^2}\right) , \tag{6.10}$$

where ω_0 is the classical cyclotron frequency.

For a harmonic cyclotron oscillator, the energy E_n of the nth quantum state is given by

$$E_n = \left(n + \frac{1}{2}\right) \hbar\omega_c \,. \tag{6.11}$$

The change δ in cyclotron frequency per energy quantum can then be approximated by using the level spacing of the harmonic oscillator:

$$\delta \approx \frac{d\omega_c}{dn} = -\frac{\omega_0}{mc^2}\frac{dE_n}{dn} \approx -\omega_c\frac{\hbar\omega_c}{mc^2} \,. \tag{6.12}$$

A fully quantum calculation [69] yields the exact result $\delta = -\hbar\omega_c^2/mc^2$, which matches the approximate result of Eq. (6.12). For the level of accuracy of this work, we also need to know the zero-point and spin contributions to the frequency shifts. The results of the fully quantum calculation [69], including these contributions, is shown in Fig. 6.2.

For $\nu_c = 150$ GHz, $\delta/(2\pi) = 182$ Hz. This shift corresponds to a 1.8 ppb cyclotron frequency shift for the interval $|s = \uparrow, n_c = 0\rangle \rightarrow |s = \uparrow, n_c = 1\rangle$, where all cyclotron spectroscopy in the Harvard 2004 experiment is performed. The measured cyclotron frequency $\bar{\omega}_c\,(|\uparrow, 0\rangle \rightarrow |\uparrow, 1\rangle)$ must be converted to the zero-energy cyclotron frequency $\bar{\omega}_c$ (which does not correspond to a measurable interval) by using

$$\bar{\omega}_c = \bar{\omega}_c\,(|\uparrow, 0\rangle \rightarrow |\uparrow, 1\rangle) + \left(\frac{3}{2}\right)\delta. \tag{6.13}$$

The value of $\bar{\omega}_c$ obtained from Eq. (6.13) is then used in Eq. (6.8) to compute the g value.

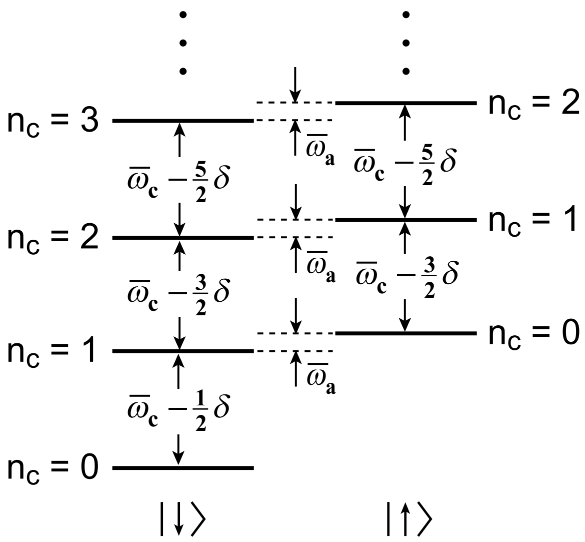

Figure 6.2: Spin and cyclotron energy levels including relativistic shifts. For a magnetic field of 5.4 Tesla, $\delta/(2\pi) = 1.2$ ppb.

The significant contribution of the relativistic correction term δ, corresponding to $\Delta g/g = 1.4 \times 10^{-12}$ per quantum level, illustrates one of the important advantages of the novel single-quantum cyclotron spectroscopy used in this experiment. If the cyclotron frequency is measured using classical spectroscopy, as in previous experiments [2, 54], there will be a distribution of occupied cyclotron states. The resulting frequency shift is by no means trivial to calculate, and it depends on both cyclotron temperature and drive strength. Errors in previous 4.2 Kelvin g value experiments introduced by thermal excitation to $|n_c = 1\rangle$ and by the relativistic shift might have been as large as $\Delta g/g \approx 1 \times 10^{-12}$ [51, 52]. Single-quantum spectroscopy between known states completely eliminates the uncertainty from relativistic effects.

6.2.2 Axial Shift from Anharmonicity

The axial frequency ν_z enters into the g value measurement as a correction to ν_a and ν_c. From Eq. (6.8), it can be shown that the error $\Delta g/g$ induced by an axial frequency error $\Delta\nu_z$ is given by

$$\frac{\Delta g}{g} \approx -\frac{\bar{\nu}_z}{\bar{\nu}_c^2}\Delta\bar{\nu}_z = -9 \times 10^{-15}\Delta\bar{\nu}_z, \tag{6.14}$$

where the last equality is for $\bar{\nu}_c = 150$ GHz and $\bar{\nu}_z$ is expressed in Hz. In principle, errors in $\Delta g/g$ from axial frequency shifts can be made negligible, but this requires some care to guarantee that the correct value for $\bar{\nu}_z$ has been measured.

As discussed in Sec. 2.3.4, the axial frequency is shifted by the large excitation of the self-excited oscillator (SEO) due to axial anharmonicity. However, cyclotron and anomaly measurements are made after the amplifiers have been shut off and the axial oscillator has cooled to ~ 300 mK (see Sec. 4.3). So the axial frequency at $T_z = 300$ mK, and not while the oscillator is self-excited, must be used in Eq. (6.8). The cold T_z conditions can be approached by measuring the axial frequency when feedback is shut off and the electron is driven only by the thermal noise of the amplifiers (in our case ~ 5 K). The electron resonance is observed as a dip in the amplifier noise resonance [69]. The shift in $\bar{\nu}_z$ between the dip frequency and the SEO-driven value is between +10 to +40 Hz (out of $\nu_z = 200$ MHz) for usable SEO gain settings. This range would correspond to an error of $0.09 \times 10^{-12} \leq \frac{\Delta g}{g} \leq 0.4 \times 10^{-12}$, if the SEO value for $\bar{\nu}_z$ instead of the non-driven value were mistakenly used in Eq. (6.8).

The dip in the noise spectrum still suffers from the broadening associated with a thermal distribution of axial energies in an anharmonic potential. However, the anharmonicity-induced broadening of the dip is observed to be less than 1 Hz, which limits the further anharmonicity-induced shift between 5 K and 300 mK to less than 1 Hz as well. Thus, a measurement of the dip frequency suffices as a measurement of $\bar{\nu}_z$ at the 1 Hz level accuracy, corresponding to $\Delta g/g \approx 10^{-14}$.

For the final data taken at $\nu_c = 149.0$ GHz, the dip frequency was used for $\bar{\nu}_z$, so there is no corresponding correction or uncertainty. However, at $\nu_c = 146.8$ GHz, the dip frequency was not measured. As a result, an anharmonicity-induced correction of $\Delta g/g = (0.2 \pm 0.3) \times 10^{-12}$ is applied to those measurements.

One of the advantages of the SEO is that it allows axial detection to be performed at large oscillation amplitudes, where the trap is made to be locally harmonic [66]. However, this comes at the cost of making the trap locally anharmonic for the colder axial temperatures where the g value measurement is performed. In future g value measurements, the SEO might need to be operated with low gains so that the anharmonicity at the trap center is reduced. Choking down the SEO gain in this way would unfortunately reduce its advantage over conventional externally-driven axial detection. Tuning the compensation potential to different settings for detection and for g value measurement might also circumvent anharmonicity problems.

Anharmonicity of the axial frequency at low excitation energies also perturbs the anomaly and cyclotron line shapes discussed in Sec. 4.2.2. The magnetic bottle causes the resonant frequency to vary with axial energy. The cyclotron and anomaly frequencies $\bar{\nu}_c$ and $\bar{\nu}_a$ are functions of the magnetron frequency $\bar{\nu}_m = \bar{\nu}_z^2/2\bar{\nu}_c$. Thus anharmonicity of the axial frequency also causes $\bar{\nu}_c$ and $\bar{\nu}_a$ to vary with axial energy, changing the effective magnetic bottle. The effect on the g value calculation of Eq.(6.8) is much more significant in $\bar{\nu}_a$ than for $\bar{\nu}_c$, so the effective bottle shift does not cancel out. Like the the other effects discussed above, though, this is not a problem at the current level of precision.

6.2.3 Axial Frequency Shift from the Anomaly Drive

There is also a shift in the axial frequency due due to the anomaly drive, which involves two effects [86]. The first is a Paul-trap effect, where the off-resonant anomaly

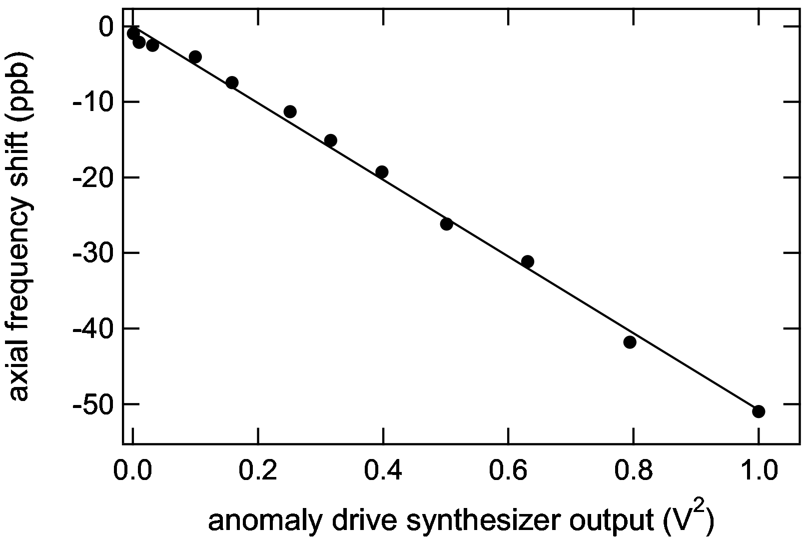

Figure 6.3: Shift of axial frequency with anomaly drive synthesizer power, for the experimental setup at $\nu_c = 149$ GHz.

drive changes the effective trap potential. The second effect is the shift of the free-oscillation frequency at ν_z as a result of forced off-resonance oscillation at ν_a. The frequency shift from both effects is expected to scale linearly with the square of the anomaly drive voltage, in good agreement with the measured shift, shown in Fig. 6.3. The axial frequency shift provides a means of calibrating the anomaly drive voltage at the trap; in further discussion, the anomaly drive power is expressed in terms of the axial frequency shift. Although the effects on a g value measurement of these axial shifts can easily be accounted for, they are negligible in the Harvard experiment since the proximity of the anomaly and axial frequencies allows a relatively weak anomaly drive to be used. The maximum anomaly drive strength used during a systematic study only caused a 4 ppb axial frequency shift, as shown in Fig. 6.4. As can be seen from Eq. (6.8), the effect on a g value measurement is negligible.

6.2.4 Anomaly Power Shifts

The anomaly transition probability dP for a short time interval dt is given [69] by

$$\frac{dP}{dt} = \frac{\pi}{2}\Omega_a^2 \chi_a(\omega), \tag{6.15}$$

where $\chi_a(\omega)$ is the anomaly response function described in Ch. 4. The rabi frequency Ω_a is given by

$$\Omega_a = B_2 z_a \rho_c \frac{\mu_B}{\hbar}, \tag{6.16}$$

where B_2 is the bottle parameter, z_a is the amplitude of the off-resonant axial oscillation at ν_a, and ρ_c is the cyclotron radius. The amplitude z_a is proportional to the anomaly drive voltage V_a. It has been shown [86] that for fixed axial and anomaly frequencies, all shifts of the anomaly resonance follow the relation

$$\frac{\Delta\nu_a}{\nu_a} \propto V_a^2, \tag{6.17}$$

where V_a^2 is the anomaly drive voltage. Combining the above equations and requiring anomaly transitions of a given rate, we find

$$\frac{\Delta\nu_a}{\nu_a} \propto \frac{1}{\chi_a(\omega) B_2^2}. \tag{6.18}$$

The response parameter $\chi_a(\omega)$ obeys

$$\chi_a(\omega) \propto \frac{1}{\Delta\omega}, \tag{6.19}$$

where $\Delta\omega \propto B_2 T_z$ is the thermal shift parameter of Sec. 4.2.2, and T_z is the axial temperature. We finally arrive at

$$\frac{\Delta\nu_a}{\nu_a} \propto \frac{T_z}{B_2}, \tag{6.20}$$

which gives the dependence of anomaly power shifts on axial temperature and bottle size for a given anomaly transition rate.

Previous g value experiments have encountered difficulties with anomaly drive systematics [54], particularly those which used a very small ($B_2 = 10$ T/m^2) magnetic bottle [86, 51, 95, 40]. According to Eq. (6.20), the fact that the Harvard bottle ($B_2 =$ 1540 T/m^2) is an order of magnitude larger than even the $B_2 =$ 150 T/m^2 magnetic bottles previously used and the temperature is over an order of magnitude smaller, we expect to observe negligible anomaly power shifts at the current level of accuracy.

A study of the anomaly drive power shift is shown in Fig. 6.4. Any anomaly drive shift is expected to be proportional to the square of the anomaly voltage V_a [86]. The power shift graph is calibrated in terms of the fractional axial frequency shift $\delta = \Delta\nu_z/\nu_z \times 10^9$ induced by the anomaly drive, which is also proportional to V_a^2 (see Sec. 6.2.3). A linear fit to the measured points shown in Fig. 6.4 yields

$$\frac{\Delta a_e}{\Delta\delta} = 0.01\ (11) \times 10^{-12}, \tag{6.21}$$

which is consistent with a vanishing power shift. The data for the reported value at $\nu_c = 149.0$ GHz were taken at an anomaly drive strength corresponding to $\delta = 1.3$.

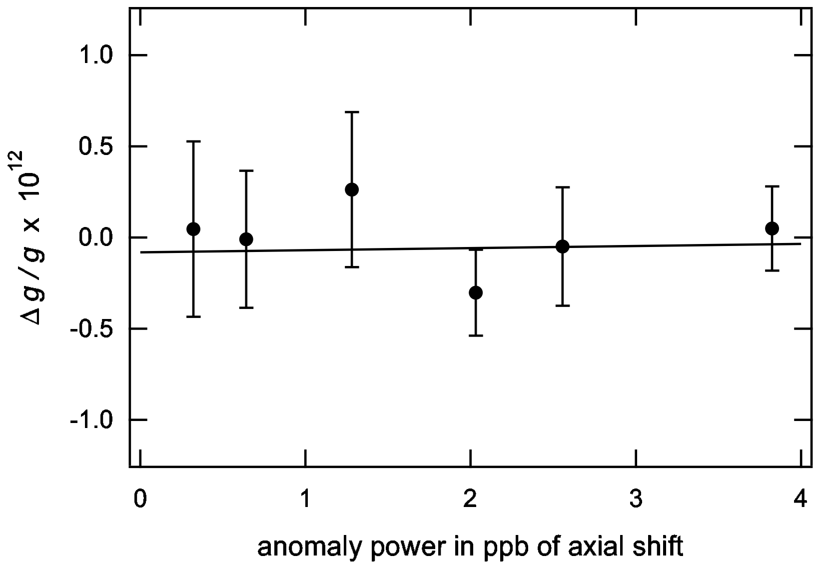

Figure 6.4: Shift of measured g value with anomaly power, measured at $\nu_c = 149.0$ GHz. Anomaly power is expressed in terms of the axial shift parameter δ (see Fig. 6.3). All data in this plot were taken at the same axial frequency and SEO gain setting, but only the SEO-excited axial frequency was recorded. As a result, the y-axis has a small but unknown offset which prevent these data from being used for a precise g value measurement. All data in this plot were taken with a cyclotron power of $P \approx 60$ in the units of Eq. (6.22). Only statistical errors are included in the figure and in the fit.

No offset is applied to the measured g values, but an uncertainty of 0.14×10^{-12} is obtained from Eq. (6.21).

The data used for obtaining g at $\nu_c = 146.8$ GHz are those shown in Fig. 4.7, over which the anomaly drive strength varies. However, like for the data of Fig. 6.4, no systematic shift over these data was observed. A conservative error estimate for the $\nu_c = 146.8$ GHz data is made by assigning an uncertainty corresponding to the possible shift at the highest used anomaly power: $\Delta g/g = (0 \pm 0.4) \times 10^{-12}$.

6.2.5 Cyclotron Power Shifts

Although cyclotron power shifts were observed in the 1987 University of Washington experiment at the 0.6 ppt level [2], their origin is not understood. Data obtained in a trap with a variable magnetic bottle [8] shows that the cyclotron power shifts are proportional to B_2. It might be expected that the effect of the 10 times larger bottle in the Harvard experiment would roughly cancel the effect of the ~ 10 times weaker drive allowed by the narrower line width (see Sec. 6.2.4). However, in the Harvard experiment, far less drive strength is required than is suggested by the linewidth argument because we resolve single-quantum cyclotron transitions (which have a relatively long lifetime), rather than requiring sustained excitation of several quanta (which start at a shorter lifetime and become even shorter in excited states).

In a study of cyclotron power shifts, drive strength is varied by adjusting a precision D-band microwave attenuator, so relative changes of microwave power are well calibrated. However, there is not currently a good method to calibrate the absolute microwave power which reaches the trap. Cyclotron excitation fraction under controlled conditions might be used to obtain an absolute calibration, but statistical fluctuations and magnetic field drift would make precise calibration difficult. The lack of absolute calibration is not considered to be a problem, though, since searches for shifts scaling with drive power can still be performed, even if the absolute scaling is unknown.

A study of cyclotron power shift is shown in Fig. 6.5. The x-axis is linear in drive power, where the power parameter P is given by

$$P = 10^{-A/10} * 1000, \tag{6.22}$$

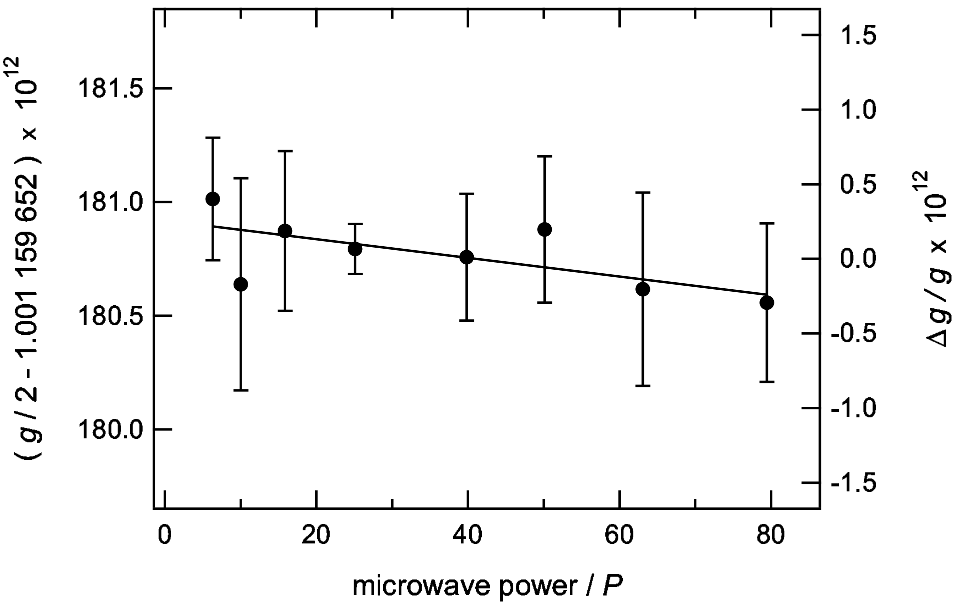

Figure 6.5: Shift of g with cyclotron drive strength, measured at $\nu_c = 149.0$ GHz. All corrections discussed in this chapter were applied to the data, but only statistical uncertainties are drawn and used for the fit. All data in this plot were taken with an anomaly drive strength corresponding to $\delta = 1.3$ (See Sec. 6.2.4). The point at $P = 25$, where final g value data was taken, represents an average over seven separate g value measurements.

where A is the D-band attenuator setting in decibels.

The fit to the data in Fig. 6.5 is given by

$$\frac{g}{2} = 1.001\ 159\ 652\ 180\ 92\ (16) - \left[4.1\ (4.7) \times 10^{-15}\right] \times P, \tag{6.23}$$

where P is microwave power in the units of Fig. 6.5. The data are consistent with a vanishing cyclotron drive power shift, so no offset to the measured g values is applied. The final data for 149.0 GHz were taken at a cyclotron drive power $P = 25$, at which power Eq. (6.23) yields an uncertainty from a possible power shift of $\Delta a_e = 0.12 \times 10^{-12}$, which is reported in Table 6.3.

Data at $\nu_c = 146.8$ GHz were taken with a different pin-hole attenuator mounted on the trap window, so the calibration of the cyclotron drive for those data relative to P is not precisely known. Comparing the cyclotron excitation fraction for histograms taken at the two different field values, it is determined that data taken at 146.8 GHz correspond to $30 \leq P \leq 60$. Therefore, a conservative error estimate is made for a possible cyclotron power shift of the $\nu_c = 146.8$ GHz by assigning an uncertainty corresponding $P = 60$ of $\Delta g/g = 0.3 \times 10^{12}$.

6.2.6 Cavity Shifts

The procedure for obtaining corrections associated with cavity shifts is described in Ch. 5. The g value measurements obtained at the two different B-field values used in this work are shown in Fig. 6.6. All corrections and uncertainties (including statistical uncertainty) discussed in this chapter, aside from those associated with cavity shifts, are included in the uncertainty intervals.

As discussed in Sec. 5.4, cavity shift uncertainty comes from two sources: mode frequency uncertainty and mode Q uncertainty. Both sources of uncertainty have a larger effect when the g value is measured near a cavity mode. Mode-frequency uncertainty is exaggerated near a cavity mode because in this region the cavity shift is changing rapidly with frequency. As discussed in Sec. 5.1.6, mode Q is insignificant if ν_c is far-detuned from the mode frequencies, and Q only has a small effect when the g value is measured near a mode. Table 6.1 shows the relative contributions to cavity shift error for the measurements at the two different field values.

Fig. 6.6 shows a comparison of g value measurements made at different B-fields along with the shift predicted by the independently measured cavity mode spectrum.

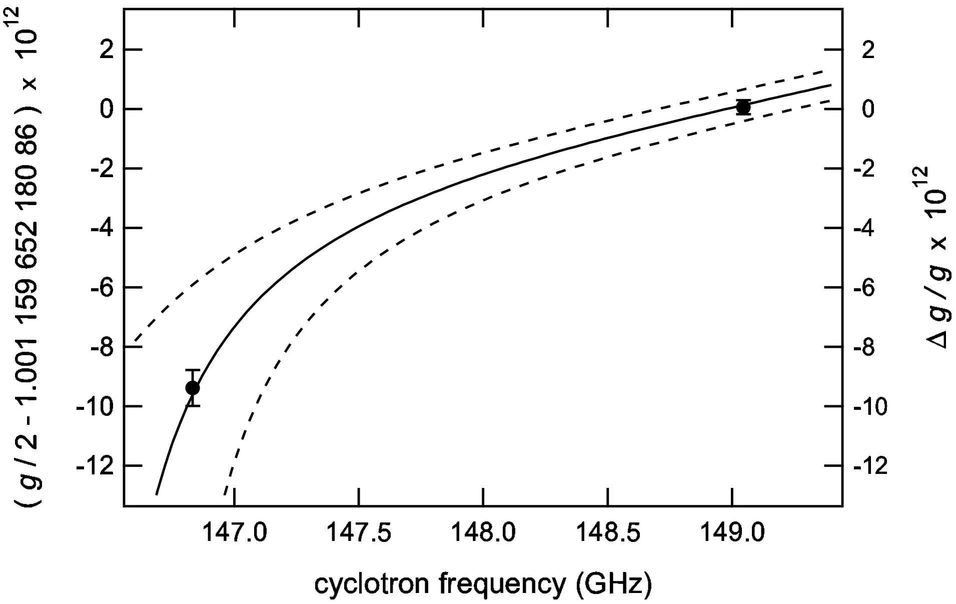

Figure 6.6: Measurements of the g value at B-fields with different cavity shifts. The lower-frequency point is near cavity mode TE_{127}, and the higher-frequency point is well-centered between TE_{127} and TM_{143}. Error bars represent all uncertainty besides those from cavity-shift corrections. The solid line represents the predicted cavity shift, with the offset in g defined by the ν_c = 149.0 GHz measurement. The dashed lines represent the estimated 68% confidence region of the cavity shift correction.

ν_c	$\lvert\nu_c - \nu_{M1}\rvert$	$\lvert\nu_c - \nu_{M2}\rvert$	calculated shift in $\Delta g/g \times 10^{12}$
146.8 GHz	0.51 (27)	4.95 (27)	-10.2 (5.9) (0.9)
149.0 GHz	2.72 (27)	2.73 (27)	0.07 (0.52) (0.01)

Table 6.1: Cavity shifts and uncertainties for g value measurements at ν_c = 146.8 GHz and at ν_c = 149.0 GHz. The second and third columns report the frequency offset (in GHz) from the nearest modes on the low and high-frequency sides, respectively. The final column reports the calculated cavity shift, where the first and second errors are estimates of the mode-frequency uncertainty and the mode-Q uncertainty, respectively. (As shown in Fig. 6.7, the upper and lower cavity shift uncertainties are actually asymmetric; the errors reported in the fourth column are the averages of the upper and lower uncertainty intervals.)

This comparison represents the first demonstration of the long-anticipated [87] cavity shifts of Penning trap g value experiments and the first comparison with predicted shifts based on an independently identified cavity mode spectrum.

It can be seen from Fig. 6.6 that the predicted cavity shift shows good agreement, to well within the uncertainty, with the measured g value shift. However, this statement still leaves open the question of whether the cavity shift model has calculated the correct *offset* for the measured g values. The cavity shift calculations inherently determine absolute shifts and not relative shifts. So, if enough relative g value comparisons are made at different fields, like the comparison shown in Fig. 6.6, the absolute offsets of the cavity shift calculation could be verified with a high degree of confidence.

6.2.7 Shifts from Trap Misalignment

Following Ref. [69], limits on trap misalignment and asymmetry can be determined by comparing the measured magnetron frequency $\bar{\nu}_m$ to the value predicted for an ideal trap $\bar{\nu}_z^2/2\bar{\nu}_c$.

Misalignment between the trap axis and the field axis is parameterized by the angles θ and ϕ, where

$$\begin{aligned} B_z &= B\cos\theta, \\ B_x &= B\sin\theta cos\phi, \\ B_y &= B\sin\theta sin\phi. \end{aligned} \tag{6.24}$$

The results of electrode internal misalignment and imperfections can be parameterized by ε, where the electrostatic potential energy U is given by

$$U = \frac{1}{2} m\omega_z^2 \left[z^2 - \frac{1}{2}\left(x^2 + y^2\right) - \frac{1}{2}\varepsilon\left(x^2 - y^2\right) \right] . \tag{6.25}$$

The observed magnetron frequency $\bar{\omega}_m$ is given by

$$\bar{\omega}_m \approx \tilde{\omega}_m \left(1 - \varepsilon^2\right)^{1/2} \left[1 - \frac{3}{2}\sin^2\theta \left(1 + \frac{1}{3}\varepsilon\cos 2\phi\right)\right]^{-3/2} , \tag{6.26}$$

where $\tilde{\omega}_m$ is defined as

$$\tilde{\omega}_m \equiv \frac{\bar{\omega}_z^2}{2\bar{\omega}_c} . \tag{6.27}$$

As discussed in Sec. 2.3.6, Eq. 6.26 along with measurement of $\bar{\omega}_m$ and $\bar{\omega}_c$ can be used to estimate the size of imperfections in the experimental trap. The observation of $\bar{\omega}_m > \tilde{\omega}_m$ in the traps described in this work and elsewhere [96, 97] is consistent with Eq. 6.26 and the expectation that for experimental traps $\theta > \varepsilon$ [69]. Thus, Eq. 6.26 is used as an estimate of θ, assuming a small ε, in this work. Using this assumption and the measurement of $\bar{\omega}_m$ described in Sec. 2.3.6, we conclude $\theta < 0.5°$.

For $\theta \ll 1$ and $\varepsilon \ll 1$,

$$\frac{\omega}{\bar{\omega}_c} = 1 + \frac{1}{2}\left[\frac{\bar{\omega}_z}{\bar{\omega}_c}\right]^2 + \frac{9}{16}\left[\frac{\bar{\omega}_z}{\bar{\omega}_c}\right]^4 \left(\theta^2 - \frac{2}{9}\varepsilon^2\right) \tag{6.28}$$

gives the error introduced in $\bar{\omega}_c$ by trap imperfections. For angular misalignment of $\theta = 1°$, the fractional error in ω_c given by Eq. (6.28) is on the order of 10^{-18}. Therefore, the invariance theorem of Eq. (6.8), can be used to accurately determine g from the measured eigenfrequencies.

6.3 g Value Measurement Results

All known corrections and systematic uncertainties are listed in Table 6.2. The largest uncertainties come from cavity shift corrections. Table 6.3 shows the final g value measurements with all corrections and uncertainties included. After including corrections for the cavity shift, the agreement between the values obtained at the different fields is quite good. The results are also plotted in Fig. 6.7.

source	$\Delta g/g \times 10^{12}$ at 146.8 GHz	$\Delta g/g \times 10^{12}$ at 149.0 GHz
relativistic $\Delta\nu_c$	– 2.07 (0.00)	– 2.10 (0.00)
misalignment	0.00 (0.00)	0.00 (0.00)
ν_z anharmonicity	0.2 (0.3)	0.00 (0.02)
anomaly power	0.0 (0.4)	0.00 (0.14)
cyclotron power	0.0 (0.3)	0.00 (0.12)
cavity shift	10.2 (6.0)	−0.07 (0.52)
total corrections	**8.3 (6.0)**	**-2.17 (0.55)**

Table 6.2: Systematic corrections and uncertainties in obtaining the g value from measured frequencies for the two different B-field values. Non-parenthesized items represent corrections applied to obtain the correct value for g, and parenthesized items represent uncertainties.

Since the uncertainties of the cavity shift calculation are already included in the 0.6 ppt standard error of the 149.0 GHz measurement, the larger uncertainty at 146.8 GHz should not be regarded as degrading the accuracy. These results can be interpreted as a 0.6 ppt g value measurement at 149.0 GHz, where the cyclotron frequency is far detuned from the nearest cavity mode, and an independent confirmation of the cavity

ν_c	$g/2$ without cavity corrections	$g/2$ with cavity corrections
146.8 GHz	1.001 159 652 171 48 (12) (58)	1.001 159 652 181 68 (12) (600)
149.0 GHz	1.001 159 652 180 93 (15) (19)	1.001 159 652 180 86 (15) (55)
wtd. mean		1.001 159 652 180 87 (57)

Table 6.3: Final results for g value measurements at the two different B-field values. In the first two rows, the first parenthesized quantity is the statistical uncertainty and the second is the systematic uncertainty. Only the overall uncertainty is given for the weighted mean. See Sec. 5.4.2 for discussion on the assigned uncertainty.

shift calculation, made by comparison with the 146.8 GHz result, where the cyclotron frequency is strongly affected by the nearby mode. Alternatively, a weighted mean of the two measurements can be performed; the result is also shown in Table 6.3.

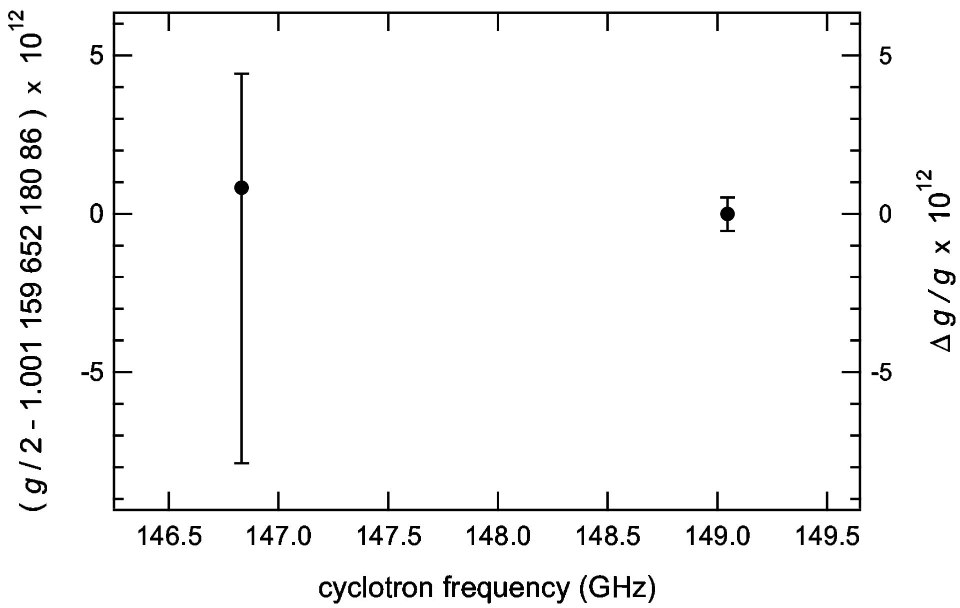

Figure 6.7: g value measurement at ν_c = 146.8 GHz and at ν_c = 149.0 GHz. All known corrections and sources of uncertainty, both statistical and systematic, are included.

Chapter 7

Conclusion

We have presented a preliminary result for the first fully quantum measurement of the electron magnetic moment. This result, with an uncertainty of 0.6 parts per trillion (ppt), is a factor of 7 more accurate than the best previous g value measurements [2, 8]. The result is regarded as preliminary since we are currently preparing to take g value measurements at a few more values of magnetic field and since the assigned error might be revised before publication (see Sec. 5.4.2). In this chapter, we review the status of the measurement. We also discuss prospects for future experiments.

7.1 Harvard g value Measurement

The g value result from this thesis, presented in Ch. 6, is

$$\frac{g}{2} = 1.001\ 159\ 652\ 180\ 86\ (57). \tag{7.1}$$

The 0.6 ppt uncertainty is dominated by the cavity shift systematic. As discussed in Sec. 1.1.2, this g value is used along with existing QED calculations [12, 4, 6] to determine a new value for the fine structure constant

$$\alpha^{-1} = 137.035\ 999\ 777\ (27)\ (67), \tag{7.2}$$

where the first uncertainty is from theory and the second is from experiment.

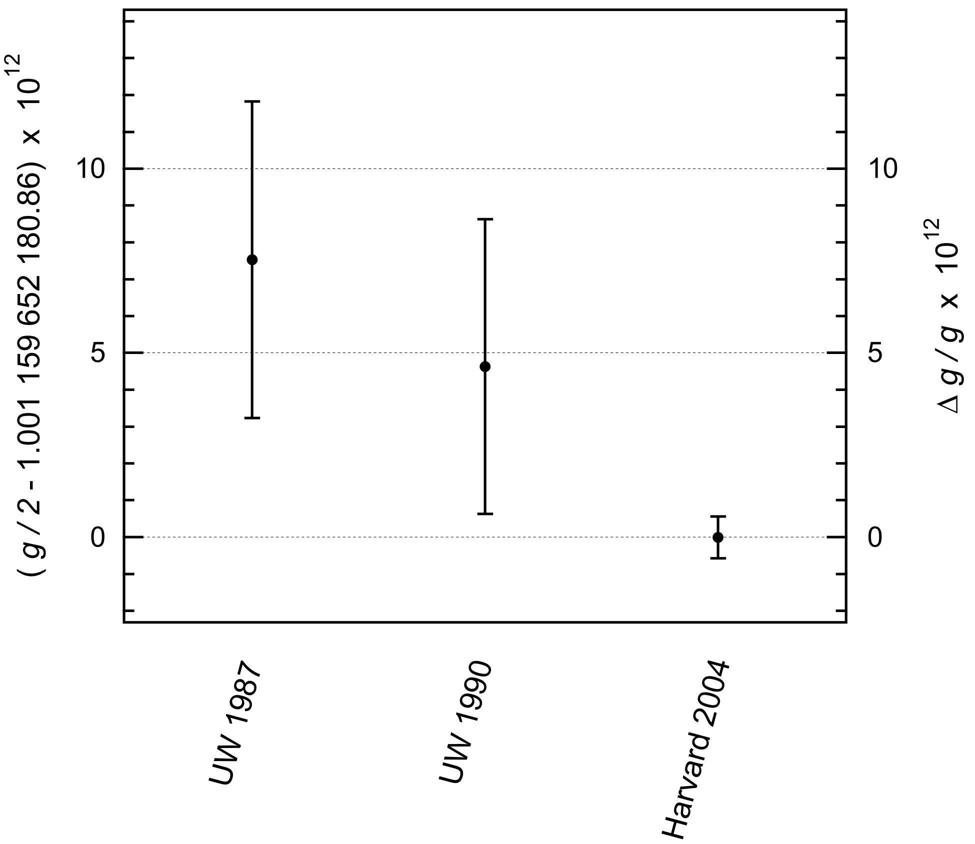

Figure 7.1: Comparison of recent g value measurements. The zero of vertical axes is set to the Harvard 2004 result presented in this thesis. "UW" denotes experiments [2, 8] performed at the University of Washington.

Agreement of the Harvard determination of α with other measurements is shown in Fig. 1.2. A comparison of the Harvard g value result with recent measurements from the University of Washington (see Sec. 1.3), is shown in Fig. 7.1. The difference between the Harvard result and the 1987 University Washington result [2], approaches a $2\,\sigma$ disagreement. This rather large disagreement is perhaps not surprising considering the lack of knowledge of the hyperbolic trap cavity modes which lead to the reported 4.3 ppt uncertainty of the 1987 measurement (see Sec. 5.5). Agreement between the Harvard result and the 1990 University of Washington result [8], where a lossy hyperbolic trap was used to reduce cavity shifts, is reasonable.

7.2 Strengths of the Harvard g value Measurement

The g value measurement presented here uses quantum spectroscopy (see Ch. 4) between only ground and first-excited states of the spin and cyclotron motions. Representing a marked improvement over the classical cyclotron spectroscopy of previous experiments [54], this procedure completely eliminates frequency-shift uncertainties associated with relativistic mass corrections of excited states.

Single quantum spectroscopy is possible because the apparatus is cooled by a dilution refrigerator, causing only the ground cyclotron state to be occupied. Also, the sub-Kelvin environment cools the axial motion, reducing thermal broadening of the cyclotron and anomaly resonances (see Ch. 4) while still allowing resolution of single-quantum cyclotron jumps. The use of a higher axial frequency [70] has a similar effect. Cooling of the axial temperature and the use of single-quantum cyclotron spectroscopy also reduce drive-power systematic shifts (see Ch. 6).

Finally, the Harvard g value measurement is performed in a cylindrical Penning trap [73], as contrasted with the hyperbolic traps used in previous g value experiments [8]. The electromagnetic standing-wave modes of the cylindrical trap cavity are identified as well characterized TE and TM modes. The low mode density and precise mode characterization (see Ch. 5) afforded by a cylindrical trap allows the cyclotron frequency to be far detuned from independently identified cavity mode frequencies. The frequency shift from residual interaction with cavity modes can be calculated to a high degree of accuracy.

7.3 Future g value Experiments

The leading uncertainty of this g value measurement is associated with an imprecise knowledge of cavity mode frequencies (see Ch.5). Although we were largely limited by equipment problems, it is also unclear why we were unable to use the precise frequency-calibration techniques of previous experiments [72]. Improved calibration of mode maps would substantially reduce the leading uncertainty of the g value measurement presented in this thesis. Eventually, the use of a higher-Q trap cavity might also be important in reducing cavity-shift errors.

At some point, g value experiments might become accurate enough that mode Q plays a non-negligible role in calculating cavity shifts. If it is determined that the parametric technique for measuring the cavity mode spectrum cannot be used to measure the mode Q values, techniques might be developed to use the measured cyclotron lifetime for mapping the cavity coupling. This could be a significant improvement, since such a map would not rely on complicated interactions in a cloud of electrons to determine the damping rate of a single electron. A technique which uses the parametric response of a single electron has succeeded in measuring an enhanced decay rate of 23 Hz near a cavity mode [98] and might be useful for making such a lifetime map.

If the anomaly and cyclotron line widths (see Ch. 4) could be narrowed, g value precision would be further improved. First the source of the mysterious line shape rounding must be eliminated. Substantial line-shape narrowing could then be accomplished by reducing the magnetic bottle size. With the axial frequency resolution currently provided by the self-excited oscillator [66], a magnetic bottle a factor of ~ 5 smaller could be used without much difficulty, resulting in narrowing of the cyclotron and anomaly line widths by the same factor. If, in addition to eliminating the line-shape rounding, the axial temperature were cooled to the ~ 30 mK limit of the current dilution refrigerator, additional line-shape narrowing would be achieved. Even lower temperatures might be reached using a more powerful pump for the dilution refrigerator. Cooling of the axial motion, perhaps to the ground state, might also be accomplished by sideband cooling techniques [72, 70].

7.4 Implications for Other Precision Measurements

The techniques developed for the g value measurement presented in this thesis also make possible improvements in other precision experiments. As discussed in Sec. 1.1.4, narrowing of the cyclotron and anomaly resonance widths makes possible improved tests of CPT symmetry and Lorentz invariance, both with and without comparison to a positron. Also, much of the progress made for this g value measurement might benefit a new measurement of the proton-to-electron mass ratio. This mass ratio is used, along with h/m_{Cs} from cesium recoil experiments, in the most competitive measurement of α. With improvements to the cesium recoil experiment [22], uncertainty in the proton-to-electon mass ratio might soon dominate the error of that measurement [20].

Bibliography

[1] S. Peil and G. Gabrielse, Phys. Rev. Lett. **83**, 1287 (1999).

[2] R. S. Van Dyck Jr., P. B. Schwinberg, and H. G. Dehmelt, Phys. Rev. Lett. **59**, 26 (1987).

[3] R. S. Van Dyck Jr., P. B. Schwinberg, and H. G. Dehmelt, in *International Conference on Atomic Physics XII*, edited by W. E. Baylis, G. W. F. Drake, and J. W. McConkey (World Scientific, New Jersey, 1990).

[4] T. Kinoshita, IEEE Trans. on Instrumentation and Measurement **50**, 568 (2001).

[5] T. Kinoshita and M. Nio, Phys. Rev. Lett. **90**, 021803 (2003).

[6] S. Laporta and E. Remiddi, Phys. Lett. B **379**, 283 (1996).

[7] M. E. Peskin and D. V. Schroeder, *Quantum Field Theory* (Addison Wesley, New York, 1995).

[8] R. S. Van Dyck Jr., P. B. Schwinberg, and H. G. Dehmelt, in *The Electron*, edited by D. Hestenes and A. Weingartshofer (Kluwer Academic Publishers, Dordrecht, 1991), p. 239.

[9] J. Schwinger, Phys. Rev. **73**, 416 (1948).

[10] C. M. Sommerfield, Phys. Rev. **107**, 328 (1957).

[11] A. Petermann, Helf. Phys. Acta **30**, 407 (1957).

[12] T. Kinoshita (private communication).

[13] P. J. Mohr and B. N. Taylor, Rev. Mod. Phys. **72**, 351 (2000).

[14] W. V. Hughes and T. Kinoshita, Rev. Mod. Phys. **71**, S133 (1999).

[15] P. J. Mohr and B. N. Taylor, Physics Today **54**, 29 (2001).

[16] B. N. Taylor and P. J. Mohr, IEEE Trans. on Instrumentation and Measurement **50**, 563 (2001).

[17] T. Kinoshita, Rep. Prog. Phys. **59**, 1459 (1996).

[18] A. M. Jeffery, R. E. Elmquist, L. H. Lee, J. Q. Shields, and R. F. Dziuba, IEEE Trans. on Instrumentation and Measurement **46**, 264 (1997).

[19] E. Sarajlic (private communication). There is a typo in Ref. [20]; the result should read $\alpha^{-1} = 137.036\,000\,3\,(10)$.

[20] A. Wicht, J. M. Hensley, E. Sarajlic, and S. Chu, Physica Scripta **102**, 82 (2002).

[21] M. P. Bradley, J. V. Porto, S. Rainville, J. V. Thompson, and D. E. Pritchard, Phys. Rev. Lett. **83**, 4510 (1999).

[22] H. Mueller (private communication).

[23] E. Krüger, W. Nistler, and W. Weirauch, Metrologia **36**, 147 (1999).

[24] D. L. Farnham, Jr. R. S. Van Dyck, and P. B. Schwinberg, Phys. Rev. Lett. **75**, 3598 (1995).

[25] G. Audi and A. H. Wapstra, Nucl. Phys. A **595**, 409 (1995).

[26] W. Liu *et al.*, Phys. Rev. Lett. **82**, 711 (1999).

[27] K. P. Jungman, Hyperfine Interactions **127**, 189 (2000).

[28] V. Y. Shifrin, P. G. Park, V. N. Khorev, C. H. Choi, and C. S. Kim, IEEE Trans. Instrum. Meas. **47**, 638 (1998).

[29] Tarbeev, V. Yu, V. Y. Shifrin, V. N. Khorev, and N. V. Studentsov, Meas. Tech. **32**, 279 (1989).

[30] E. R. Williams, Jr. G. R. Jones, S. Ye, R. Liu, H. Sasaki, P.T. Olsen, W.D. Phillips, and H. P. Layer, IEEE Trans. Instrum. Meas. **38**, 233 (1989).

[31] G. W. F. Drake, Can. J. Phys. **80**, 1195 (2002).

[32] K. Pachucki and J. Sapirstein, J. Phys. B **36**, 803 (2003).

[33] T. Zelevinsky, D. Farkas, and G. Gabrielse, to be published.

[34] M. C. George, L. D. Lombardi, and E. A. Hessels, Phys. Rev. Lett. **87**, 173002 (2001).

[35] R. Bluhm, V. A. Kostelecký, and N. Russel, Phys. Rev. Lett. **79**, 1432 (1997).

[36] V. A. Kostelecký and R. Potting, Phys. Rev. D **51**, 3923 (1995).

[37] D. Colladay and A. Kostelecký, Phys. Rev. D **55**, 6760 (1997).

[38] D. Colladay and A. Kostelecký, Phys. Rev. D **58**, 116002 (1998).

[39] H. Dehmelt, R. Mittleman, R. S. Van Dyck Jr., and P. Schwinberg, Phys. Rev. Lett. **83**, 4694 (1999).

[40] R. K. Mittleman, I. I. Ionnaou, H. G. Dehmelt, and N. Russel, Phys. Rev. Lett. **83**, 2116 (1999).

[41] R. Bluhm, V. A. Kostelecký, and N. Russel, Phys. Rev. D **57**, 3932 (1998).

[42] L. K. Gibbons *et* al., Phys. Rev. D **55**, 6625 (1997).

[43] P. A. M. Dirac, Nature (London) **139**, 323 (1937).

[44] T. Damour, F. Piazza, and G. Veneziano, Phys. Rev. Lett. **89**, 081601 (2002).

[45] M. T. Murphy, J. K. Webb, and V. V. Flambaum, Mon. Not. Roy. Astron. Soc. **342**, 830 (2003).

[46] J. K. Webb, M. T. Murphy, V. V. Flambaum, V. A. Dzuba, J. D. Barrow, C. W. Churchill, J. X. Prochaska, and A. M. Wolfe, Phys. Rev. Lett. **87**, 091301 (2001).

[47] M. Fischer *et al.* , Phys. Rev. Lett. **92**, (2001).

[48] G. W. Bennett *et al.*, Phys. Rev. Lett. **92**, 161802 (2003).

[49] L. Roberts (private communication).

[50] P. B. Scwinberg, R. S. Van Dyck, and H. G. Dehmelt, Phys. Rev. Lett. **47**, 1679 (1981).

[51] R. K. Mittleman, I. I. Ionnaou, and H. G. Dehmelt, in *ICAP XVI Abstracts*, edited by W. E. Baylis and G. W. F. Drake (World Scientific, New Jersey, 1998).

[52] F. L. Palmer, Hyperfine Interactions **81**, 115 (1993).

[53] S. Peil, Ph.D. thesis, Harvard University, 1999.

[54] R. S. Van Dyck Jr., in *Quantum Electrodynamics*, edited by T. Kinoshita (World Scientific, Singapore, 1990), pp. 323–389.

[55] B. D'Urso, B. Odom, and G. Gabrielse, Phys. Rev. Lett. **90**, 043001 (2003).

[56] L. S. Brown, G. Gabrielse, J. Tan, and K. C. D. Chan, Phys. Rev. A **37**, 4163 (1988).

[57] G. Gabrielse and H. Dehmelt, Phys. Rev. Lett. **55**, 67 (1985).

[58] R. S. Van Dyck Jr., P. B. Schwinberg, and H. G. Dehmelt, in *Atomic Physics 9*, edited by R. Van Dyck Jr. and N. Fortson (World Scientific, Singapore, 1984), pp. 52–73.

[59] H. G. Dehmelt, in *Atomic Physics 7*, edited by D. Kleppner and F. M. Pipkin (Plenum Publishing, New York, 1981), pp. 337–372.

[60] W. H. Louisell, R. W. Pidd, and H. R. Crane, Phys. Rev. **94**, 1954 (1954).

[61] D. T. Wilkinson and H. R. Crane, Phys. Rev. **130**, 852 (1963).

[62] F. J. M. Farley, Europhysics News **32**, (2001).

[63] A. Rich and J. Wesley, Rev. Mod. Phys. **44**, 250 (1972).

[64] D. J. Wineland, P. Ekstrom, and H. G. Dehmelt, Phys. Rev. Lett. **31**, 1279 (1973).

[65] R. S. Van Dyck Jr., P. B. Schwinberg, and H. G. Dehmelt, Phys. Rev. Lett. **38**, 310 (1977).

[66] B. D'Urso, R. Van Handel, B. Odom, D. Hanneke, and G. Gabrielse, to be published.

[67] G. Gabrielse and F. C. Mackintosh, International Journal of Mass Spectrometry and Ion Processes **57**, 1 (1984).

[68] G. Gabrielse, J. Tan, and L. S. Brown, in *Quantum Electrodynamics*, edited by T. Kinoshita (World Scientific, Singapore, 1990), pp. 389–415.

[69] L. Brown and G. Gabrielse, Rev. Mod. Phys. **58**, 233 (1986).

[70] B. D'Urso, Ph.D. thesis, Harvard University, 2003.

[71] B. D'Urso and G. Gabrielse, to be published.

[72] J. Tan, Ph.D. thesis, Harvard University, 1992.

[73] J. Tan and G. Gabrielse, App. Phys. Lett. **55**, 2144 (1989).

[74] L. Lapidus, Ph.D. thesis, Harvard University, 1998.

[75] H. Dehmelt, Proc. Natl. Acad. Sci. USA **83**, 2291 (1986).

[76] H. Dehmelt, Proc. Natl. Acad. Sci. USA **83**, 3074 (1986).

[77] D. Phillips, Ph.D. thesis, Harvard University, 1996.

[78] D. Hanneke, Ph.D. thesis, Harvard University, Unfinished.

[79] R. van Handel, Ph.D. thesis, Harvard University, .

[80] R. S. Van Dyck Jr., D. L. Farnham, S. L. Zafonte, and P. B. Schwinberg, **70**, 1665 (1999).

[81] R. K. Pathria, *Statistical Mechanics* (Butterworth Heinemann, Boston, 1997).

[82] *Handbook of Chemistry and Physics, 63rd Edition*, edited by R. C. Weast and M. J. Astle (CRC Press, Inc., Boca Raton, Florida, 1982).

[83] L. S. Brown, Ann. Phys. **159**, 62 (1985).

[84] L. S. Brown and G. Gabrielse, Phys. Rev. A **32**, 3204 (1985).

[85] S. Peil, B. Odom, and G. Gabrielse, Bull. Am. Phys. Soc. **43**, 1272 (1998).

[86] F. L. Palmer, Phys. Rev. A **47**, 2610 (1993).

[87] L. S. Brown, G. Gabrielse, K. Helmerson, and J. Tan, Phys. Rev. Lett. **55**, 44 (1985).

[88] G. Gabrielse and J. Tan, in *Advances in Atomic, Molecular and Optical Physics: Supplement 2: Cavity Quantum Electrodynamics*, edited by P. Berman (Academic Press, New York, 1994), pp. 267–299.

[89] D.G. Boulware and L.S. Brown, Phys. Rev. Lett. **55**, 133 (1985).

[90] D.G. Boulware, L.S. Brown, and T. Lee, Phys. Rev. D **32**, 729 (1985).

[91] J. D. Jackson, *Classical Electrodynamics* (John Wiley & Sons, Inc., New York, 1962).

[92] R. S. Van Dyck Jr., F. L. Moore, D. L. Farnham, P. B. Schwinberg, and H. G. Dehmelt, Phys. Rev. A **36**, 3455 (1987).

[93] J. Tan and G. Gabrielse, Phys. Rev. A **48**, 3105 (1993).

[94] L. Brown and G. Gabrielse, Phys. Rev. A **25**, 2423 (1982).

[95] R. K. Mittleman, F. L. Palmer, and H. G. Dehmelt, Hyperfine Interactions **81**, 105 (1993).

[96] R. S. Van Dyck Jr., P. B. Schwinberg, and H. G. Dehmelt, in *New Frontiers in High Energy Physics*, edited by B. Kursunoglu, A. Perlmutter, and L. Scott (Plenum, New York, 1978), pp. 159–181.

[97] R. S. Van Dyck Jr. and G. Gabrielse, unpublished.

[98] Ching-Hua Tseng, Ph.D. thesis, Harvard University, 1995.